RATE TRANSIENT ANALYSIS IN SHALE GAS RESERVOIRS WITH TRANSIENT LINEAR BEHAVIOR

A Dissertation

by

RASHEED OLUSEHUN BELLO

Submitted to the Office of Graduate Studies of
Texas A&M University
in partial fulfillment of the requirements for the degree of

DOCTOR OF PHILOSOPHY

May 2009

Major Subject: Petroleum Engineering

RATE TRANSIENT ANALYSIS IN SHALE GAS RESERVOIRS WITH TRANSIENT LINEAR BEHAVIOR

A Dissertation

by

RASHEED OLUSEHUN BELLO

Submitted to the Office of Graduate Studies of
Texas A&M University
in partial fulfillment of the requirements for the degree of

DOCTOR OF PHILOSOPHY

Approved by:

Chair of Committee,	Robert A. Wattenbarger
Committee Members,	Goong Chen
	Christine Ehlig-Economides
	Bryan Maggard
Head of Department,	Stephen Holditch

May 2009

Major Subject: Petroleum Engineering

ABSTRACT

Rate Transient Analysis in Shale Gas Reservoirs with Transient Linear Behavior.

(May 2009)

Rasheed Olusehun Bello, B.Sc., University of Lagos, Nigeria;

M.Sc., University of Saskatchewan, Canada

Chair of Advisory Committee: Dr. Robert Wattenbarger

Many hydraulically fractured shale gas horizontal wells in the Barnett shale have been observed to exhibit transient linear behavior. This transient linear behavior is characterized by a one-half slope on a log-log plot of rate against time. This transient linear flow regime is believed to be caused by transient drainage of low permeability matrix blocks into adjoining fractures. This transient flow regime is the only flow regime available for analysis in many wells.

The hydraulically fractured shale gas reservoir system was described in this work by a linear dual porosity model. This consisted of a bounded rectangular reservoir with slab matrix blocks draining into adjoining fractures and subsequently to a horizontal well in the centre. The horizontal well fully penetrates the rectangular reservoir. Convergence skin is incorporated into the linear model to account for the presence of the horizontal wellbore.

Five flow regions were identified with this model. Region 1 is due to transient flow only in the fractures. Region 2 is bilinear flow and occurs when the matrix drainage begins simultaneously with the transient flow in the fractures. Region 3 is the response

for a homogeneous reservoir. Region 4 is dominated by transient matrix drainage and is the transient flow regime of interest. Region 5 is the boundary dominated transient response. New working equations were developed and presented for analysis of Regions 1 to 4. No equation was presented for Region 5 as it requires a combination of material balance and productivity index equations beyond the scope of this work.

It is concluded that the transient linear region observed in field data occurs in Region 4 – drainage of the matrix. A procedure is presented for analysis. The only parameter that can be determined with available data is the matrix drainage area, A_{cm}.

It was also demonstrated in this work that the effect of skin under constant rate and constant bottomhole pressure conditions is not similar for a linear reservoir. The constant rate case is the usual parallel lines with an offset but the constant bottomhole pressure shows a gradual diminishing effect of skin. A new analytical equation was presented to describe the constant bottomhole pressure effect of skin in a linear reservoir.

It was also demonstrated that different shape factor formulations (Warren and Root, Zimmerman and Kazemi) result in similar Region 4 transient linear response provided that the appropriate *f(s)* modifications consistent with λ_{Ac} calculations are conducted. It was also demonstrated that different matrix geometry exhibit the same Region 4 transient linear response when the area-volume ratios are similar.

DEDICATION

I dedicate my work to all those who have lovingly supported me throughout life and all its travails.

ACKNOWLEDGEMENTS

First, I want to give praises to Almighty Allah for sparing my life, continuously granting me His blessings and allowing me to successfully conclude this phase of my life.

I want to acknowledge my supervisor, Dr. Robert. A. Wattenbarger for being a father, mentor, supervisor and friend to me. I am honored to have worked with him. I am also eternally grateful to him. I want to acknowledge the suggestions and contributions of my committee members, Dr. Christine Ehlig-Economides , Dr. Bryan Maggard – whose classes are among my favorites and invaluable- and Dr. Goong Chen.

I want to acknowledge the eternal support of my parents, Rahaman and Doja Bello, my siblings- Biodun, Bidemi and Tolu- and my girl, Medinat.

TABLE OF CONTENTS

CHAPTER Page

LIST OF TABLES

TABLE Page

LIST OF FIGURES

FIGURE Page

FIGURE Page

FIGURE Page

FIGURE Page

CHAPTER I

INTRODUCTION

Natural gas demand in the United States is expected to increase from 23 tcf/yr currently to 30-34 tcf/yr by the year 2025.[1] United States natural gas production is also expected to increase from 19.5 tcf/yr in 2004 to more than 25 tcf/yr by the year 2020 in order to satisfy this demand as shown in Fig. 1.1. Conventional gas sources (sandstone reservoirs) will not be able to satisfy this demand and unconventional gas sources (tight gas, shale gas and coalbed methane) are thus expected to be a major component of this production (Fig. 1.1).

Unconventional reservoirs are defined as reservoirs that cannot be produced at economic flowrates or that do not produce economic volumes of oil and gas without assistance from massive stimulation treatments or special recovery processes, such as steam injection.[2] Unconventional reservoirs are normally described as basin-centered continuous accumulations. The hydrocarbons are distributed throughout a large area. These accumulations do not have well-defined hydrocarbon-water contacts and are usually abnormally pressured.[3]

Shales are fissile rocks composed of layers of fine-grained sediments. Shale reservoirs are normally regarded as the source rocks for the petroleum system according

---

This dissertation follows the style of *Society of Petroleum Engineers Journal*.

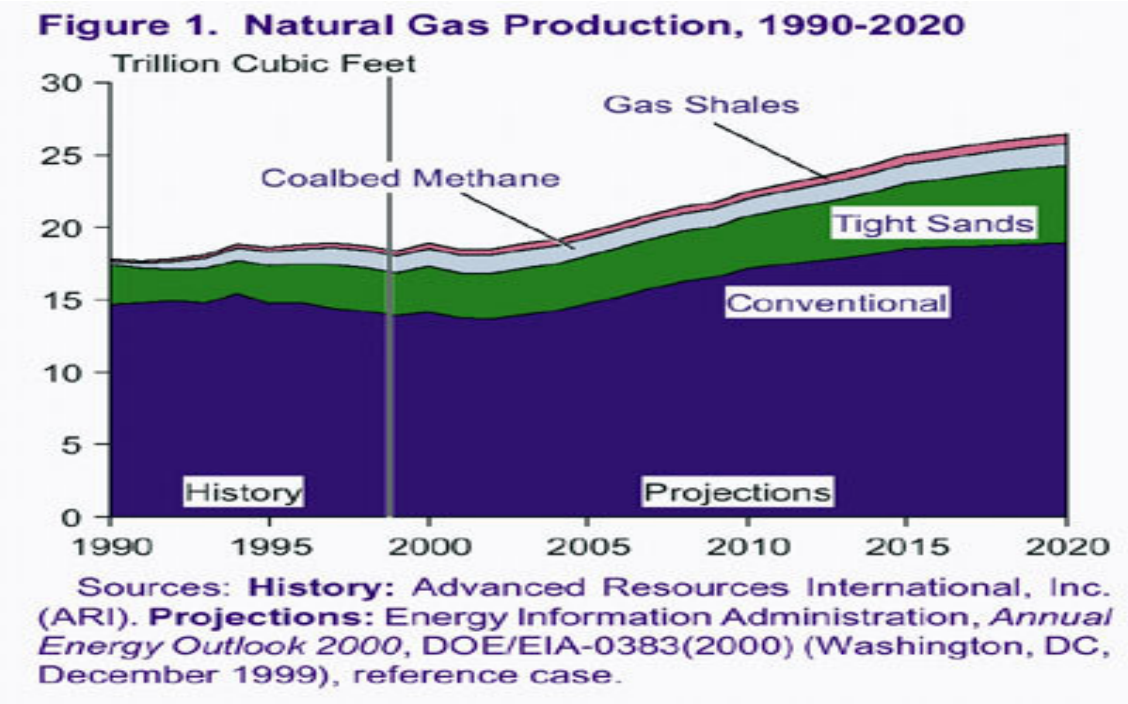

Fig. 1.1 – United States Natural Gas Production, 1990-2020.[4]

to the organic theory. The hydrocarbon is generated in the source rock (shale) and migrates to a reservoir rock (e.g. sandstone). However, the unconventional shale gas reservoir which is the focus of this study are self-sourcing reservoirs. The shale acts as both a source rock and reservoir.

A map of the major shale basins in the United States is shown in Fig. 1.2. The Gas Technology Institute estimates that organic shale reservoirs in the United States contain up to 780 tcf of gas. The Barnett Shale in the Fort Worth Basin is by far the most active shale gas play in the United States. The reservoir ranges from 100 ft to more than 1000 ft in gross thickness and holds from 50 to 200 bcf of gas per square mile.[5]

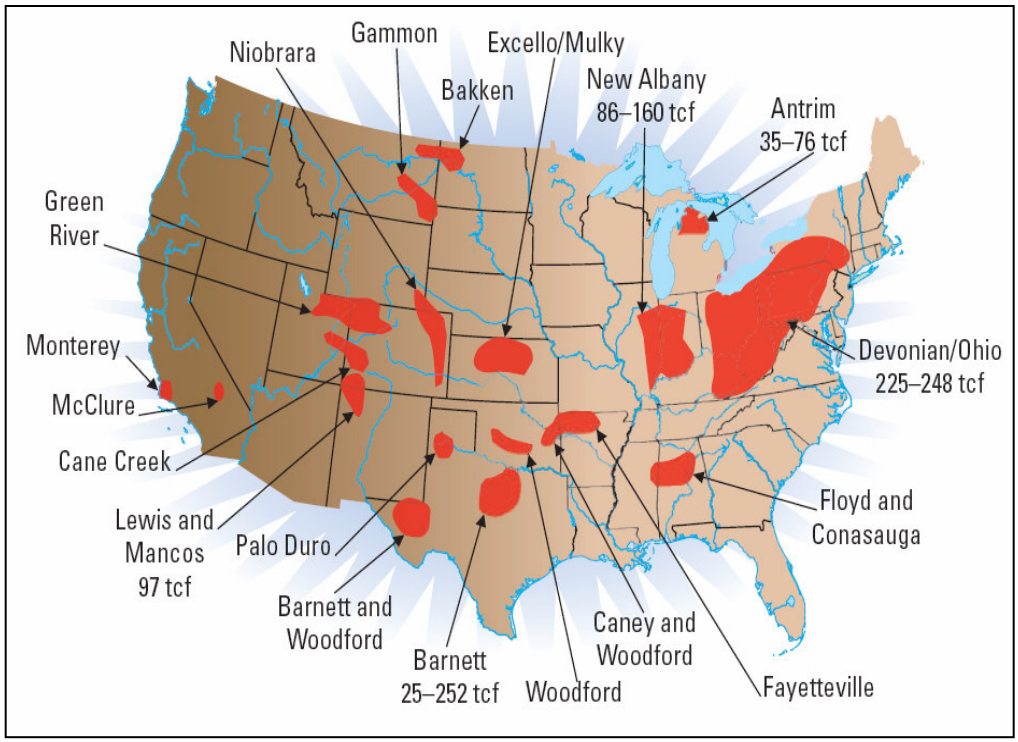

Fig. 1.2 - Map of the Major United States Shale Basins.[5]

Shales can be classified[2] based on hydrocarbon (gas) generation mechanism as thermogenic (organic matter is transformed into hydrocarbons under the influence of temperature) or biogenic (water which contains microorganisms migrates into the rock and transforms the organic matter).

Shales can be also be classified as:[2] (i) Shales having very fine sand and silt laminae and beds; gas is thermogenic (similar to tight sand e.g. Ohio Shale, Lewis shale); (ii) Dark organic-rich shales having water-filled fractures and must be depressurized (like coalbed reservoirs; gas reservoirs may be biogenic or thermogenic e.g. Antrim shale); and (iii) Mixed – Shales that have characteristics of the above, depending on location in basin e.g. New Albany Shale.

In general, shale gas reservoirs are characterized[6] by low production rates (20 to 500 Mscf per day), long production lives (up to 30 yrs), low decline rates (typically 2 to 3% per yr), ability to be thick (up to 1,500 ft) and large gas reserves (5 bcf to 50 bcf per section). Shale gas reservoirs are also typically organically rich.

In shales, natural fractures provide permeability and the matrix provides storage of most of the gas. They are thus also referred to as a Nelson Type II Fractured Reservoir.[2] Shale matrix permeabilities can be as low as 10^{-9} md.[7] Matrix porosities range from 1 to 6%.[8] The gas is stored either by compression (as free gas) or by adsorption on the surfaces of the solid material (either organic matter or minerals).

The adsorption (desorption) behavior of shale gas reservoirs have typically been modeled by the Langmuir isotherm.[9] It has been shown[8,10] that in the Barnett shale, at higher pressures (above 1000 psia), gas storage occurs as free gas in the matrix porosity. Below 1000 psia, desorption is important and adsorbed gas may account for 50 to 60% of total gas stored.

Shale gas reservoirs were traditionally ignored because of the low matrix permeability and the costs thus associated with production. The Section 29 tax credit (1980-2002) was one of the factors which revived interest in these reservoirs. It allowed a credit of $3 per barrel of oil equivalent for production from unconventional sources. It was amended in 2003 by the Energy Policy Act Section 1345.[11] Other factors were technological improvements and include horizontal wells and hydraulic fracturing. The use of water-based or nitrogen foam fracturing fluids along with proppants in hydraulic

fracturing have aided production from these reservoirs. In recent times, high oil and gas prices have renewed interest in shale gas reservoir exploitation.

1.1 Problem Description

Horizontal wells producing gas in the Barnett shale are typically multi-stage hydraulically fractured. Typical micro-seismic data used to monitor the hydraulic fractures is shown in Fig. 1.3. The different hydraulic fracture stages are indicated by the different clusters.

Shale gas production data from a sample well in the Barnett shale is plotted against time on a log-log plot as shown in Fig. 1.4. A half-slope is obtained on the plot. This indicates a transient linear regime analogous to Regime 4 described by Ozkan *et al.*[12] for dual porosity behavior in a radial reservoir. The transient linear behavior shown in Fig. 1.4 occurs for a duration of almost two log cycles. The transient linear behavior shown in Fig. 1.4 has been observed in several shale gas wells and is the only flow regime available for analysis in numerous cases. The question thus arises of how to conduct proper analysis of this flow regime and what parameters can be determined.

Wattenbarger[13] identified different causes for transient linear flow including hydraulic fracture draining a square geometry, high permeability layers draining adjacent tight layers and early-time constant pressure drainage from different matrix geometry. A possible cause for the transient linear regime identified in Fig. 1.4 is the drainage from the matrix blocks into high permeability surrounding fractures (as demonstrated in Appendix A). These high permeability fractures thus have negligible pressure drop and

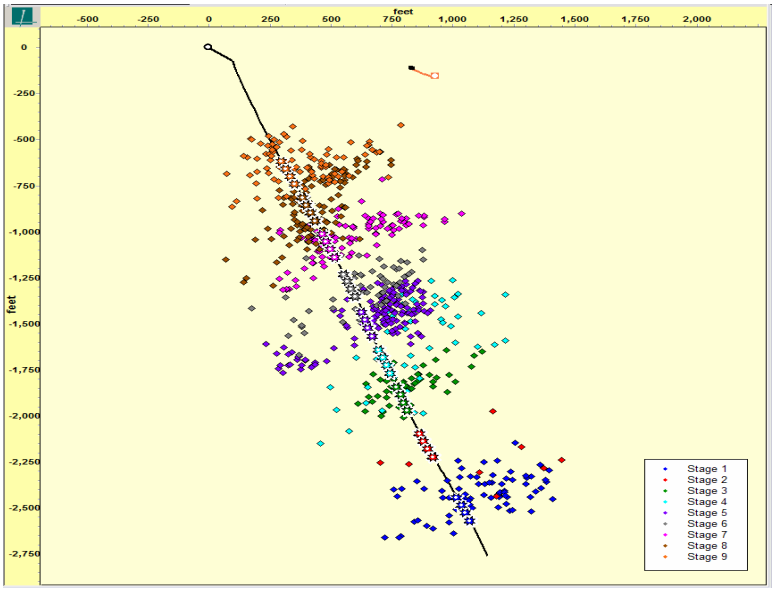

Fig. 1.3 – Microseismic Map of Multi-Stage Hydraulically Fractured Horizontal Well.

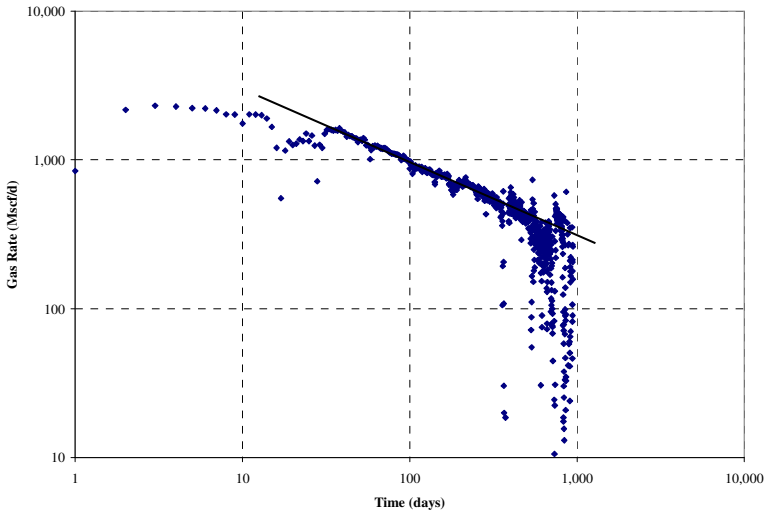

Fig. 1.4 - Log-log Plot of Field Production Rate as a Function of Time. Line drawn on plot indicates half slope.

transient linear flow occurs. This description is consistent with the dual porosity concept for shale gas reservoirs.

Mayerhofer *et al.*[14] present a model for hydraulically fractured shale gas reservoirs. Their model represents the hydraulic fracture as an interconnected network of fractures. Their paper indicates that drainage does not occur far beyond the stimulated region because of the low matrix permeability. This observation was also stated by Carlson and Mercer.[15]

In the current work, the hydraulically fractured horizontal shale gas well will be modeled as a horizontal well draining a rectangular geometry containing a network of fractures separated by matrix blocks (dual-porosity system) as suggested by Fig. 1.3. The solutions presented by El-Banbi[16] for a linear dual porosity model will be extended and applied to this system. The effects of desorption and diffusion will be assumed negligible in this paper since they will not be important at reservoir pressures of interest in the Barnett shale as previously described.

1.2 Objectives

The objectives of this research are

- To develop mathematical models to analyze these multi-stage hydraulically fractured horizontal wells
- To develop a rate transient analysis procedure for analyzing these wells to enable the determination of reservoir characteristics, drainage

volume/original gas-in-place (OGIP), fracture network characteristics and assessment of the effectiveness of different hydraulic fracture treatments.

1.3 Organization of This Dissertation

The study is divided into eight chapters. The outline and organization of this dissertation are as follows:

Chapter I presents an overview of shale gas. The research problem is described and the project objectives are presented.

Chapter II presents an extensive literature review. The dual porosity model and its applications to liquids and gas are reviewed. Horizontal well applications are also reviewed.

Chapter III describes the linear model to be used in this work. Validation of the linear model is also presented.

Chapter IV presents new analysis equations developed using the linear model.

Chapter V discusses the transient linear regime in detail and discusses the effects of shape factors and area-volume ratio.

Chapter VI describes the constant bottomhole pressure effect of skin in linear reservoirs

Chapter VII presents development of new type curves with application to sample field data.

Chapter VIII presents conclusions and recommendations.

CHAPTER II

LITERATURE REVIEW

2.1 Introduction

Initial studies of fractured reservoirs were concerned with applications to well test analysis of reservoir flow of liquids (constant rate, pressure buildup and drawdown). Subsequent research considered production data analysis (constant bottomhole pressure) and extension of existing models to gas flow. Most of the literature is devoted to radial reservoir models. In this chapter, review of literature will be conducted in three sections. The first section discusses the dual porosity model and its application to flow of slightly compressible fluids. The second section discusses the application of the dual porosity model to gas flow. The final section discusses the application of the dual porosity model to analysis of naturally fractured reservoirs with horizontal wells.

2.2 Dual Porosity Model (Slightly Compressible Fluids)

Naturally fractured reservoirs (tight gas, shale gas and coal gas) have been described by the dual porosity model. The dual porosity model was first formulated by Barenblatt *et al.*[17] and later extended to well test analysis by Warren and Root.[18] The Warren and Root model forms the basis of modern day analysis of naturally fractured reservoirs. In the Warren and Root model, the naturally fractured reservoir is modeled by uniform homogeneous matrix blocks separated by fractures as shown in Fig. 2.1. The matrix blocks provide storage of the fluid to be produced while the fractures provide the

permeability. When a producing well is present, the fluid flows from the matrix to the fractures and to the well. There have been two types of approach in applying the dual porosity model based on how flow of the fluid from the matrix to the fractures is modeled – pseudosteady state and transient.

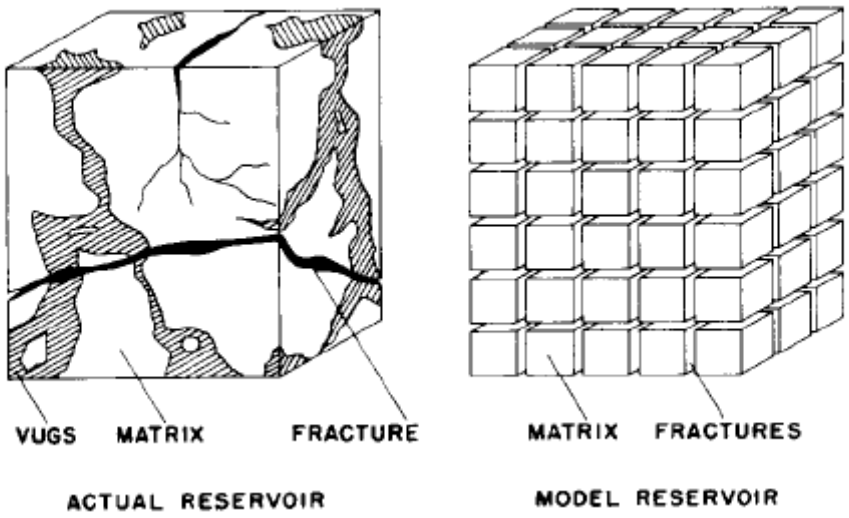

Fig. 2.1 - Dual Porosity Model.[18]

2.2.1 Pseudosteadystate Matrix-Fracture Transfer Models

An equation for interporosity flow from the matrix to the fractures at a mathematical point under pseudosteadystate (quasisteadystate or semisteadystate) conditions was presented by Warren and Root.[18]

$$q = \sigma \frac{k_m}{\mu}\left(p_m - p_f\right)$$

Where q is the drainage rate per unit volume, σ is the Warren and Root shape factor, p_m is the matrix pressure at a mathematical point.

Two new parameters which are used to characterize naturally fractured reservoirs were presented by Warren and Root[18] - the interporosity flow parameter, λ (a measure of the flow capacity of the system) and the storativity, ω (a measure of the storage capacity of the fractures). Warren and Root[18] were the first to apply Laplace transformation to obtain "*f(s)*" and solve for the dimensionless pressure distribution. A method of analyzing pressure buildup data for the infinite radial reservoir case was presented. Buildup plots were found to exhibit parallel lines on a semilog plot separated by an S-shaped transition period. The first line represents flow in the fracture system only while the second line represents flow in the total system (matrix and fractures).

Kazemi *et al.*[19] investigated the suitability of applying the Warren and Root model to interpret interference results. They presented a model which extends the Warren and Root model to interference testing. They applied the Laplace transformation to obtain "*f(s)*" and solve for the dimensionless pressure distribution. They also numerically solved the model equations by finite-difference methods and included vertical pressure gradients. It was concluded that an equivalent homogeneous model was not appropriate at early times but could be used at later times. It was also concluded that the Warren and Root model yielded similar results as their numerical solution and was thus appropriate for analyzing naturally fractured reservoirs.

Odeh[20] developed an infinite radial reservoir model for the behavior of naturally fractured reservoir. The model incorporates some limiting assumptions. The Laplace transformation is also utilized. Two parallel straight lines were not observed on a semilog plot contrary to Warren and Root's results. It was concluded that buildup and drawdown plots of naturally fractured reservoir transient responses are similar to those of homogeneous reservoirs.

Mavor and Cinco-Ley[21] present solutions for the constant rate case in an infinite radial reservoir with and without wellbore storage and skin; and a bounded radial reservoir. Solutions are also presented for the first time for a constant pressure inner boundary with skin in an infinite radial reservoir.

Da Prat *et al.*[22] extended the Warren and Root[18] solutions to constant pressure inner boundary conditions and bounded outer boundary cases for the radial reservoir. They also present type curves for analysis. The results do not appear to represent realistic field cases.

Bui *et al.*[23] present type curves for transient pressure analysis of partially penetrating wells in naturally fractured reservoirs by combining the Warren and Root model with the solution for these wells in homogeneous reservoirs.

2.2.2 Transient Matrix-Fracture Transfer Models

Kazemi[24] used a slab matrix model with horizontal fractures and unsteady state matrix-fracture flow to represent single-phase flow in the fractured reservoir. The assumptions include homogeneous behavior and isotropic matrix and fracture properties. The well is

centrally located in a bounded radial reservoir. A numerical reservoir simulator was used. It was concluded that the results were similar to the Warren and Root model when applied to a drawdown test in which the boundaries have not been detected. Two parallel straight lines were obtained on a semilog plot. The first straight line may be obscured by wellbore storage effects and the second straight line may lead to overestimating ω when boundary effects have been detected.

De Swaan[25] presented a model which approximates the matrix blocks by regular solids (slab and spheres) and utilizes heat flow theory to describe the pressure distribution. It was assumed that the pressure in the fractures around the matrix blocks is variable and the source term is described through a convolution term. Approximate line-source solutions for early and late time are presented. The late time solutions are similar to those for early time except that modified hydraulic diffusivity terms dependent on fracture and matrix properties are included. The results are two parallel lines representing the early and late time approximations. The late time solution matches Kazemi[24] for the slab case. De Swaan's model does not properly represent the transition period.

Najurieta[26] presented a transient model for analyzing pressure transient data based on De Swaan's[25] theory. Two types of fractured reservoir were studied- stratum (slabs) and blocks (approximated by spheres). The model predicted results similar to Kazemi.[24]

Serra *et al.*[27] present methods for analyzing pressure transient data. The slab model used is similar to De Swaan[25] and Najurieta.[26] The model considers unsteady state

matrix fracture transfer and is for an infinite reservoir. Three flow regimes were identified. Flow Regime 1 and 3 are the Warren and Root[18] early and late time semilog lines. A new flow Regime 2 was also identified with half the slope of the late time semilog line.

Chen *et al.*[28] present methods for analyzing drawdown and buildup data for a constant rate producing well centrally located in a closed radial reservoir. The slab model similar to De Swaan[25] and Kazemi[24] is used. Five flow regimes are presented. Flow regimes 1, 2 and 3 are associated with an infinite reservoir and are described in Serra *et al.*[27] Flow regime 1 occurs when there is a transient only in the fracture system. Flow regime 2 occurs when the transient occurs in the matrix and fractures. Flow regime 3 is a combination of transient flow in the fractures and "pseudosteady state" in the matrix. Pseudosteadystate in the matrix occurs when the no-flow boundary represented by the symmetry center line in the matrix affects the response. Two new flow regimes associated with a bounded reservoir are also presented. Flow regime 4 reflects unsteady linear flow in the matrix system and pseudosteadystate in the fractures.. Flow Regime 5 occurs when the response is affected by all the boundaries (pseudosteady-state).

Streltsova[29] applied a "gradient model" (transient matrix-fracture transfer flow) with slab-shaped matrix blocks to an infinite reservoir. The model predicted results which differ from the Warren and Root model in early time but converge to similar values in late time. The model also predicted a linear transitional response on a semi-log plot between the early and late time pressure responses which has a slope equal to half

that of the early and late time lines. This linear transitional response was also shown to differ from the S-shaped inflection predicted by the Warren and Root model.

Cinco Ley and Samaniego[30] utilize models similar to De Swaan[25] and Najurieta[26] and present solutions for slab and sphere matrix cases. They utilize new dimensionless variables – dimensionless matrix hydraulic diffusivity, and dimensionless fracture area. They describe three flow regimes observed on a semilog plot – fracture storage dominated flow, "matrix transient linear" dominated flow and a matrix pseudosteadystate flow. The "matrix transient linear" dominated flow period is observed as a line with one-half the slopes of the other two lines.[27,29] It should be noted that the "matrix transient linear" period yields a straight line on a semilog plot indicating radial flow and might be a misnomer. The fracture storage dominated flow is due to fluid expansion in the fractures. The "matrix transient linear" period is due to fluid expansion in the matrix. The matrix pseudosteadystate period occurs when the matrix is under pseudosteadystate flow and the reservoir pressure is dominated by the total storativity of the system (matrix + fractures). It was concluded that matrix geometry might be identified with their methods provided the pressure data is smooth.

Lai *et al.*[31] utilize a one-sixth of a cube matrix geometry transient model to develop well test equations for finite and infinite cases including wellbore storage and skin. Their model was verified with a numerical simulator employing the Multiple Interacting Continua (MINC) method.

Ozkan *et al.*[12] present analysis of flow regimes associated with flow of a well at constant pressure in a closed radial reservoir. The rectangular slab model similar to De

Swaan[25] and Kazemi[24] is used. Five flow regimes are presented. Flow regimes 1, 2 and 3 are described in Serra *et al*.[27] Two new regimes are presented- Flow regime 4 reflects unsteady linear flow in the matrix system and occurs when the outer boundary influences the well response and the matrix boundary has no influence. Flow Regime 5 occurs when the response is affected by all the boundaries.

Houze *et al*.[32] present type curves for analysis of pressure transient response in an infinite naturally fractured reservoir with an infinite conductivity vertical fracture.

Stewart and Ascharsobbi[33] present an equation for interporosity skin which can be introduced into the pseudosteadystate and transient models. The effect of interporosity skin is to delay flow from the matrix to the fractures. This equation is given by

$$s_{ma} = \frac{2k_{mi}h_s}{h_m k_s}$$

where k_{mi} is the intrinsic matrix permeability, h_s is the thickness of the interporosity skin layer, h_m is the matrix block dimension and k_s is the permeability of the interporosity skin layer.

It should be noted that all the transient models previously described were developed for the radial reservoir cases (infinite or bounded).

El-Banbi[16] was the first to present transient dual porosity solutions for the linear reservoir case. New solutions were presented for a naturally fractured reservoir using a dual porosity, linear reservoir model. Solutions are presented for a combination of different inner boundary (constant pressure, constant rate, with or without skin and

wellbore storage) and outer boundary conditions (infinite, closed, constant pressure). This model will be used in this work.

2.3 Dual Porosity Model (Gas)

Kucuk and Sawyer[34,35]presented a model for transient matrix-fracture transfer for the gas case. Previous work had been concerned mainly with modeling slightly compressible (liquid) flow. They considered cylindrical and spherical matrix blocks cases. They also incorporate the pseudopressure definitions for gases. Techniques for analyzing buildup data are also presented for shale gas reservoirs. Their model results plotted on a dimensionless basis matched Warren and Root[18] and Kazemi[24] for very large matrix blocks at early time but differ at later times. They also conclude from their tests that naturally fractured reservoirs do not always exhibit the Warren and Root behavior (two parallel lines).

Carlson and Mercer[15] coupled Fick's law for diffusion within the matrix and desorption in their transient radial reservoir model for shale gas. Modifications include use of the pressure-squared forms valid for gas at low pressures to linearize the diffusivity equation. They provide a Laplace space equation for the gas cumulative production from their model and use it to history match a sample well. They also show that semi-infinite behavior (portions of the matrix remain at initial pressure and is unaffected by production from the fractures) occurs in shale gas reservoirs regardless of matrix geometry. They present an equation for predicting the end of this semi-infinite behavior.

Gatens *et al.*[36] analyzed production data from about 898 Devonian shale wells in four areas. They present three methods of analyzing production data – type curves, analytical model and empirical equations. The empirical equation correlates cumulative production data at a certain time with cumulative production at other times. This avoids the need to determine reservoir properties. Reasonable matches with actual data were presented. The analytical model is used along with an automatic history matching algorithm and a model selection procedure to determine statistically the best fit with actual data.

Watson *et al.*[37] present a procedure that involves selection of the most appropriate production model from a list of models including the dual porosity model using statistics. The analytical slab matrix model presented by Serra *et al.*[27] is utilized. Reservoir parameters are estimated through a history matching procedure that involves minimizing an objective function comparing measured and estimated cumulative production. They incorporate the use of a normalized time in the analytical model to account for changing gas properties with pressure. Reasonable history matches were obtained with sample field cases but forecast was slightly underestimated.

Spivey and Semmelbeck[38] present an iterative method for predicting production from dewatered coal and fractured gas shale reservoirs. The model used is a well producing at constant bottomhole pressure centered in a closed radial reservoir. A slab matrix is incorporated into these solutions. These solutions are extended to the gas case by using an adjusted time and adjusted pressure. Their method also uses a total compressibility term accounting for desorption.

2.4 Horizontal Wells in Naturally Fractured Reservoirs

There have been different traditional approaches to modeling horizontal wells in homogeneous reservoirs. Horizontal wells are normally modeled as infinite conductivity (pressure is uniform along the wellbore). It is not practical, as Gringarten *et al*.[39] demonstrated with infinite conductivity fractures, to compute the wellbore pressure from the infinite-conductivity model because of the computational work involved. Gringarten *et al*.[39] suggested computing the pressure drop from the uniform flux model (flowrate is the same for each individual segment along a wellbore) at a value of $x_D = 0.732$. This value was the point at which the uniform flux model yields the same results as the infinite conductivity model. This computation has also been incorporated into horizontal well models.[40-46]

The mathematical problem to be solved for the anisotropic case is usually given by

$$k_x \frac{\partial^2 p}{\partial x^2} + k_y \frac{\partial^2 p}{\partial y^2} + k_z \frac{\partial^2 p}{\partial z^2} = \phi \mu c_t \frac{\partial p}{\partial t}$$

Several authors have used a model of a line source well in a semi-infinite[45,47] or infinite reservoir.[40-44,48-50] Others[41-44,48,51] have used a line source well in a closed rectangular reservoir. The infinite model has no-flow boundaries at the top and bottom. The semi-infinite reservoir model has three no-flow boundaries (top, bottom and left). The closed reservoir model has all four no-flow boundaries.

It should be noted that in these models, the well is usually not completely penetrating but the models by Ozkan [41-44] and Odeh and Babu[51] provide this possibility once the appropriate well and reservoir dimensions are specified.

The differential equation and boundary conditions have been mostly solved by the Newman product method and source functions.[40-45] These concepts for the homogeneous reservoir case have been extended to model horizontal wells in naturally fractured reservoirs.

Ozkan[41-44] presents Laplace space solutions for horizontal wells in a reservoir for infinite and closed rectangular boundary cases in terms of *f(s)*. The line source approach previously described is utilized. As demonstrated by Ozkan, there is a possibility of applying this to the naturally fractured reservoir by substituting the appropriate *f(s)* for a selected matrix geometry.

Carvalho and Rosa[52] present solutions for an infinite conductivity horizontal well in a semi-infinite reservoir. The reservoir is homogeneous and isotropic. The horizontal well is modeled as a line source. The solutions for the homogeneous case were then extended to the dual porosity case by substituting *s*f(s)* for *s* in Laplace space for the pressure derivative (homogeneous). Wellbore storage and skin are incorporated into their model using Laplace space.

Aguilera and Ng[53] present analytical equations for pressure transient analysis. Their model is a horizontal well in a semi-infinite, anisotropic, naturally fractured reservoir. Transient and pseudosteadystate interporosity flow is considered. Six flow periods are identified –First radial flow (at early times, from fractures), Transition

period, Second radial flow in vertical plane, First linear flow, Pseudoradial flow and Late linear - with expressions for determining skin provided.

Ng and Aguilera[54] present analytical solutions using a line source and then compute pressure drop on a point away from the well axis to account for the radius of the actual well. A method for determining the numerical Laplace transform is presented. This method was then used to compute the dual porosity response (pseudosteady state). Their solutions were compared to other solutions.

Thompson *et al*.[55] present an algorithm for computing horizontal well response in a bounded dual porosity reservoir. Their model is a horizontal well in a closed rectangular reservoir. Their procedure involves converting a known analytic solution to Laplace space numerically point by point and then inverting using the Stehfest algorithm.[56] This is similar to the procedure presented by Ohaeri and Vo[46] who use a numerical Laplace space algorithm[57] but also present alternative equations determined by parameter ranges which result in computational efficiency.

Du and Stewart[58] describe situations which can yield linear flow behavior – a multi-layered reservoir (one layer has a very high permeability relative to the other); naturally fractured reservoir (flow from matrix into horizontal well intersecting fractures); and areal anisotropy (vertical fractures aligned predominantly in one direction). Their model is that of a horizontal well in a homogeneous, infinite acting reservoir. Three flow regimes are identified – radial vertical flow, linear flow opposite completed section and pseudoradial flow at late time. A bilinear flow behavior was also identified.

The model presented in this work has the advantage of being simpler than the horizontal well models. The model will be presented in Chapter III. It also allows the direct use of Laplace space techniques not easily seen with these horizontal well models. Review of literature also shows that the transient linear flow regime has not been investigated in the manner presented in this work.

CHAPTER III

MATHEMATICAL MODEL

3.1 Introduction

A schematic of the model to be used in this work is shown in Fig. 3.1. A rectangular grid is imposed on the microseismic results as shown in Fig. 3.1. The model is shown in detail with representative cube matrix blocks in Fig. 3.2. The features of the model to be used in this work are described below.

- A closed rectangular geometry reservoir containing a network of natural and hydraulic fractures (as in Mayerhofer *et al.*[14]). The fractures do not drain beyond the boundaries of this rectangular geometry.
- The perforated length of the well , x_e is the same as the width of the reservoir.
- Flow is towards the well at the centre of the rectangular geometry
- It is a dual porosity system consisting of matrix blocks and fractures
- The transient dual porosity solutions presented for a linear model by El-Banbi[16] are applied and extended to this system. Modifications will be made to this linear model to include the convergence skin accounting for flow towards an actual horizontal well.

The slab matrix model is more commonly used in the literature. This model will be similarly adopted and is shown in Fig. 3.3. The mathematical details of this linear dual porosity model (slab matrix) are given in Appendix B.

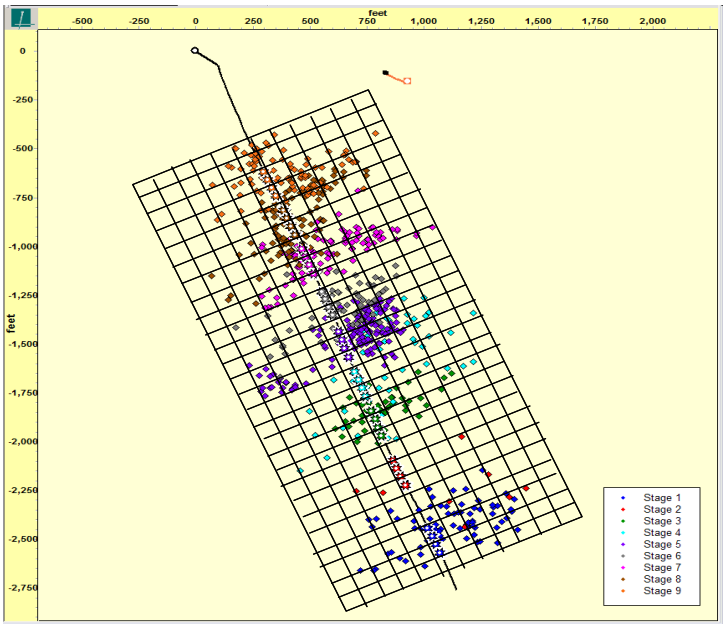

Fig. 3.1 – Hydraulically Fractured Horizontal Well in Shale Gas Reservoir. Rectangular grid superimposed on system to represent our model.

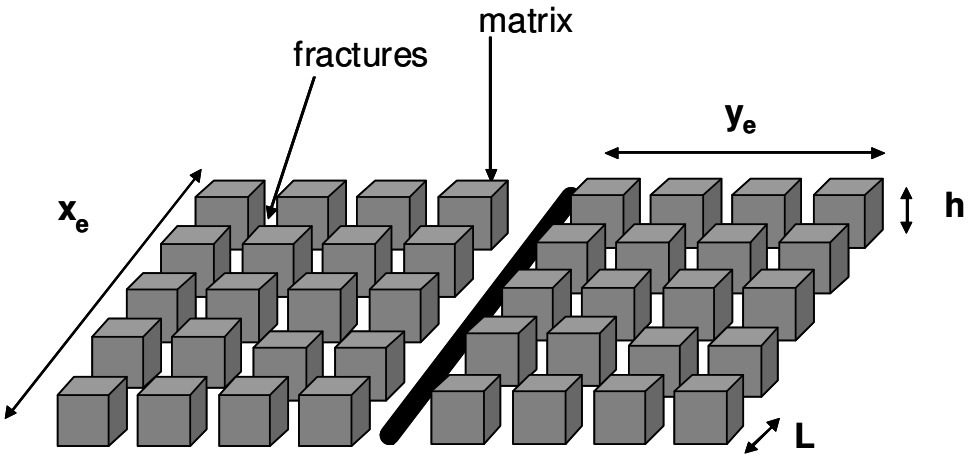

Fig. 3.2 – Schematic of Cube Matrix Linear Model of Hydraulically Fractured Well. Cross-sectional area at well face, $A_{cw} = 2x_e h$.

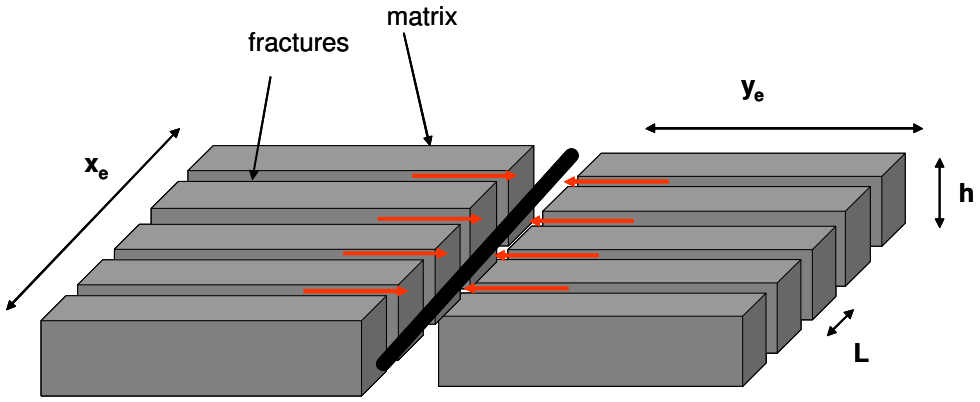

Fig. 3.3 – Schematic of Slab Matrix Linear Model of Hydraulically Fractured Well. Cross-sectional area at well face, $A_{cw} = 2x_e h$.

3.2 Matrix (Slab) Equations

The diffusivity equations for the matrix along with the initial and boundary conditions are given by Eqs. B-4 to B-6 in Appendix B.

$$\frac{\partial^2 p_{DLm}}{\partial z_D^2} = \frac{3}{\lambda_{Ac}}(1-\omega)\frac{\partial p_{Dm}}{\partial t_{DAc}} \qquad \text{.....(3.1)}$$

where $\lambda_{Ac} = \frac{12}{L^2}\frac{k_m}{k_f}A_{cw}$ is the Warren and Root interporosity flow parameter

Initial condition: $p_{DLm}(z_D,0)=0$

Inner boundary: $\left|\frac{\partial p_{DLm}}{\partial z_D}\right|_{z_D=0} = 0$

Outer boundary: $\left|p_{DLm}\right|_{z_D=1} = p_{DLf}$

The dimensionless time and pressure variables are given for the slightly compressible fluid by

$$t_{DAc} = \frac{0.00633 k_f t}{(\phi\mu c_t)_{f+m} A_{cw}} \text{ and } \quad p_{DL} = \frac{k_f \sqrt{A_{cw}}(p_i - p_{wf})}{141.2 qB\mu} \qquad \text{.....(3.2)}$$

and for the gas case by

$$t_{DAc} = \frac{0.00633 k_f t}{(\phi\mu c_t)_{f+m} A_{cw}} \quad , \; m_{DL} = \frac{k_f \sqrt{A_{cw}}\left[m(p_i) - m(p_{wf})\right]}{1422 q_g T},$$

k_f is defined as the bulk fracture permeability of the dual porosity models.

3.3 Fracture Equations

The diffusivity equations for the fracture and the initial and boundary conditions are given by Eq. B-12 in Appendix B. The second term on the right side of the equation represents the source term from the matrix.

$$\frac{\partial^2 p_{DLf}}{\partial y_D^2} = \omega \frac{\partial p_{DLf}}{\partial t_{DAc}} - \frac{\lambda_{Ac}}{3} \left| \frac{\partial p_{DLm}}{\partial z_D} \right|_{z_D=1} \qquad \text{.....(3.3)}$$

Initial condition: $p_{DLf}(y_D, 0) = 0$

Inner boundary: $\left| \frac{\partial p_{DLf}}{\partial y_D} \right|_{y_D=0} = -2\pi$ (constant rate)

Outer boundary: $\frac{\partial p_{DLf}}{\partial y_D}\left(y_e \Big/ \sqrt{A_{cw}}, t_{DAc} \right) = 0$ (no-flow boundary)

3.4 Constant Pressure Inner Boundary Solution

The solution to the system presented in Eqs. 3.1 and 3.3 in Laplace space is given by Eq. B-23 in Appendix B

$$\overline{p_{wDL}} = \frac{2\pi}{s\sqrt{sf(s)}}\left[\frac{1+e^{-2\sqrt{sf(s)}y_{De}}}{1-e^{-2\sqrt{sf(s)}y_{De}}}\right] \qquad \text{……(3.4)}$$

Where $y_{De} = y_e \Big/ \sqrt{A_{cw}}$

In Laplace space, the constant p_{wf} case at the wellbore can be found from the solution for the constant rate case given by Eq. 3.4 using the Van Everdingen and Hurst relation[59] given by Eq 3.5

$$\overline{q_{DL}} = \frac{1}{s^2\overline{p_{wDL}}} \qquad \text{……(3.5)}$$

Eq. 3.5 thus becomes for the constant p_{wf} case

$$\frac{1}{\overline{q_{DL}}} = \frac{2\pi s}{\sqrt{sf(s)}}\left[\frac{1+e^{-2\sqrt{sf(s)}y_{De}}}{1-e^{-2\sqrt{sf(s)}y_{De}}}\right] \qquad \text{……(3.6)}$$

Eq. 3.6 can then be inverted to obtain the solutions as a function of time using suitable Laplace numerical inversion algorithms such as Stehfest's inversion algorithm.[56]

3.5 Convergence Skin

The convergence skin accounts for distortion of the flow from linear to radial around the wellbore and is given by Lichtenberger[60] as

$$s_c = -\ln\left[\frac{\pi r_w}{h}\left(1+\sqrt{\frac{k_V}{k_H}}\right)\sin\left(\frac{\pi d_z}{h}\right)\right] \qquad \text{……(3.7)}$$

where d_z is the distance to the nearest horizontal boundary and k_V and k_H are horizontal and vertical permeabilities respectively.

The effect of including the convergence skin into the linear model is illustrated in Fig. 3.4. This accounts for flow towards an actual horizontal well present in the center of the rectangular reservoir distinct from flow towards a plane in the El-Banbi model.[16]

Fig. 3.4 – Side View of Linear Model (Rectangular Reservoir) with and without Convergence Skin. In the figure on the left, linear flow occurs towards a plane. In the figure on the right, the inclusion of the convergence skin accounts for the distortion of the flowlines from linear to radial around the horizontal wellbore.

Equations for the beginning of the stabilization of the convergence skin in linear flow were derived in Appendix I, and are given by Eqs. I-15 and I-20 for the constant rate and constant p_{wf} cases respectively as

$$t_{DAc} = \frac{h}{8\pi L_w} \qquad \text{constant rate} \qquad \text{.....(3.8)}$$

$$t_{DAc} = \frac{h}{2\pi^3 L_w} \qquad \text{constant } p_{wf} \qquad \text{.....(3.9)}$$

3.6 Validation of Model

In this section, a set of runs will be performed to compare the linear model previously described to *Fekete (WellTest32 Module version 7.0.0.2)*, the numerical simulator *ECLIPSE version 2007.1.* and Ozkan's Laplace space solution[41] for horizontal well in a bounded rectangular reservoir. More extensive tests are described in Appendix E.

The problem is to determine the constant rate transient response of a fully penetrating horizontal well in the center of a bounded rectangular reservoir as in Fig. 3.3. The data for the problem set is given in Table 3.1. For simplicity, the reservoir will be assumed to be homogeneous and the fluid slightly compressible.

Ozkan's Laplace space solution (too lengthy to be reproduced here) is given by Eq. 2.6.42 in his dissertation.[41] This is inverted from Laplace space to yield the dimensionless pressure, p_{DOzkan}. An equation for the pseudoskin factor[41,42] given below is added to p_{DOzkan} to yield the horizontal well response.

$$s = -\frac{1}{2L_D\sqrt{k/k_x}}\ln\left\{4\sin\left[\frac{\pi}{2}\left(2z_{wD}+r_{wzD}\right)\right]\sin\left(\frac{\pi}{2}r_{wzD}\right)\right\} \qquad \text{.....(3.10)}$$

Ozkan's dimensionless pressure and time variables are defined as

$$p_{DOzkan} = \frac{kh\left(p_i - p_{wf}\right)}{141.2qB\mu}, \qquad t_{DOzkan} = 0.00633\frac{kt}{\phi\mu c_t\left(L_w/2\right)^2}$$ where L_w is the length of the horizontal well.

The following is input into Ozkan's model to adapt it to our test case.

$x_{eD} = 2$, $y_{eD} = 1$ (rectangular reservoir dimensions), $L_D = 33.33$, $x_{wD} = 1$, $y_{wD} = 0.5$, $z_{wD} = 0.5$ (location of well in rectangular reservoir). The response is computed at $x_D = 0.732$, $y_D = 0.5$, $z_D = 0.778$. These dimensionless variables are those defined by Ozkan.[41]

where $x_D = \frac{2x}{L_w}\sqrt{\frac{k}{k_x}}, y_D = \frac{2y}{L_w}\sqrt{\frac{k}{k_y}}, z_D = \frac{z}{h}, L_D = \frac{L_w}{2h}\sqrt{\frac{k_z}{k}}, r_{wzD} = \frac{r_w}{h}\sqrt{\frac{k_z}{k_y}}$

It is assumed above that $k_x=k_y=k_z$

Table 3.1 – Dataset for Model Validation Runs.	
r_w	0.25 ft
h	30 ft
ϕ	0.1
k	1 md
p_i	5,000 psi
L_w (x_e)	2,000 ft
y_e	500 ft
q	100 stb/d
B	1 rb/stb
μ	1 cp
c_t	$3x10^{-6}$ psi^{-1}

The results from programming Ozkan's Laplace space solution is checked against the analytical solution given by Eq. 2.6.59 in his dissertation.[41] It can be seen from Fig. 3.5 that our results obtained from using Ozkan's Laplace solution appears to be comparable to the analytical solution.

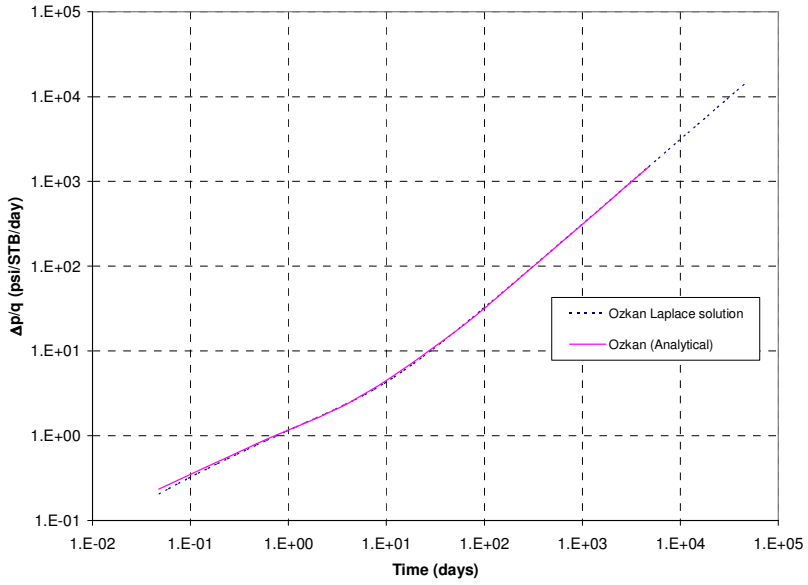

Fig. 3.5 – Verification of Ozkan's Laplace Solution for Horizontal Well in a Rectangular Reservoir. The half-slope linear and pseudoradial regions are shown. The Laplace solution appears to be comparable to the analytical solution.

Our linear model (constant rate) solution is given by Eq. 3.4. with $f(s)=1$ for the homogeneous case. The convergence skin is computed as 2.95 from Eq. 3.7.

$$s_c = -\ln\left[\frac{\pi(0.25)}{30}\left(1+\sqrt{\frac{1}{1}}\right)\sin\left(\frac{\pi(15)}{30}\right)\right] = 2.95$$

This convergence skin is then converted to linear variables using

$$s_{cAc} = s_c \frac{\sqrt{A_{cw}}}{L_w} = 2.95\frac{\sqrt{120{,}000}}{2000} = 0.51$$

This value is added to the dimensionless pressure using Eq. 3.11

$$p_{wDL} = p_{DL} + 2\pi s_{cAc} \qquad \text{.....(3.11)}$$

The 2π in the definition for skin was given by El-Banbi[16] and will be adopted in the current work.

The dimensionless linear model variables given in Eq. 3.2 is used to convert the results to pressure and time.

The results from the runs are given in Fig. 3.6. It can be observed from Fig 3.6 that the linear model (with convergence skin) matches Fekete and ECLIPSE but differs from Ozkan's solutions. It is believed that the Ozkan solution differs because of his equation for pseudoskin factor which might not properly account for the convergence skin.

It can thus be concluded that our linear model with the inclusion of the convergence skin is valid for the purposes of this work.

The beginning of the stabilization of the convergence skin can be computed for this example from Eq. 3.8 as

$$t_{DAc} = \frac{h}{8\pi L_w} = \frac{30}{8(\pi)(2{,}000)} = 0.000597 \qquad \text{.....(3.12)}$$

The time of intersection of the radial and linear flow periods is determined from the derivative in Fig. 3.6 as 0.00314 days. This time yields a dimensionless time of

$$t_{DAc} = \frac{0.00633(1)(0.00314)}{(0.1)(1)(3x10^{-6})(120{,}000)} = 0.000552 \qquad \text{.....(3.13)}$$

where $A_{cw} = 2(2{,}000)(30) = 120{,}000\, ft^2$

The dimensionless time computed in Eq. 3.13 is similar to that computed from Eq. 3.12. It can thus be concluded that Eq. 3.8 is appropriate.

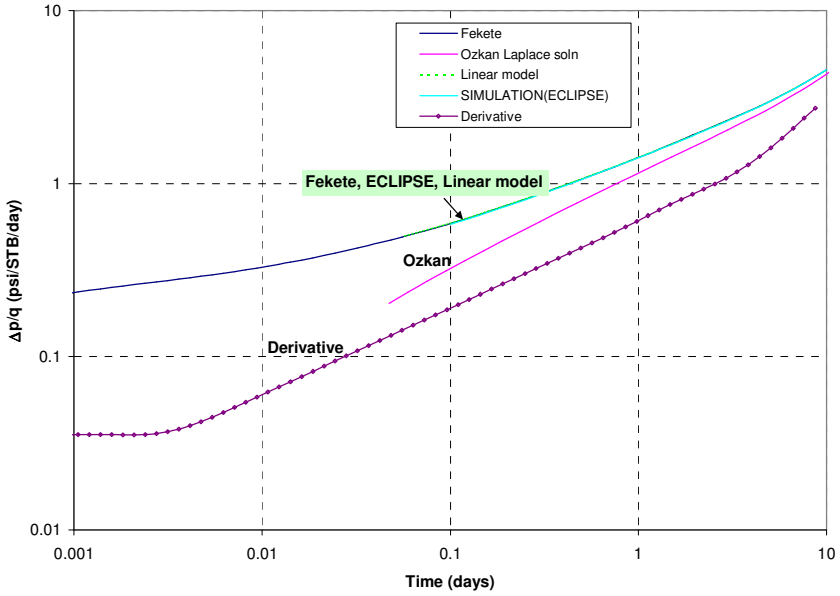

Fig. 3.6 – Comparison of Linear model (homogeneous, zero skin, closed) with Fekete, ECLIPSE and Ozkan Laplace solution. The convergence skin has been added on to the linear model. The Linear model matches Fekete and ECLIPSE but differs from Ozkan's solution.

CHAPTER IV

DEVELOPMENT OF ANALYSIS EQUATIONS

4.1 Introduction

The model used to represent the multi-stage hydraulically fractured shale gas well has been described in Chapter III. It should be noted that the slab matrix geometry (shown in Fig. 3.3) is used in this work since it is most commonly used in the literature. Applications to the other matrix geometry types (two-dimensional: cylinder, columns; three-dimensional: sphere, cubes) will be demonstrated in Chapter V. The linear dual porosity model given in El-Banbi[16] will be used as a basis for the work in this chapter. The mathematical details of this linear dual porosity model are given in Appendix B.

From Eq. 3.6 and B-25, the Laplace space solution for the constant pressure inner boundary, closed outer boundary reservoir (slab matrix) is given by

$$\frac{1}{\overline{q}_{DL}} = \frac{2\pi s}{\sqrt{sf(s)}}\left[\frac{1+e^{-2\sqrt{sf(s)}y_{De}}}{1-e^{-2\sqrt{sf(s)}y_{De}}}\right] \qquad \text{.....(4.1)}$$

where dimensionless variables are defined as

$$\frac{1}{q_{DL}} = \frac{k_f\sqrt{A_{cw}}\left[m(p_i)-m(p_{wf})\right]}{1422 q_g T}, \quad y_{De} = \frac{y_e}{\sqrt{A_{cw}}} \qquad \text{.....(4.2)}$$

where s is the Laplace space variable and the inverse is $t_{DAc} = \dfrac{0.00633 k_f t}{(\phi\mu c_t)_{f+m} A_{cw}}$

Additionally for the slab matrix case,

$$f(s) = \omega + \sqrt{\frac{\lambda_{Ac}}{3s}(1-\omega)}\tanh\sqrt{\frac{3(1-\omega)s}{\lambda_{Ac}}} \qquad \text{.....(4.3)}$$

The dual porosity parameters are given by $\lambda_{Ac} = \frac{12}{L^2}\frac{k_m}{k_f}A_{cw}$ and $\omega = \frac{(\phi c_t)_f}{(\phi c_t)_f + (\phi c_t)_m}$

A parametric study conducted with the linear model given by Eq. 4.1 is summarized in Figs. 4.1 and 4.2. Figs. 4.1 and 4.2 show results for reservoir sizes y_{De} = 1 and 100 for ranges of ω (10^{-3} and 10^{-7}) and λ_{Ac} (10^{-3},10^{-5} and 10^{-7}). The homogeneous case (ω=1) is also added to the plot.

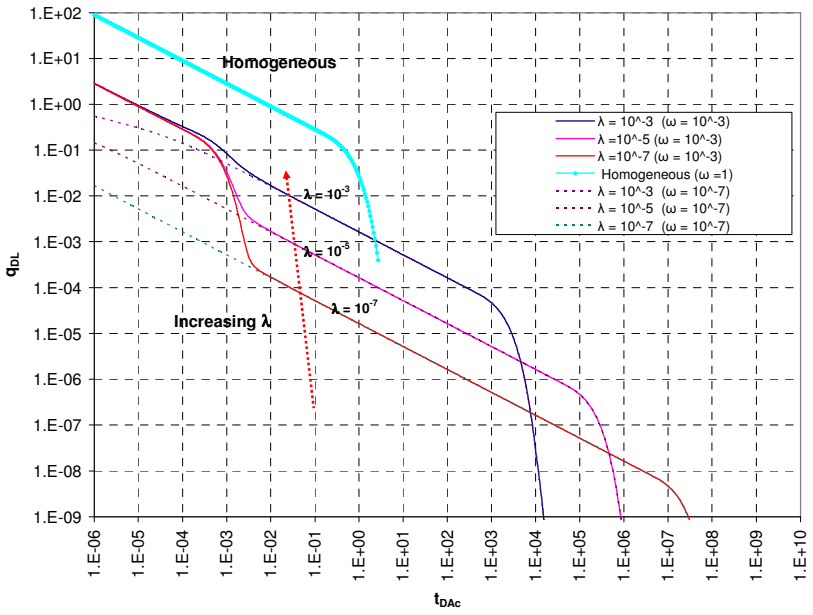

Fig. 4.1 – Effect of ω and λ_{Ac} on Linear Model Response (y_{De} = 1). λ_{Ac} =10^{-3}, 10^{-5},10^{-7} for values of ω = 10^{-3} and 10^{-7}. There is no effect of ω on the late time transient linear response for a fixed λ_{Ac}.

It can be observed from Fig. 4.1 that the homogeneous response is above the dual porosity response. It can also be observed that for $\omega = 10^{-3}$, all the responses for λ_{Ac} = 10^{-3}, 10^{-5},10^{-7} converge to the same initial half-slope (indicative of linear flow in the fractures) at early times and different half slopes at later times. The half slope at later times is indicative of linear flow in the matrix. As ω decreases to 10^{-7} (dotted lines), the common initial half slope disappears and the responses show only the late time half slopes. The late time responses for each of the λ_{Ac} is similar for $\omega = 10^{-3}$ and 10^{-7}. It can thus be concluded that there is no effect of ω on the late time transient response for a particular λ_{Ac}. It can also be concluded that the initial half slope region preceding the later time half slope region is only evident as λ_{Ac} and ω increases.

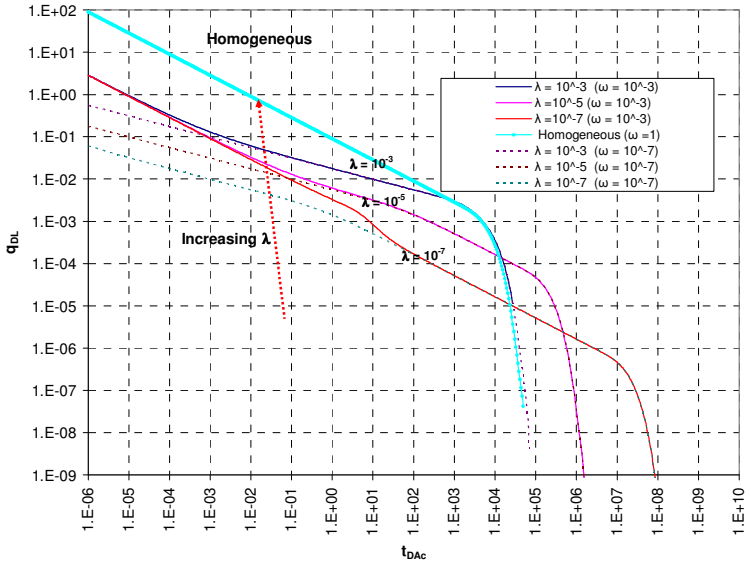

Fig. 4.2 – Effect of ω and λ_{Ac} on Linear Model Response (y_{De} = 100). λ_{Ac} =10^{-3}, 10^{-5}, 10^{-7} for values of $\omega = 10^{-3}$ and 10^{-7} The parameters ω and λ_{Ac} affect the transient response significantly.

The parameters in Fig. 4.2 are similar to Fig. 4.1 except that y_{De} has increased from 1 to 100. Similar to Fig. 4.1, the homogeneous response is above the dual porosity response. It can be observed from Fig. 4.2 that the $\omega = 10^{-3}$ cases also indicate the common initial half-slope and then progressively indicate a quarter slope (bilinear flow caused by simultaneous linear flow in the matrix and fractures). The $\lambda_{Ac}=10^{-5}$, $\omega=10^{-3}$ and $\lambda_{Ac} = 10^{-7}$, $\omega=10^{-3}$ cases indicate a bilinear flow followed by linear flow (half-slope). As ω decreases to 10^{-7} (dotted lines) , the early linear flow disappears and the only transient responses are bilinear ($\lambda_{Ac}=10^{-3}$, $\omega=10^{-7}$) and bilinear followed by linear ($\lambda_{Ac}=10^{-5}$, $\omega=10^{-7}$ and $\lambda_{Ac}=10^{-7}$, $\omega=10^{-7}$).

It appears that relatively large λ_{Ac} and ω result only in the bilinear transient flow. As λ_{Ac} and ω decrease, bilinear followed by an increasing transient linear regime is observed.

It can be concluded from Figs. 4.1 and 4.2 that relatively smaller y_{De} reservoirs exhibit long periods of late-time transient linear flow only as shown in Fig. 4.1 and bilinear flow occurs with large reservoirs.

There are thus five flow regions identified and equations are subsequently presented for each region. All the equations are derived beginning with Eq. 4.1. The details of the development are shown in Appendix C. The flow regimes are illustrated in Fig. 4.3.

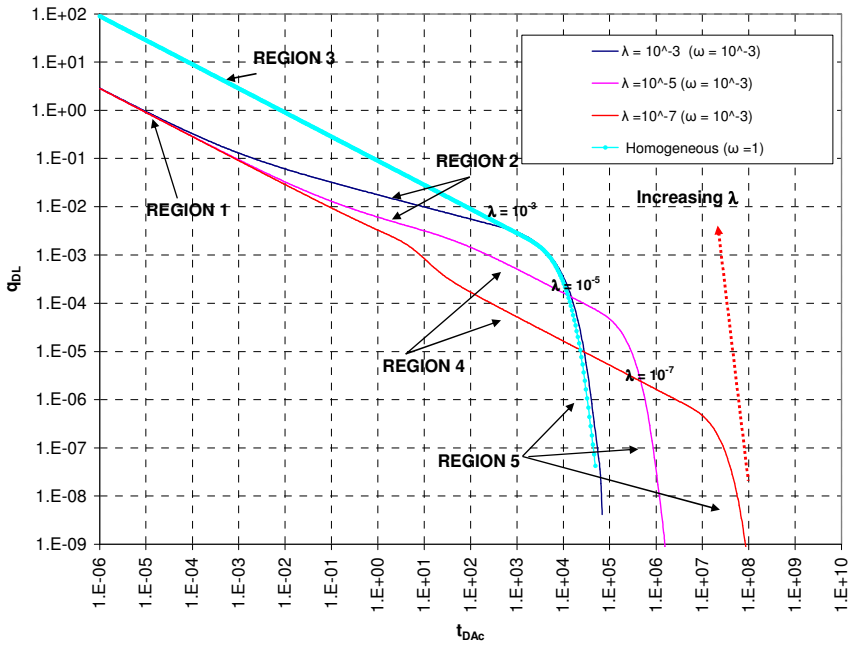

Fig. 4.3 – Illustration of the Five Flow Regions. This is the same case as in Fig. 4.2 for (y_{De} = 100). λ_{Ac} =10^{-3}, 10^{-5}, 10^{-7} for values of ω= 10^{-3}.

4.2 Region 1

This represents early transient linear flow in the fracture system only. There is negligible drainage from the matrix. This occurs at early times as shown in Fig 4.3. As shown in Eq. C-11 in Appendix C-1, the equation is given by

$$q_{DL} = \frac{1}{2\pi\sqrt{\pi t_{DAc}/\omega}} \qquad \text{.....(4.4)}$$

and the approximate valid range is given by Eq. C-17

$$0 < t_{DAc} < \frac{y_{De}^2 \omega}{9} \qquad \text{.....(4.5)}$$

Applying the dimensionless pressure and time definitions given in Eq. 4.2 to convert Eq. 4.4 to usual variables yields

$$\sqrt{k_f}\,A_{cw} = \frac{1262T}{\sqrt{\omega(\phi\mu c_t)_{f+m}}}\frac{1}{\tilde{m}_1} \qquad \text{……(4.6)}$$

Where $\tilde{m}_1$ is the slope obtained from a plot of $\frac{\lfloor m(p_i) - m(p_{wf})\rfloor}{q_g}$ against $\sqrt{t}$

If Region 1 is observed, Eq. 4.6 may be used to determine the fracture permeability if the other parameters are known.

4.3 Region 2

This represents bilinear flow caused by simultaneous transient flow in the fracture system and matrix. It is indicated by a one-quarter slope on a log-log plot as shown in Fig. 4.3. As shown in Eq. C-27 in Appendix C-2, the equation is given by

$$q_{DL} = \frac{\lambda_{Ac}^{0.25}}{10.133\, t_{DAc}^{0.25}} \qquad \text{……(4.7)}$$

This region has been found occur only when $y_{De} > \sqrt{3/\lambda_{Ac}}$. Otherwise it bends down to Region 4 as shown in Fig. 4.3. This region is valid approximately when $t_{DAc} < \frac{1}{3\lambda_{Ac}}$ or

when $t_{DAc} < \left(\frac{y_{De}}{3}\right)^4 \frac{\lambda_{Ac}}{3}$ ……(4.8)

as shown in the derivations given in Appendix C (Eq. C-36)

Applying the dimensionless pressure and time definitions given in Eq. 4.2 to convert Eq. 4.7 to usual variables yields

$$\sqrt{k_f}\,A_{cw} = \frac{4064T}{\left[\sigma k_m (\phi\mu c_t)_{f+m}\right]^{0.25}} \frac{1}{\tilde{m}_2} \qquad \text{.....(4.9)}$$

Where $\tilde{m}_2$ is the slope obtained from a plot of $\frac{\lfloor m(p_i) - m(p_{wf})\rfloor}{q_g}$ against $t^{0.25}$

If Region 2 is observed, Eq. 4.9 may be used to determine the fracture permeability and the shape factor, σ, if the other parameters are known.

4.4 Region 3

This represents the homogeneous reservoir case response (An equation for the complete analytical homogeneous reservoir transient response is given in Appendix D). This is also indicated by a one-half slope on a log-log plot as shown in Fig. 4.3. As shown in Appendix C-3, the equation is given by Eq. C-44

$$q_{DLh} = \frac{1}{2\pi\sqrt{\pi t_{DAch}}} \qquad \text{.....(4.10)}$$

Where $\frac{1}{q_{DLh}} = \frac{k\sqrt{A_{cw}}\left[m(p_i) - m(p_{wf})\right]}{1422 q_g T}$; $t_{DAch} = \frac{0.00633kt}{(\phi\mu c_t)A_{cw}}$ and k is the homogeneous reservoir permeability.

This region has been found occur only when $y_{De} \geq \sqrt{3\omega/\lambda_{Ac}}$.

This region is valid approximately when $t_{DAch} < \frac{y_{De}^2}{9}$ .....(4.11)

as shown in the derivations given in Appendix C (Eq. C-50)

Applying the dimensionless pressure and time definitions given in Eq. 4.2 to convert Eq. 4.10 to usual variables yields

$$\sqrt{k}A_{cw} = \frac{1262T}{\sqrt{(\phi\mu c_t)_{f+m}}}\frac{1}{\tilde{m}_3} \quad \text{.....(4.12)}$$

where $\tilde{m}_3$ is the slope obtained from a plot of $\frac{|m(p_i) - m(p_{wf})|}{q_g}$ against $\sqrt{t}$

If Region 3 is observed, Eq. 4.12 may be used to determine the bulk reservoir permeability if the other parameters are known.

4.5 Region 4

This represents the transient linear case when the transient response is primarily from drainage of the matrix from the outer edges towards the matrix block centers. This is also indicated by a one-half slope on a log-log plot as shown in Fig. 4.3. As shown in Appendix C-4, the equation is given by Eq. C-61

$$q_{DL} = \frac{1}{2\pi\sqrt{\pi t_{DAc}}}\sqrt{\frac{\lambda_{Ac}}{3}}y_{De} \quad \text{.....(4.13)}$$

and the approximate valid range is given by Eq. C-73

$$\frac{\lambda_{Ac}}{3}\left(\frac{y_{De}}{0.5}\right)^4 < t_{DAc} < \frac{1}{3\lambda_{Ac}} \quad \text{.....(4.14)}$$

Applying the dimensionless pressure and time definitions given in Eq. 4.2 to convert Eq. 4.13 to usual variables along with Eqs. 4.15 and 4.16 (for the slab matrix case) yields Eq. 4.17

$$\lambda_{Acw} = \frac{12}{L^2}\frac{k_m}{k_f}A_{cw} \quad \text{.....(4.15)}$$

$$A_{cw} = \frac{L}{2y_e}A_{cm} \quad \text{.....(4.16)}$$

$$\sqrt{k_m}A_{cm} = \frac{1262T}{\sqrt{(\phi\mu c_t)_m}}\frac{1}{\tilde{m}_4} \qquad \text{.....(4.17)}$$

where $\tilde{m}_4$ is the slope obtained from a plot of $\frac{\lfloor m(p_i) - m(p_{wf})\rfloor}{q_g}$ against $\sqrt{t}$. It is also assumed that $(\phi\mu c_t)_{f+m} \approx (\phi\mu c_t)_m$ If Region 4 is observed, Eq. 4.17 may be used to determine the matrix drainage area, A_{cm}, if the other parameters are known.

It should be noted that Eq. 4.13 can be written as

$$q_{DLm} = \frac{1}{2\pi\sqrt{\pi t_{DAcm}}} \qquad \text{.....(4.18)}$$

where $\frac{1}{q_{DLm}} = \frac{k_m\sqrt{A_{cm}}\left[m(p_i) - m(p_{wf})\right]}{1422 q_g T}$; $t_{DAcm} = \frac{0.00633 k_m t}{(\phi\mu c_t)_m A_{cm}}$ and k_m is the reservoir matrix permeability.

Eq. 4.18 can easily be converted to Eq. 4.17.

This implies that Region 4 depends only on matrix properties k_m and A_{cm} and is not affected by fracture flow properties.

4.6 Region 5

This represents the period when the reservoir boundary begins to influence the transient response as shown in Fig. 4.3. The transient response in the matrix blocks have reached their central inner no-flow symmetry lines. No equation is presented for this region in this study. Unlike the slightly compressible fluid case (liquid), the use of pseudopressure relations for gas to linearize and solve the diffusivity equation will only be accurate for the transient regions (Regions 1 to 4). The boundary dominated Region 5 requires the use of the following equations simultaneously.

$$q_g = J_{CP}\left[m(\bar{p}) - m(p_{wf})\right] \qquad \text{.....(4.18)}$$

where J_{CP} is the productivity index for the constant pressure case.

and

$$\frac{\bar{p}}{z} = \left(\frac{\bar{p}}{z}\right)_i \left[1 - \frac{G_p}{G}\right] \qquad \text{.....(4.19)}$$

Which is the material balance equation for a closed gas reservoir.

All the derived equations are summarized in Tables 4.1. A summary of the equivalent equations for the constant rate inner boundary case is also presented in Table 4.2.

Table 4.1 – Summary of Analysis Equations for the Constant p_{wf} Inner Boundary Case (Slab Matrix).

Region	**Equation**	**Analysis Equation** $\frac{m(p_i)-m(p_{wf})}{q_g} vs \sqrt{t}$
1 – Early linear (fracture)	$q_{DL}=\frac{1}{2\pi\sqrt{\pi t_{DAc}/\omega}}$	$\sqrt{k_f}A_{cw}=\frac{1262T}{\sqrt{\omega(\phi\mu c_t)_{f+m}}}\frac{1}{\tilde{m}_1}$
2 – Bilinear	$q_{DL}=\frac{\lambda_{Ac}^{0.25}}{10.133\ t_{DAc}^{0.25}}$	* $\sqrt{k_f}A_{cw}=\frac{4070T}{\left[\sigma k_m(\phi\mu c_t)_{f+m}\right]^{0.25}}\frac{1}{\tilde{m}_2}$
3 – Homogeneous	$q_{DLh}=\frac{1}{2\pi\sqrt{\pi t_{DAch}}}$	$\sqrt{k}A_{cw}=\frac{1262T}{\sqrt{(\phi\mu c_t)}}\frac{1}{\tilde{m}_3}$
4 – Matrix transient linear	$q_{DL}=\frac{1}{2\pi\sqrt{\pi t_{DAc}}}\sqrt{\frac{\lambda_{Ac}}{3}}y_{De}$ or $q_{DLm}=\frac{1}{2\pi\sqrt{\pi t_{DAcm}}}$	$\sqrt{k_m}A_{cm}=\frac{1262T}{\sqrt{(\phi\mu c_t)_{f+m}}}\frac{1}{\tilde{m}_4}$
5 – Boundary-dominated	----------	----------

* This case is the $\frac{m(p_i)-m(p_{wf})}{q_g}$ vs $\sqrt[4]{t}$ plot

Table 4.2 – Summary of Analysis Equations for the Constant Rate Inner Boundary Case (Slab Matrix).

Region	Equation	Analysis Equation $\frac{m(p_i)-m(p_{wf})}{q_g} vs \sqrt{t}$
1 – Early linear (fracture)	$p_{WDL} = 4\sqrt{\pi_{DAc}/\omega}$	$\sqrt{k_f}A_{cw} = \frac{803.2T}{\sqrt{\omega(\phi\mu c_t)_{f+m}}}\frac{1}{\tilde{m}_1}$
2 – Bilinear	$p_{WDL} = 9.123\frac{t_{DAc}^{0.25}}{\lambda_{Ac}^{0.25}}$	* $\sqrt{k_f}A_{cw} = \frac{3664T}{\left[\sigma k_m(\phi\mu c_t)_{f+m}\right]^{0.25}}\frac{1}{\tilde{m}_2}$
3 – Homogeneous	$p_{WDLh} = 4\sqrt{\pi_{DAch}}$	$\sqrt{k}A_{cw} = \frac{803.2T}{\sqrt{(\phi\mu c_t)}}\frac{1}{\tilde{m}_3}$
4 – Matrix transient linear	$p_{WDL} = 4\sqrt{\frac{3}{\lambda_{Ac}}}\frac{1}{y_{De}}\sqrt{\pi_{DAc}}$ Or $p_{WDLm} = 4\sqrt{\pi_{DAcm}}$	$\sqrt{k_m}A_{cm} = \frac{803.2T}{\sqrt{(\phi\mu c_t)_{f+m}}}\frac{1}{\tilde{m}_4}$
5 – Boundary-dominated	-----	------

* This case is the $\frac{m(p_i)-m(p_{wf})}{q_g}$ vs $\sqrt[4]{t}$ plot

The effect of y_{De} on Region 4 response is shown in Figs. 4.4 to 4.7. The slab matrix dual porosity linear reservoir transient response is compared with the equations for Region 3 [$q_{DL} = \frac{1}{2\pi\sqrt{\pi t_{DAc}}}$] and Region 4 [$q_{DL} = \frac{1}{2\pi\sqrt{\pi t_{DAc}}}\sqrt{\frac{\lambda_{Ac}}{3}}y_{De}$] in Figs. 4.4 and 4.5 to show the effect of small (y_{De} = 1) and relatively larger (y_{De} = 10^5) reservoirs. It can be observed that for the small reservoir in Fig. 4.4, the slab matrix response matches the equation for Region 4. For the larger reservoir in Fig. 4.5, the slab matrix response indicates a bilinear region at early times and matches the equation for Region 3 at later times.

The slab matrix dual porosity transient response is shown in Figs. 4.6 and 4.7 for several values of y_{De}. It can be observed from Fig. 4.6 and 4.7 that the transient response for Region 4 curves downwards when $y_{De} < \sqrt{3\omega/\lambda_{Ac}}$ and is not evident when $y_{De} \geq \sqrt{3/\lambda_{Ac}}$.

4.7 Summary

Five flow regions have been identified with the linear dual porosity model and derived equations were presented for four of the regions. Analysis equations were also presented for the region along with the criteria for existence of each of these regions. It has been shown that the dimensionless reservoir size, y_{De} has an important effect on Region 4 transient response.

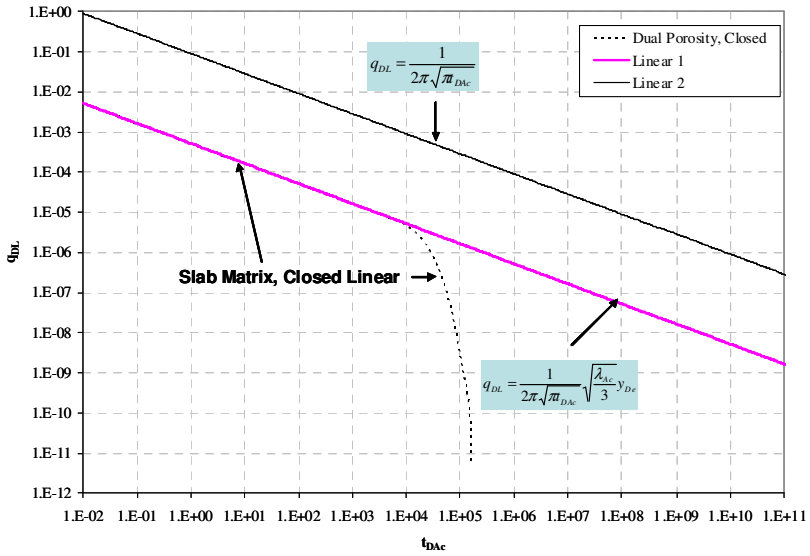

Fig. 4.4 – Effect of Small Reservoir Size on Region 4 (y_{De} = 1, λ_{Ac} =10^{-4}, ω = 10^{-5}). The half slope region on the slab matrix (dual porosity, constant p_{wf}, closed) response matches the equation shown previously for Region 4.

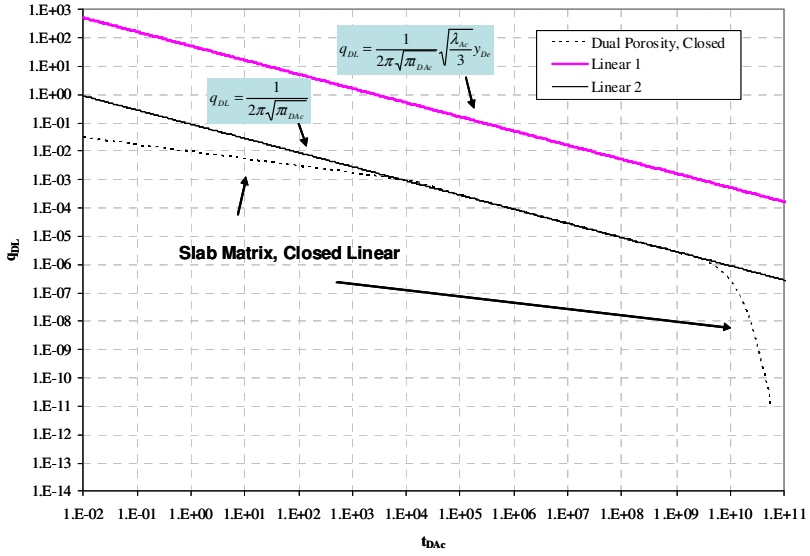

Fig. 4.5 – Effect of Large Reservoir Size on Region 4 (y_{De} = 10^{5},λ_{Ac} =10^{-4} , ω = 10^{-5}). The half slope region on the slab matrix (dual porosity, constant p_{wf}, closed) response matches the equation shown previously for Region 3 (homogeneous) and not that for Region 4 as shown in Fig. 4.4.

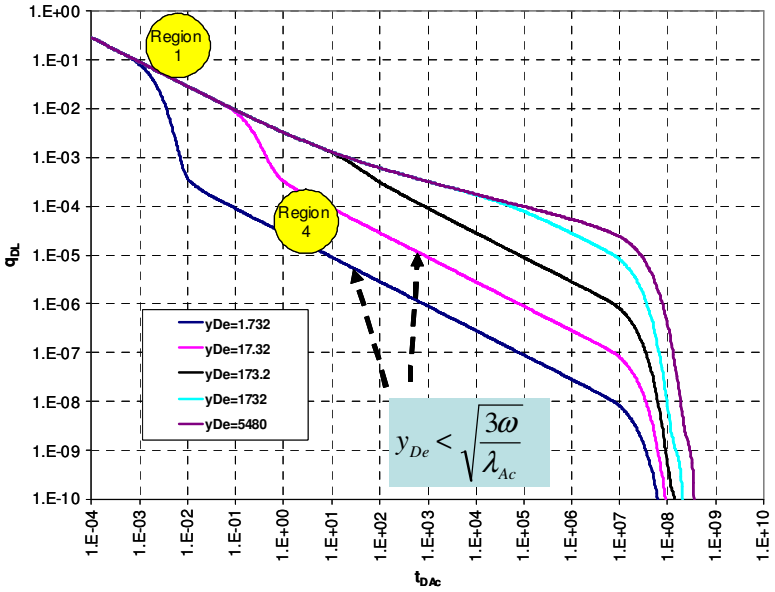

Fig. 4.6 – Effect of y_{De} (Case A - slab matrix dual porosity, constant p_{wf}, closed). The usual half slope (Region 4) initially curves down only when $y_{De} < \sqrt{3\omega/\lambda_{Ac}}$.

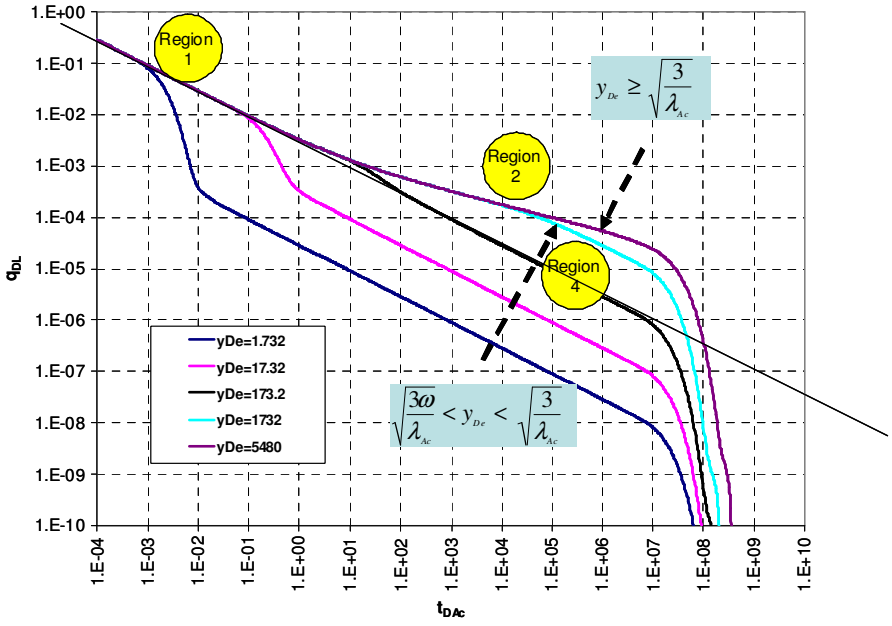

Fig. 4.7 – Effect of y_{De} (Case B - slab matrix dual porosity, constant p_{wf}, closed). There is no evident half slope (Region 4) when $y_{De} \geq \sqrt{3/\lambda_{Ac}}$ but a bilinear region (Region 2).

CHAPTER V

TRANSIENT LINEAR FLOW REGIME (REGION 4)

5.1 Introduction

The transient linear regime is the regime in which the response is dominated by matrix drainage and was described as Region 4 in Chapter IV. Matrix block drainage of different geometries have been shown in detail to exhibit the transient linear drainage in Appendix A. This chapter deals with Region 4 in detail and summarizes the effects of shape factors and area-volume ratios. A preliminary procedure is presented for analyzing field data with zero skin and is illustrated with a synthetic case.

5.2 Effect of Shape Factors

The term shape factor as used in this work refers to the parameter first presented by Warren and Root[18] to describe matrix geometry and utilized in their pseudosteady-state matrix-transfer equation. Several authors[61-69] have investigated and shown their values for these shape factors. The Warren and Root shape factors have been factored into the commonly used transient dual porosity models (illustrated in Appendix B). It will be shown that other shape factors can be factored into the transient dual porosity models with consistent appropriate modifications. In this work, the shape factors given by Warren and Root, Kazemi and Zimmerman will be used for comparison.

As previously mentioned, the Warren and Root shape factor formulation for the slab matrix geometry ($12/L^2$) is inherent in *f(s)* as shown in Appendix B. The Kazemi and Zimmerman relations for the shape factor can be similarly substituted into the transient dual porosity model as was shown in Appendix B. This is summarized in Table 5.1.

Table 5.1 - Summary of *f(s)* Formulations for the Slab Matrix Case.

Author	**Shape Factor**	***f(s)***
Warren and Root	$\frac{12}{L_1^2}$	$f(s)=\omega+\sqrt{\frac{\lambda}{3s}(1-\omega)}\tanh\sqrt{\frac{3(1-\omega)s}{\lambda}}$
Kazemi	$\frac{4}{L_1^2}$	$f(s)=\omega+\sqrt{\frac{\lambda}{s}(1-\omega)}\tanh\sqrt{\frac{(1-\omega)s}{\lambda}}$
Zimmerman	$\frac{\pi^2}{L_1^2}$	$f(s)=\omega+\sqrt{\frac{4}{\pi^2}\frac{\lambda}{s}(1-\omega)}\tanh\sqrt{\frac{\pi^2}{4}\frac{(1-\omega)s}{\lambda}}$

The generalized test run procedure is illustrated for the slab matrix, rectangular geometry reservoir case with the Warren and Root shape factor case. It was previously illustrated for the radial geometry case.[70] The dataset is given in Table 5.2.

a) Select a shape factor formulation (e.g. Warren and Root)

b) Compute a value for the shape factor (e.g. slab matrix) $\sigma=\frac{12}{(50)^2}=4.8x10^{-3}$

c) Compute λ : $\lambda_{Ac}=\sigma\frac{k_m}{k_f}A_{cw}=\left(4.8x10^{-3}\right)\frac{\left(10^{-5}\right)}{(100)}\left(8x10^{5}\right)=3.84x10^{-4}$

d) Ensure appropriate *f(s)* from Table 5.1 (in this case, Warren and Root) is programmed in transient dual porosity model.

e) Run program with computed λ_{Ac} and given ω.

Table 5.2 – Shape Factor Example Calculation Dataset.	
x_e	2000 ft
y_e	500 ft
h	200 ft
L	50 ft
k_f	100 md
k_m	10^{-5} md
ω	10^{-3}
Computed Values	
y_{De}	0.559
σ *(slab case)*	0.0012 ft^{-2}
λ_{Ac} *(slab case)*	3.84×10^{-4}
A_{cw}	8×10^5 ft^2

The results from the runs are compared in Fig. 5.1. It can be observed from Fig. 5.1 that the different shape factor formulations – Warren and Root, Kazemi and Zimmerman - result in the same transient linear response. It can thus be concluded that any shape factor formulation can be utilized as long as the appropriate *f(s)* formulation is used along with the consistent λ_{Ac} equation and calculations. More importantly, programs that have the Warren and Root formulation correctly programmed can be utilized. This conclusion has also been verified for the cylinder and sphere geometries.

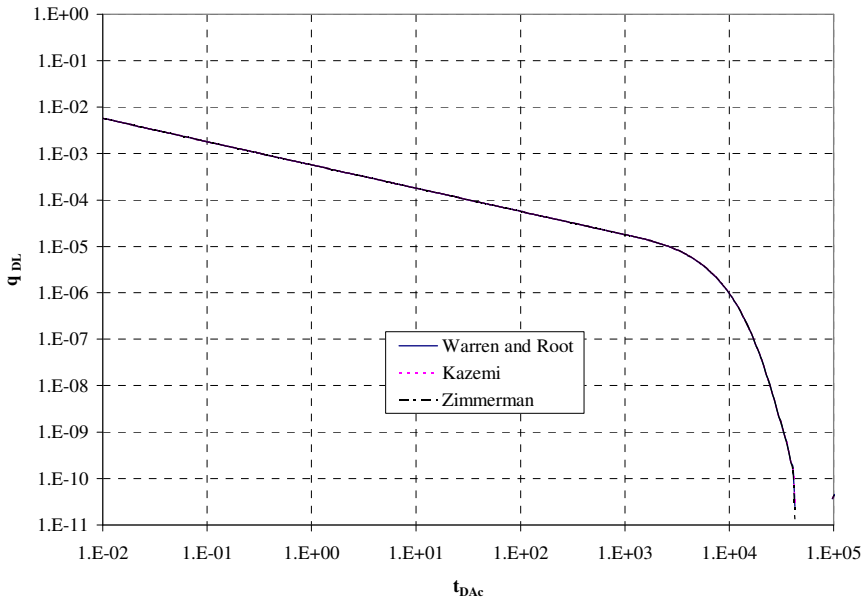

Fig. 5.1 - Effect of Shape Factors on Transient Linear Response (slab matrix case; ω=10^{-3}; W&R : λ_{Ac} =3.84x10^{-4}; Kazemi : λ_{Ac} =1.28x10^{-4}; Zimmerman : λ_{Ac} =3.16x10^{-4}). The shape factors result in the same transient linear response once the corresponding *f(s)* changes are made consistent with the λ_{Ac} definition.

5.3 Effect of Area-Volume Ratio

In this section, the transient dual porosity response of different matrix geometry (slab, cylinder and sphere) will be compared. Two cases are presented.

Case 1 is one in which the different matrix geometry transient dual porosity models are run with the same λ_{Ac} (3.84x10^{-4}). The dataset is the same as in Table 5.2. The Warren and Root shape factors were used for the three matrix geometries. Slab: $12/L^2$, Cylinder: $32/D^2$, Sphere : $60/D^2$. The results are presented in Figs. 5.2 and 5.3. It can be observed that the transient linear responses are different for all the geometries.

Case 2 is one in which the area-volume ratios for all the three matrix geometry are made equivalent. The dataset is given in Table 5.3. The area-volume ratios are given thus:

Slab (One-dimensional) $\frac{2}{L_1}$

Cylinder/Column (Two-dimensional) $\frac{4}{D}$ or $\frac{4}{L_2}$

Sphere/Cube (Three-dimensional) $\frac{6}{D}$ or $\frac{6}{L_3}$

It is noticed that the area-volume ratios for the two-dimensional case, $4/D$ and $4/L_2$ will be the same if the fracture spacings D and L_2 are equivalent. This observation also applies to the three-dimensional cases if D and L_3 are equivalent. This allows the use of transient dual porosity models with the cylinder and sphere as good approximations for the two-dimensional and three-dimensional cases (since the transient dual porosity models are actually developed and programmed with simpler cylinder and sphere geometries instead of the more realistic column and cube geometries).

Dimensions for the slab, cylinder and sphere were selected as 50, 100 and 150 ft respectively to ensure similar area/volume ratios of 0.04. The parameter, λ_{Ac} is computed for each geometry and then run in the transient dual porosity model. The results are presented in Figs. 5.4 and 5.5. It can be observed that the initial transient linear responses are similar for all the geometries before the effect of the boundary.

Table 5.3 – Case 2 Calculation Dataset.	
x_e	2000 ft
y_e	500 ft
h	200 ft
L	50 ft
D_c	100 ft
D_s	150 ft
k_f	100 md
k_m	10^{-5} md
ω	10^{-3}
Computed Values	
y_{De}	0.559
A_{cw}	$8x10^5$ ft^2

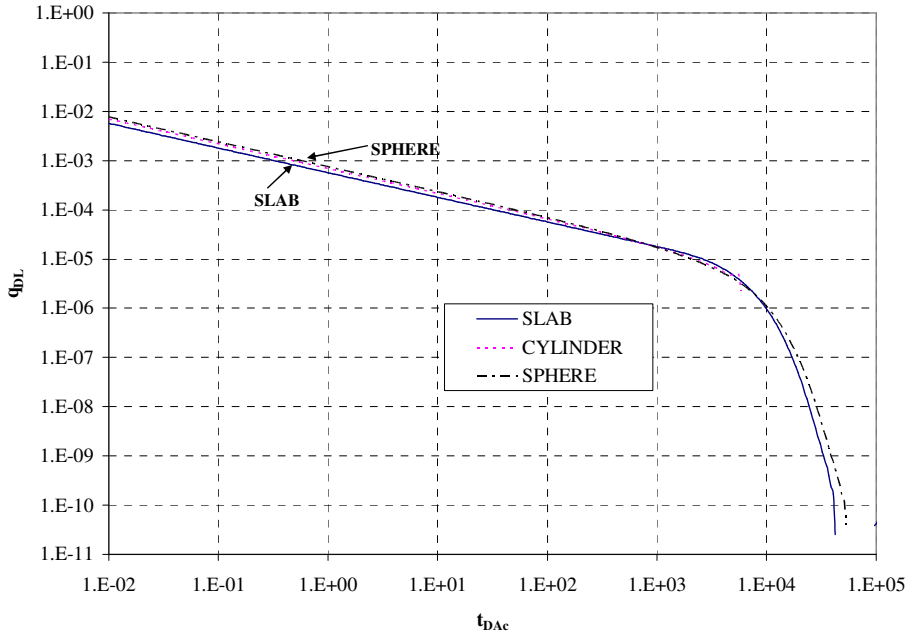

Fig. 5.2 - Log-log Plot of q_{DL} against t_{DAC} - Effect of Matrix Geometry on Transient Response Case 1. Similar λ_{Ac} (ω=10^{-3}; λ_{Ac} =$3.84x10^{-4}$). The three geometries result in different transient linear responses.

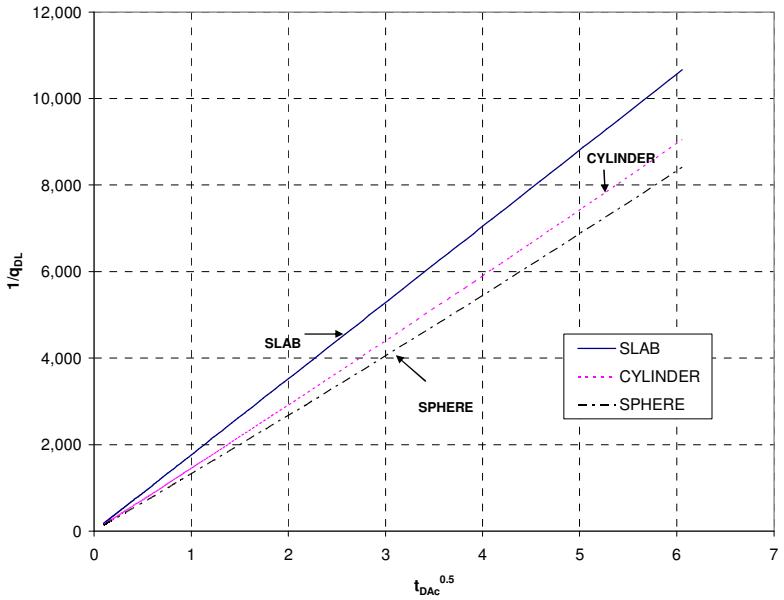

Fig. 5.3 – Specialized Plot of $1/q_{DL}$ against $t_{DAc}^{0.5}$ - Effect of Matrix Geometry on Transient Response Case 1. Similar λ_{Ac} (ω=10^{-3}; λ_{Ac} =3.84x10^{-4}). The three geometries result in different transient linear responses.

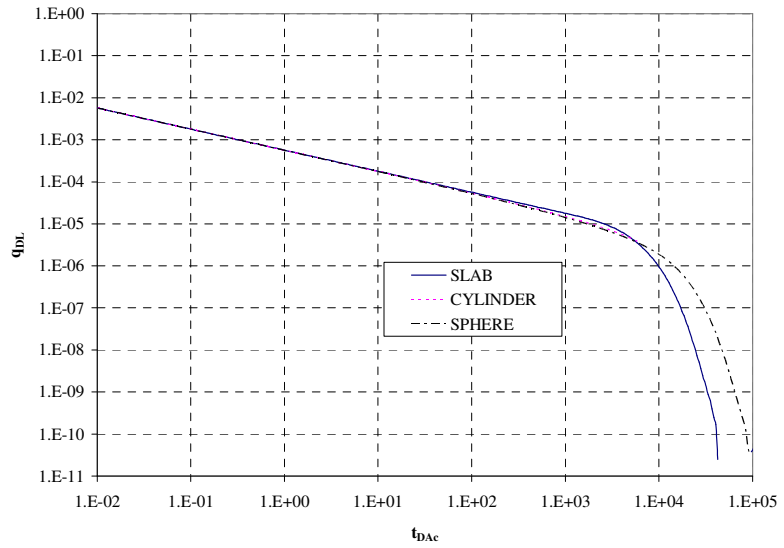

Fig. 5.4 – Log-log Plot of q_{DL} against t_{DAc} - Effect of Matrix Geometry on Transient Response Case 2. Area-volume ratio is 0.04 for all geometries. (slab : λ_{Ac} = 3.84x10^{-4}; L=50 ft; cylinder: λ_{Ac} = 2.56x10^{-4}, D =100 ft; sphere: λ_{Ac} = 2.13x10^{-4}, D=150 ft). The three geometries result in similar initial transient linear responses.

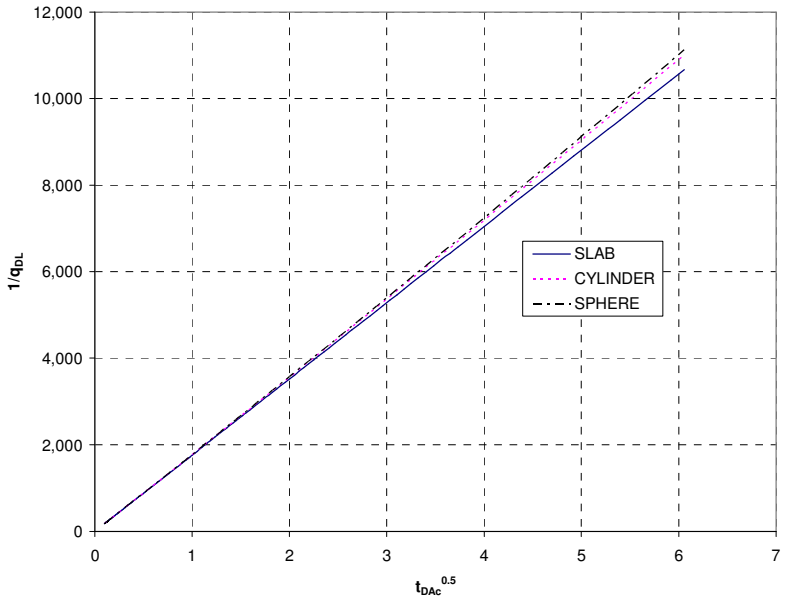

Fig. 5.5 – Specialized Plot of $1/q_{DL}$ against $t_{DAc}^{0.5}$ - Effect of Matrix Geometry on Transient Response Case 2. Area-volume ratio is 0.04 for all geometries. (slab : λ_{Ac} = 3.84x10^{-4}; L=50 ft; cylinder: λ_{Ac} = 2.56x10^{-4}, D=100 ft; sphere: λ_{Ac} = 2.13x10^{-4}, D=150 ft). The three geometries result in similar initial transient linear responses.

The results from these cases illustrate the importance of the area-volume ratio in obtaining similar transient linear response from any matrix geometry. This significant result ensures that we can develop a method for analysis of the transient linear regime for geometry that incorporates the area-volume ratio.

It can be concluded that the matrix drainage area, A_{cm} has to be the same for all matrix geometries in order to achieve the same transient linear response.

It can also be concluded that for the same reservoir, the fracture spacings for the one, two and three-dimensional matrix geometries have to be in the ratio of 1:2:3 in order to achieve the same transient linear response. These results and conclusions have also been verified using the other shape factor formulations- Zimmerman and Kazemi.

5.4 Data Analysis Procedure

Results from the previously described sections are combined to develop a preliminary practical method of analyzing field data. The following procedure for determining the fracture spacing is presented.

a) Obtain field production rate data.

b) Check for half slope on log-log plot of rate against time indicating the transient linear flow regime. Also check for a straight line on a plot of $[m(p_i)-m(p_{wf})]/q_g$ against $\sqrt{t}$.

c) Determine $\sqrt{k_m}A_{cm}$ from

$$\sqrt{k_m}A_{cm} = \frac{1262T}{\sqrt{(\phi\mu c_t)_{f+m}}}\frac{1}{\tilde{m}_4} \qquad \text{……(5.1)}$$

d) If matrix permeability is known, determine A_{cm} from $\sqrt{k_m}A_{cm}$

e) If A_c and y_e are known (A_c may be estimated from product of well length and net thickness; y_e is estimated from well spacing);

Assuming one-dimensional slab matrix determine fracture spacing, from $L_1 = \frac{2y_e}{A_{cm}}A_{cw}$ ……(5.2)

Assuming two-dimensional matrix geometry determine fracture spacing from $L_2 = \frac{4y_e}{A_{cm}}A_{cw}$ ……(5.3)

Assuming three-dimensional matrix geometry determine fracture spacing from $L_3 = \frac{6y_e}{A_{cm}}A_{cw}$ ……(5.4)

5.5 Application of Procedure to Synthetic Case

In this section, the field analysis procedure is demonstrated with synthetic data generated using the transient dual porosity model (rectangular geometry, slab matrix blocks) analytical solutions. Data used for this illustration is given in Table 5.4. Calculated parameters are also shown in Table 5.4.

5.5.1 Problem Formulation

Since we know the data in Table 5.4, we can calculate certain values for our synthetic case.

The cross-sectional area is computed from $A_{cw} = 2x_e h = 2(2{,}000)(200) = 8x10^5\ ft^2$

The matrix drainage area is computed from $\frac{A_{cm}}{V_{bm}} = \frac{2}{L}$ (area-volume relation for the slab)

and with $V_{bm} = A_{cw} y_e$; $A_{cm} = \frac{2y_e}{L} A_{cw} = \frac{2(500)}{50}(8x10^5) = 1.6x10^7\ ft^2$

The interporosity flow parameter is computed as

$$\lambda_{Ac} = \frac{12}{L^2}\frac{k_m}{k_f} A_{cw} = \frac{12}{(50)^2}\left(\frac{10^{-5}}{100}\right)(8x10^5) = 3.84 * 10^{-4}$$

The transient dual porosity model is then run with λ_{Ac} = 3.84x10^{-4}, ω=10^{-3} and y_{De}=y_e /$\sqrt{A_{cw}}$ = 0.559. The following equations for dimensionless pressure and time are then used to convert to rate and time values used to plot Fig. 5.6.

$$\frac{1}{q_{DL}} = \frac{k_f \sqrt{A_{cw}}\left[m(p_i) - m(p_{wf})\right]}{1422 q_g T} \quad ; \quad t_{DAc} = \frac{0.00633 k_f t}{(\phi \mu c_t)_{f+m} A_{cw}}$$

Table 5.4 – Synthetic Case Calculation Dataset.	
x_e	2000 ft
y_e	500 ft
h	200 ft
L	50 ft
$\phi_{(m+f)}$	0.15
c_{ti}	304.02×10^{-6} psi^{-1}
k_f	100 md
k_m	10^{-5} md
p_i	3000 psi
p_{wf}	500 psi
T	660 ^{o}R (200^{o}F)
γ_g	0.8
B_{gi}	0.00531 rcf/scf
μ_i	0.0224 cp
Corresponding Values	
y_{De}	0.559
$m(p_i)$	5.902×10^{8} psi^2/cp
$m(p_{wf})$	2×10^{7} psi^2/cp
σ *(slab case)*	0.0012 ft^{-2}
λ_{Ac} *(slab case)*	3.84×10^{-4}
ω	10^{-3}
A_{cm}	1.6×10^{7} ft^2
A_{cw}	8×10^{5} ft^2

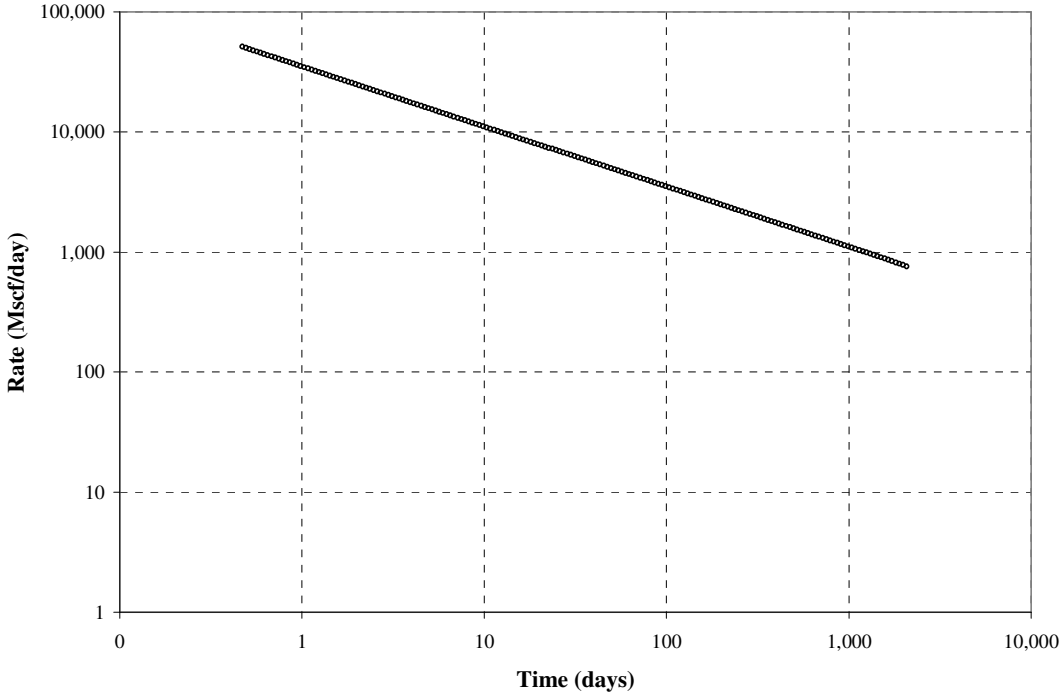

Fig. 5.6 – Log-log Plot of Rate against Time - Synthetic Case. Data was generated using the transient dual porosity model (rectangular geometry, linear flow, slab matrix).

5.5.2 Application

The data indicates a half-slope as shown in Fig. 5.6. The next step is to make a plot of $[m(p_i)-m(p_{wf})]/q_g$ against $\sqrt{t}$ as shown in Fig. 5.7 using the synthetic data generated in Fig. 5.6. As previously stated, it will be assumed that $(\phi\mu c_t)_{f+m}$ (the total system - matrix and fractures) is approximately the same as $(\phi\mu c_t)_m$ for the matrix only. The parameter $(\phi\mu c_t)_m$ is also computed using properties at initial reservoir pressure of the gas equations.

The slope, $\tilde{m}_4$ is determined from Fig. 5.7 as 16,250 psi^2/cp/Mscf/day

And, $\sqrt{k_m}A_{cm} = \dfrac{1262T}{\sqrt{(\phi\mu c_t)_{f+m}}\tilde{m}_4} = \dfrac{1262(660)}{\sqrt{(0.15)(0.0224)(304.02*10^{-6})}(16{,}250)} = 5.07x10^4 md^{0.5} ft^2$

If we can estimate the matrix permeability (k_m=10^{-5} md for this synthetic case) then we can calculate

$$A_{cm} = \frac{5.07x10^4}{\sqrt{10^{-5}}} = 1.6x10^7 ft^2$$

This computed A_{cm} value is the same as the expected value given in Section 5.5.1.

Assuming one-dimensional (slab) matrix geometry;

The fracture spacing is determined from Eq. 5.2 as $L_1 = \dfrac{2y_e}{A_{cm}}A_{cw} = \dfrac{2(500)}{1.6x10^7}(8x10^5) = 50 ft$

This fracture spacing value is similar to the expected value given in Section 5.5.1.

The calculations for our synthetic case were done for our slab matrix block case since this was used to generate the data. If we did not know that this was a slab matrix geometry case and assumed that it was a two-dimensional (column) case, then we can calculate the fracture spacing from Eq. 5.3 as $L_2 = \dfrac{4y_e}{A_{cm}}A_{cw} = \dfrac{4(500)}{1.6x10^7}(8x10^5) = 100 ft$

If we assume that it was a three-dimensional (cube) matrix geometry, then we can similarly calculate the fracture spacing from Eq. 5.4 as

$L_3 = \dfrac{6y_e}{A_{cm}}A_{cw} = \dfrac{6(500)}{(1.6x10^7)}(8x10^5) = 150 ft$

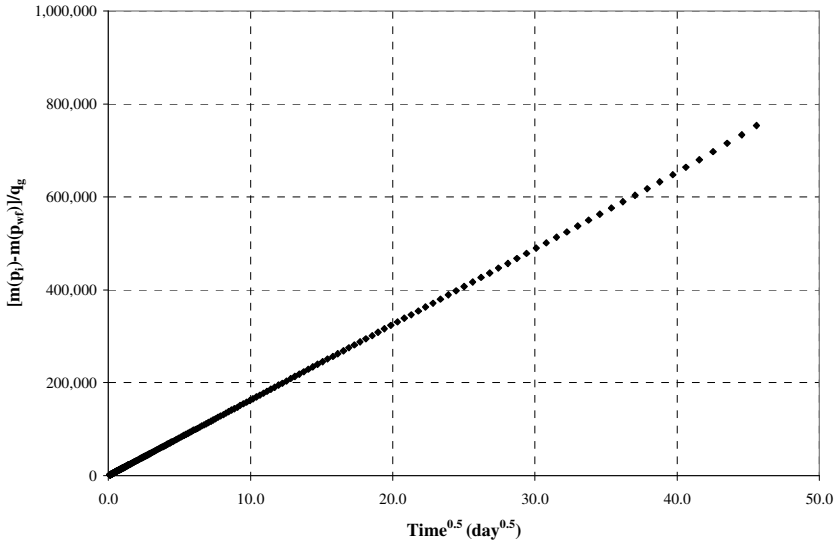

Fig. 5.7 – Specialized Plot of $[m(p_i)-m(p_{wf})]/q_g$ against $t^{0.5}$ - Synthetic Case. Data was generated using the transient dual porosity model (rectangular geometry, linear flow, slab matrix).

It has been shown that the matrix drainage area, A_{cm} and (effective) fracture spacings (L_1, L_2, and L_3) can be calculated using our procedure, if k_m can be estimated. However, there is no way to determine whether the slab, column, or cube case actually applies to a particular well. But it has been shown that the values of (L_1, L_2, and L_3) are in the ratios 1:2:3. In addition to production rate, these calculated values may be useful in determining the effectiveness of the hydraulic fracture treatments. Smaller fracture spacings result in higher gas rates and recovery factors as shown by Mayerhofer *et al.*[14] These calculated values may be used to compare the effectiveness of the fractured systems of different wells. It should be remembered that $(\phi\mu c_t)$ should be calculated at initial pressure for all equations, as is always done for the gas equations.

It should be noted that the skin effect has been assumed to be zero in all that has been presented in this chapter. The effect of skin will be discussed in detail in Chapter VI.

5.6 Summary

The transient linear flow regime (Region 4) was studied in detail. Different shape factor formulations were shown to result in similar Region 4 response when appropriate *f(s)* modifications consistent with λ_{Ac} computations are made. A preliminary procedure for analyzing field data was presented. This was illustrated with a synthetic case. The parameter A_{cm} can be obtained with available limited data.

CHAPTER VI

CONSTANT BOTTOMHOLE PRESSURE EFFECT OF SKIN IN LINEAR GEOMETRY

6.1 Introduction

Skin is normally defined as a dimensionless pressure for the slightly compressible fluid case given for the radial case by[71]

$$s_{rw} = \frac{kh\Delta p_s}{141.2qB\mu} \qquad \text{……..(6.1)}$$

Where the skin is an additional dimensionless pressure

$$p_{wD} = p_D + s_{rw} \qquad \text{……..(6.2)}$$

s_{rw} is the skin for the radial case and p_D is the solution without skin

The Laplace space solution solution for an infinite homogeneous radial reservoir with skin and zero wellbore storage (constant rate inner boundary) is given by

$$\overline{p_{Drw}} = \frac{K_o\left(\sqrt{s}\right) + s_{rw}\sqrt{s}K_1\left(\sqrt{s}\right)}{s\sqrt{s}K_1\left(\sqrt{s}\right)} \qquad \text{……..(6.3)}$$

The corresponding Laplace space solution for the constant p_{wf} inner boundary can be obtained by the Van Everdingen and Hurst[59] relation given by

$$\overline{p_{Drw}} = \frac{1}{s^2\overline{q_{Drw}}} \qquad \text{……..(6.4)}$$

The solution is thus obtained from Eq. 6.4 as

$$\overline{\overline{\frac{1}{q_{Drw}}}} = \frac{s\left[K_o\left(\sqrt{s}\right) + s_{rw}\sqrt{s}K_1\left(\sqrt{s}\right)\right]}{\sqrt{s}K_1\left(\sqrt{s}\right)} \qquad \text{……..(6.5)}$$

The constant rate solution from Eq. 6.3 is inverted from Laplace space and plotted for s_{rw} = 0 and s_{rw} =10 on a semilog plot in Fig. 6.1. It can be observed from Fig. 6.1 that the two responses are parallel and there is a constant offset of 10 from the s_{rw} = 0 case.

The constant p_{wf} solution from Eq. 6.5 is inverted from Laplace space and plotted for s_{rw} = 0 and s_{rw} =10 on a semilog plot in Fig. 6.2. It can be observed from Fig. 6.1 that the two responses are parallel and there is a constant offset of 10 from the s_{rw} = 0 case.

Both the constant rate and constant p_{wf} cases are plotted in Fig. 6.3. It can be observed that the responses are similar for constant rate and constant p_{wf}. It can thus be concluded that the effect of skin on constant rate and constant p_{wf} for the radial reservoir are similar. The constant rate p_{wf} effect has also been confirmed with simulation as shown in Appendix E.

6.2 Effect of Skin in Linear Reservoir

The Laplace space solution for an infinite homogeneous linear reservoir with skin and zero wellbore storage (constant rate inner boundary) is given by[16]

$$\overline{p_{WDLh}} = \frac{2\pi}{s\sqrt{s}}\left[1 + s_{Ach}\sqrt{s}\right] \qquad \text{……(6.6)}$$

where s_{Ach} is the skin and s is the Laplace space variable.

Eq. 6.6 will also govern the response of the closed linear reservoir at early times.

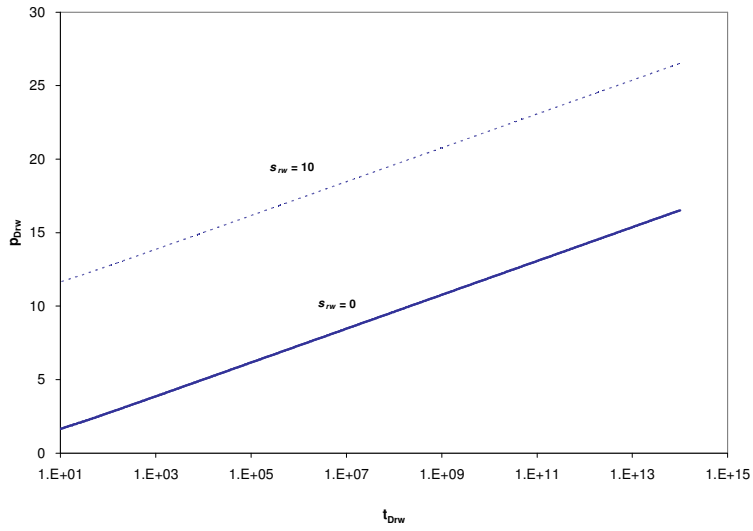

Fig. 6.1– Effect of Skin on Radial Reservoir Model (Constant rate, homogeneous, infinite) for s_{rw} = 0 and 10. Semilog plot. The two responses are parallel and there is a constant offset of 10 from the s_{rw} =0 case.

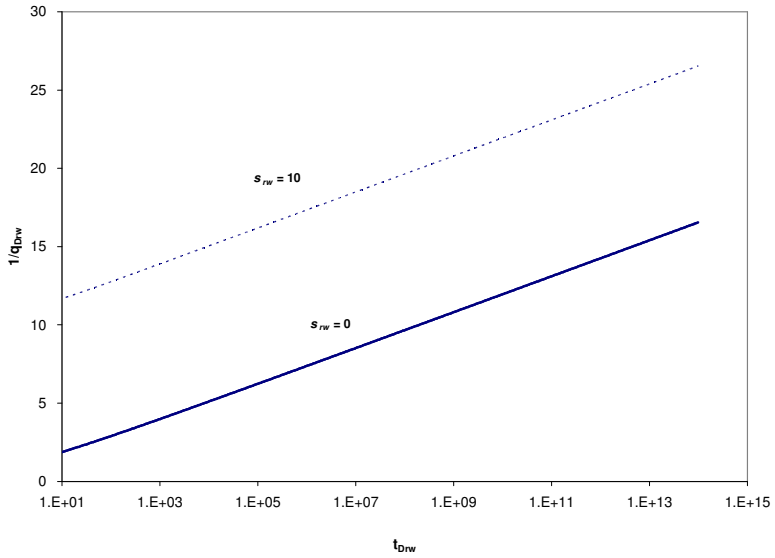

Fig. 6.2 – Effect of Skin on Radial Reservoir Model (Constant p_{wf}, homogeneous, infinite) for s_{rw} = 0 and 10. Semilog plot. The two responses are parallel and there is a constant offset of 10 from the s_{rw} =0 case.

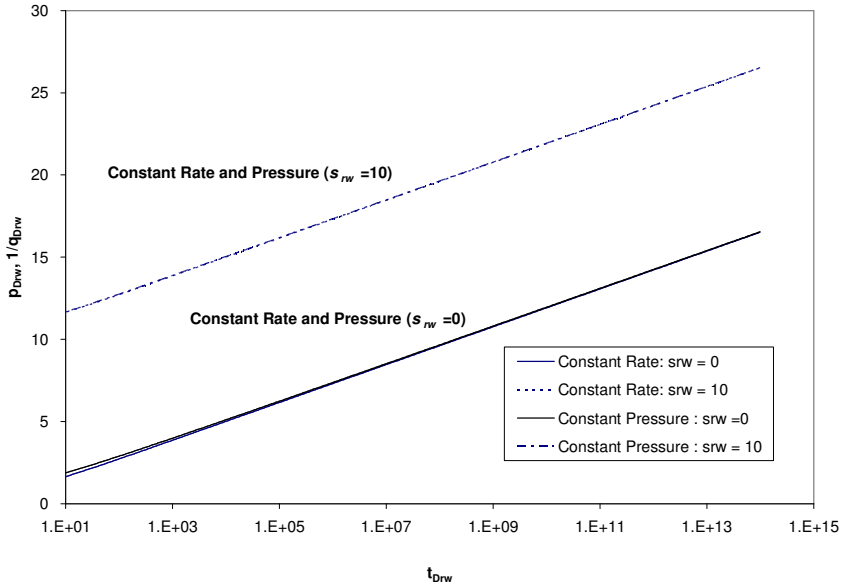

Fig. 6.3 – Effect of Skin on Radial Reservoir Model (Comparing constant rate and p_{wf}, homogeneous, infinite) for s_{rw} = 0 and 10. Semilog plot. It can be observed that the responses are similar for constant rate and pressure.

It can be observed from Eq. 6.6 that

$$\overline{p_{WDLh}} = \frac{2\pi}{s\sqrt{s}} + \frac{2\pi s_{Ach}}{s} \qquad \ldots\ldots\ldots\ldots\ldots\ldots\ldots\ldots\ldots\ldots(6.7)$$

Inverting from Laplace space

$$p_{WDLh} = 2\pi 2\sqrt{\frac{t_{DAch}}{\pi}} + 2\pi s_{Ach} = 4\sqrt{\pi t_{DAch}} + 2\pi s_{Ach} \qquad \ldots\ldots\ldots\ldots\ldots\ldots\ldots\ldots\ldots\ldots(6.8)$$

Where $p_{WDLh} = \dfrac{k\sqrt{A_{cw}}\left[m(p_i) - m(p_{wf})\right]}{1422 q_g T}$; $t_{DAch} = \dfrac{0.00633kt}{(\phi\mu c_t)A_{cw}}$ and k is the homogeneous reservoir permeability.

From Eq. 6.8, the first term on the right hand side is the curve through the origin and the second term is the skin term. This is illustrated in Fig. 6.4 where the s_{Ach} = 10 case is parallel to the s_{Ach} = 0 case with a constant offset of $2\pi s_{Ach}$. The skin effect was defined as $2\pi s_{Ach}$ for the linear model by El-Banbi.[16]

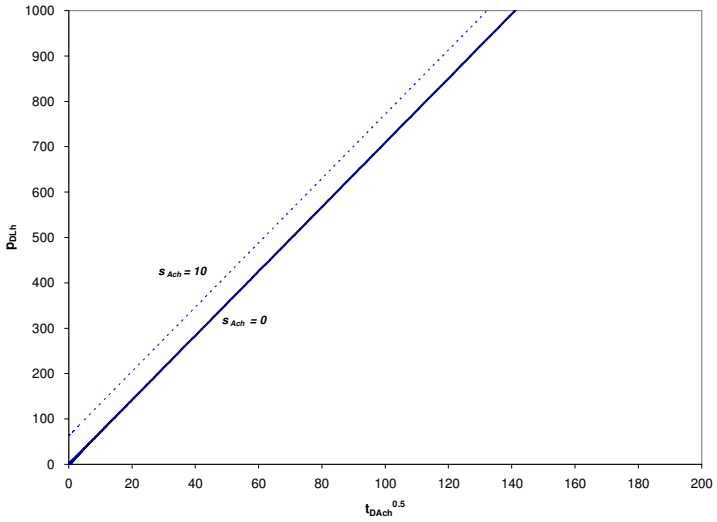

Fig. 6.4 – Effect of Skin on Linear Reservoir Model (Constant rate, homogeneous, infinite) for s_{Ach} = 0 and 10. The two responses are parallel and there is a constant offset of $2\pi(10)$ from the s_{Ach} = 0 case.

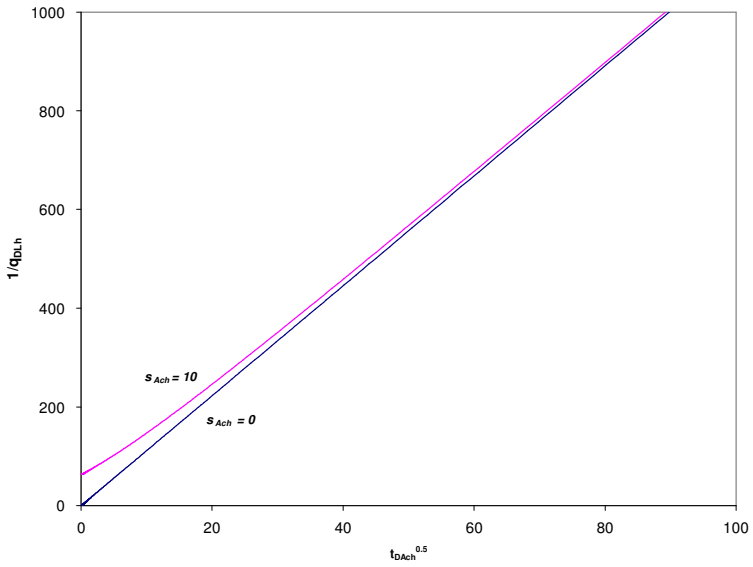

Fig. 6.5 – Effect of Skin on Linear Reservoir Model (Constant p_{wf}, homogeneous, infinite) for s_{Ach} = 0 and 10. The s_{Ach} = 10 case is not parallel to the s_{Ach} = 0 case. The difference between the two curves diminish with time.

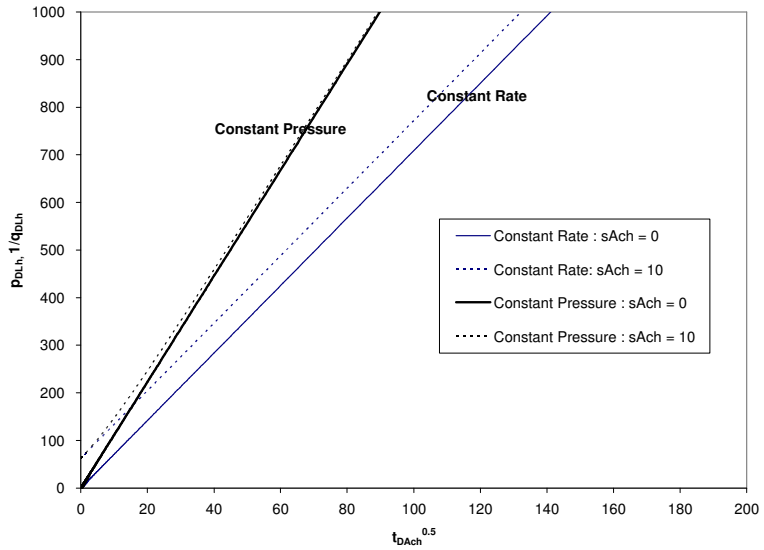

Fig. 6.6 – Effect of Skin on Linear Reservoir Model (Constant p_{wf}, homogeneous, infinite) for s_{Ach} = 0 and 10. The constant rate case is different from the constant pressure case. Note that the constant rate case with s_{rw} = 0 and 10 are parallel whereas the constant p_{wf} case with s_{rw}=10 converges to s_{rw}=0 case at later times.

The Laplace space solution for an infinite homogeneous linear reservoir with skin and zero wellbore storage for the constant pressure inner boundary using Eq. 6.6 is given by

$$\frac{1}{\overline{q_{DLh}}} = \frac{2\pi s}{\sqrt{s}}\left[1 + s_{Ach}\sqrt{s}\right] \qquad \text{…..……(6.9)}$$

where s_{Ach} is the skin (homogeneous case) and s is the Laplace space variable.

Details of the derivation of the skin effect for the constant pressure case are provided in Appendix F.

From Eq. 6.9

$$\overline{q_{DLh}} = \frac{1}{2\pi\sqrt{s}\left[1 + s_{Ach}\sqrt{s}\right]} \qquad \text{……..(6.10)}$$

Solving by partial fractions , Eq. 6.10 can be expressed as

$$\overline{q_{DLh}} = \frac{1}{2\pi\sqrt{s}} + \frac{-s_{Ach}/2\pi}{1 + s_{Ach}\sqrt{s}} \qquad \text{……..(6.11)}$$

Inverting from Laplace space, from Eq. F-10,

$$q_{DLh} = \frac{1}{2\pi s_{Ach}} e^{\left(\frac{t_{DAch}}{s_{Ach}^2}\right)} erfc\left(\frac{\sqrt{t_{DAch}}}{s_{Ach}}\right) \qquad \text{……..(6.12)}$$

Eq. 6.12 gives the transient response for an infinite homogeneous, constant pressure inner boundary reservoir with a skin effect, s_{Ach} present. This is not the same as the constant rate case as illustrated in Figs. 6.5 and 6.6. For the constant pressure case, the skin effect diminishes with time. These results from the linear reservoir case are different from previous observations for the radial case. Eq. 6.12 is confirmed by comparing with the Laplace space inversion of Eq. 6.9 in Fig. 6.7.

It can be observed from Eq. 6.12 that at small times as $t_{DAch} \approx 0$

$$q_{DLh} = \frac{1}{2\pi s_{Ach}} \qquad \text{.....(6.13)}$$

It can also be observed from Eq. 6.12 that at large times as $t_{DAch} \approx \infty$,

Using the first term in the asymptotic expansion for *erfc(x)* for large x

$$erfc(x) = \frac{e^{-x^2}}{x\sqrt{\pi}} \qquad \text{.....(6.14)}$$

Eq. 6.12 becomes

$$q_{DLh} = \frac{1}{2\pi\sqrt{\pi t_{DACh}}} \qquad \text{.....(6.15)}$$

These results explain observations in Fig. 6.6 where the constant pressure response for s_{Ach} =10 ranges from the reciprocal of $1/2\pi s_{Ach}$ at approximately zero time until it approaches the reciprocal of $1/2\pi\sqrt{\pi t_{DAch}}$ at late times.

The following empirical equation has also been found to fit the constant p_{wf} response shown in Fig. 6.5

$$\frac{1}{q_{DLh}} = 2\pi\sqrt{\pi t_{DAch}} + \frac{2\pi s_{Ach}}{1 + \frac{0.8\sqrt{t_{DAch}}}{s_{Ach}}} \qquad \text{.....(6.16)}$$

An expression for the square root of time derivative given by $\frac{d\left(1/q_{DL}\right)}{d\sqrt{t}}$ for identification of the linear region is derived in Appendix G. The derivative is shown for the s_{Ach} = 10 case in Fig. 6.8. This derivative is flat for the linear region.

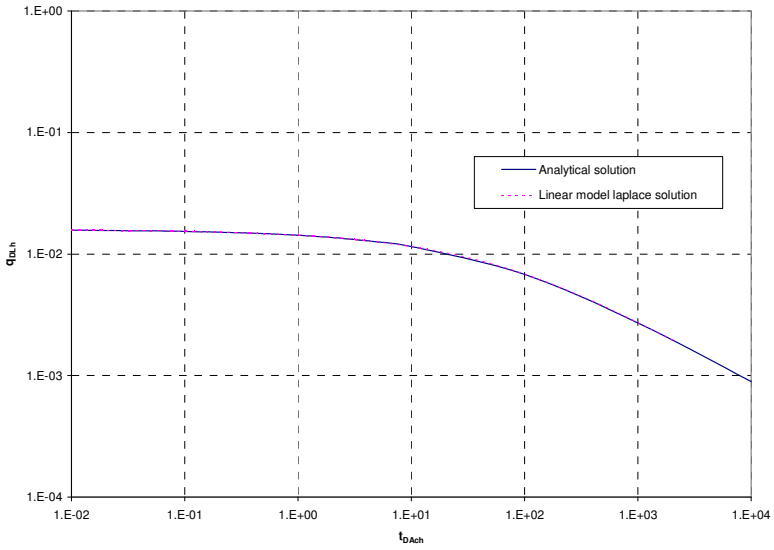

Fig. 6.7 – Validation of Analytical Solution (Linear model, homogeneous, constant p_{wf}) for s_{Ach} =10. The analytical solution is similar to the Laplace space solution.

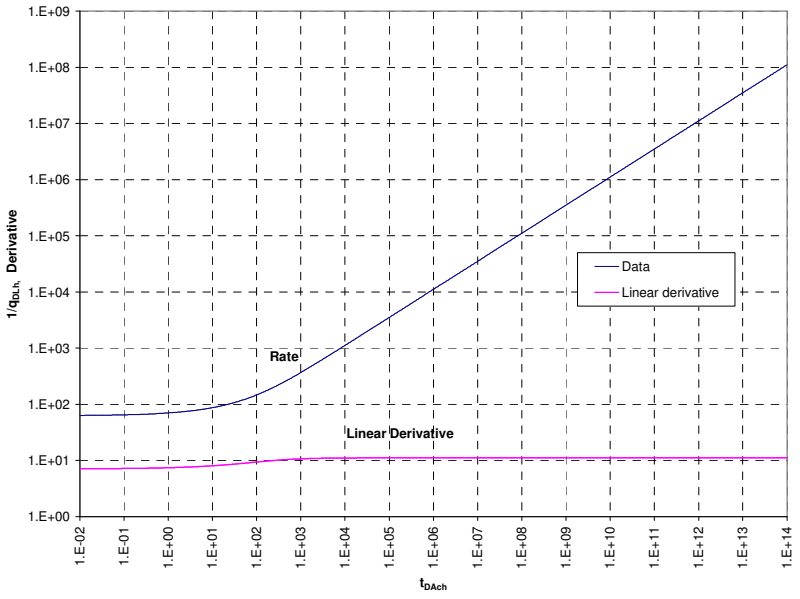

Fig. 6.8 – Rate and Linear Derivative (Linear model, homogeneous, constant p_{wf}) for s_{Ach} =10. The transient linear region is flat on the derivative while the convergence skin region gradually increases.

6.3 Dual Porosity Reservoir

The solutions[16] for the closed linear dual porosity reservoir (slab matrix) for the constant rate and constant pressure inner boundary with a skin, s_{Ac} are given by Eqs. 6.17 and 6.18 respectively.

$$\overline{p_{wDL}} = \frac{2\pi}{s\sqrt{sf(s)}}\left[\frac{\left(1-s_{Ac}\sqrt{sf(s)}\right)\exp\left(-2\sqrt{sf(s)}y_{De}\right)+\left(1+s_{Ac}\sqrt{sf(s)}\right)}{1-\exp\left(-2\sqrt{sf(s)}y_{De}\right)}\right] \qquad \text{.....(6.17)}$$

$$\frac{1}{\overline{q_{DL}}} = \frac{2\pi s}{\sqrt{sf(s)}}\left[\frac{\left(1-s_{Ac}\sqrt{sf(s)}\right)\exp\left(-2\sqrt{sf(s)}y_{De}\right)+\left(1+s_{Ac}\sqrt{sf(s)}\right)}{1-\exp\left(-2\sqrt{sf(s)}y_{De}\right)}\right] \qquad \text{.....(6.18)}$$

with

$$f(s) = \omega + \sqrt{\frac{\lambda_{Ac}}{3s}\frac{(1-\omega)}{\lambda_{Ac}}}\tanh\sqrt{\frac{3(1-\omega)s}{\lambda_{Ac}}} \qquad \text{for the slab matrix case.}$$

These equations are inverted from Laplace space for the constant rate and constant p_{wf} case as shown in Figs. 6.9 and 6.10. The constant rate case in Fig. 6.9 shows similar results to the homogeneous case – there are two parallel lines with an offset of $2\pi s_{Ac}$.

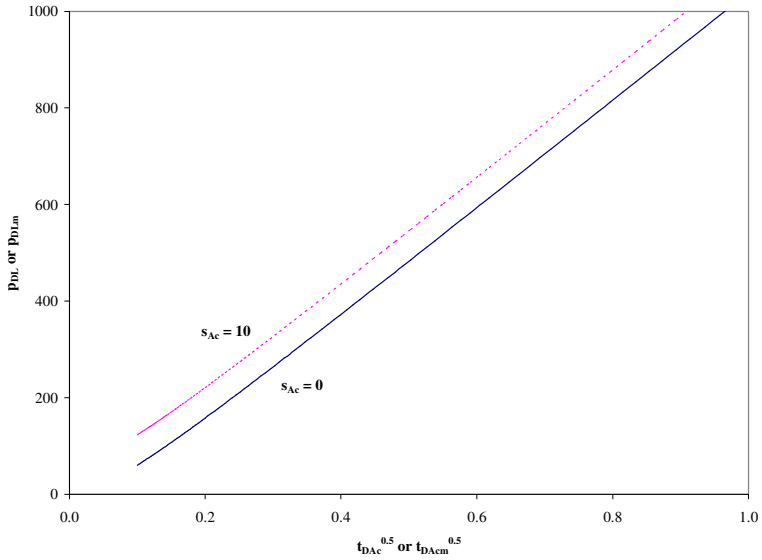

Fig. 6.9 – Effect of Skin on Linear Reservoir Model (Constant rate, Dual porosity, slab matrix, infinite) for s_{Ac} = 0 and 10. Similar to the homogeneous case, the two responses are parallel and there is a constant offset of 2π(10) from the s_{Ac} =0 case.

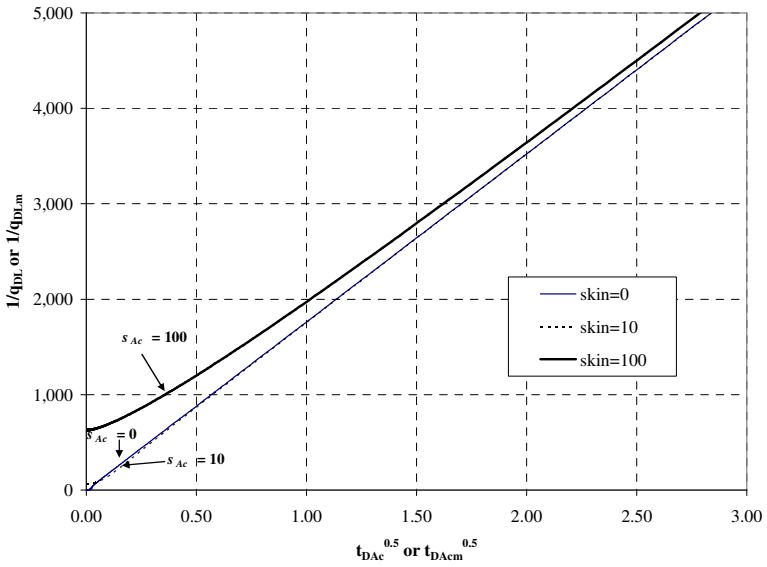

Fig. 6.10 – Effect of Skin on Linear Reservoir Model (Constant p_{wf}, Dual porosity, slab matrix, closed) for s_{Ac} = 0, 10 and 100. For the s_{Ac} =100 case, the skin effect diminishes with time as was observed with the homogeneous case.

For the constant p_{wf} case shown in Fig. 6.10 the skin effect diminishes with time as was observed with the homogeneous case eventually approaching the linear transient response. This is also shown in Fig. 6.11. It can be observed from Fig. 6.11 that as the skin, s_{Ac}, increases, the flatter initial response increases and the linear transient response of the reservoir is delayed.

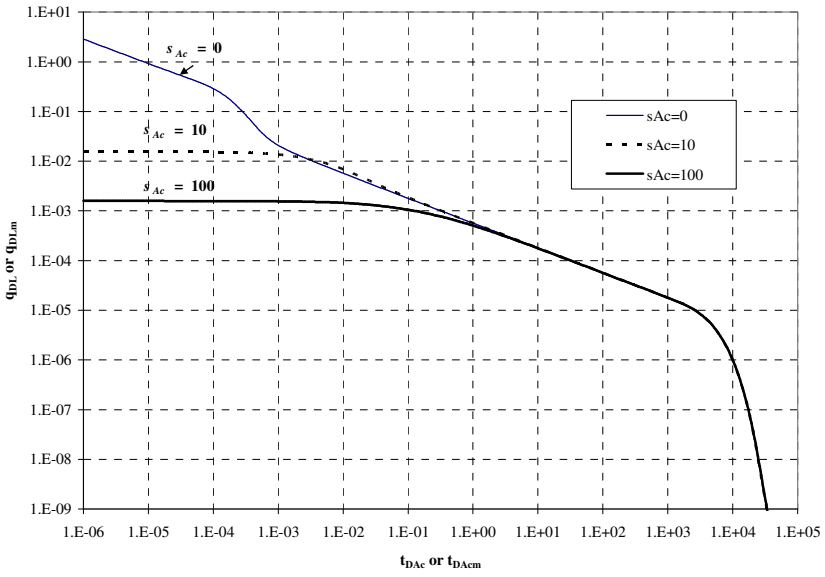

Fig. 6.11 – Log-log plot: Effect of Skin on Linear Reservoir Model (Constant p_{wf}, Dual porosity, slab matrix, closed) for s_{Ac} = 0, 10 and 100 (λ_{Ac} = 3.84* 10^{-4}, ω=10^{-3}, y_{De} = 0.559). As skin increases, the flatter initial response increases and the linear transient response of the reservoir is delayed.

An equation similar to Eq. 6.12 (for the homogeneous case) is derived in Appendix G for the slab matrix dual porosity case. From Eq. G-22,

$$q_{DL} = \frac{1}{2\pi} y_{De} \sqrt{\frac{\lambda_{Ac}}{3}} \frac{3}{A} \left[e^{\left(\frac{3}{A}\right)^2 t_{DAc}} erfc\left(\frac{3}{A} \sqrt{t_{DAc}} \right) \right] \qquad \text{……..……(6.19)}$$

Where $A = \sqrt{\frac{\lambda_{Ac}}{3}} y_{De}^2 + s_{Ac} \sqrt{\frac{\lambda_{Ac}}{3}} 3 y_{De}$

Eq. 6.19 is confirmed by comparison with the inverted Laplace space solution given in Eq. 6.18 as shown in Figs. 6.12 and 6.13 for s_{Ac} = 10 and 100 respectively. It can be observed from Fig. 6.12 that the analytical solution matches the Laplace space solutions at very early and late times. The slight difference noticed on the graph might be as a result of the assumptions made in the derivations of Eq. 6.19.

A better match with the Laplace space solutions is obtained for the s_{Ac} = 100 case in Fig. 6.13. It can thus be concluded that Eq. 6.19 is appropriate for cases with relatively higher skin, s_{Ac}.

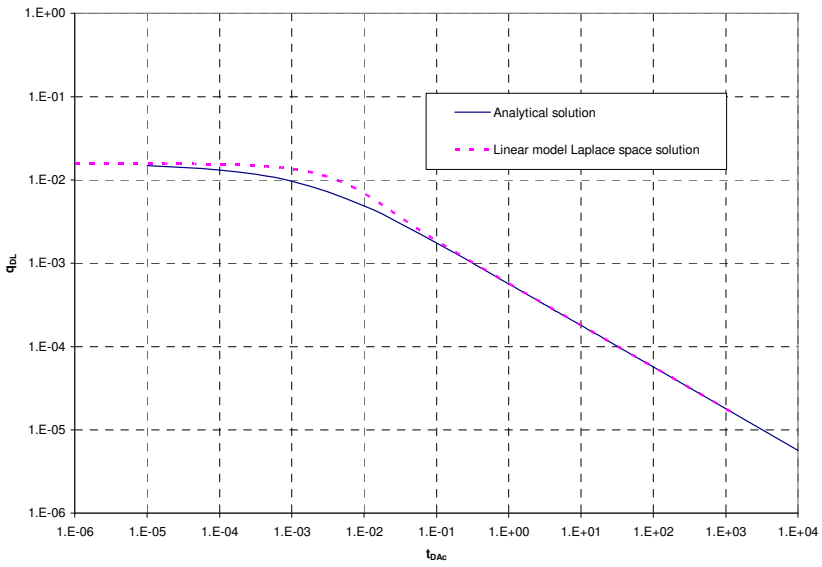

Fig. 6.12 – Validation of Analytical Solution (Linear model, slab matrix, constant p_{wf}, closed) for s_{Ac} =10 (λ_{Ac} = 3.84*10^{-4}, ω=10^{-3}, y_{De} = 0.559). The analytical solution matches the Laplace space solutions at very early and late times.

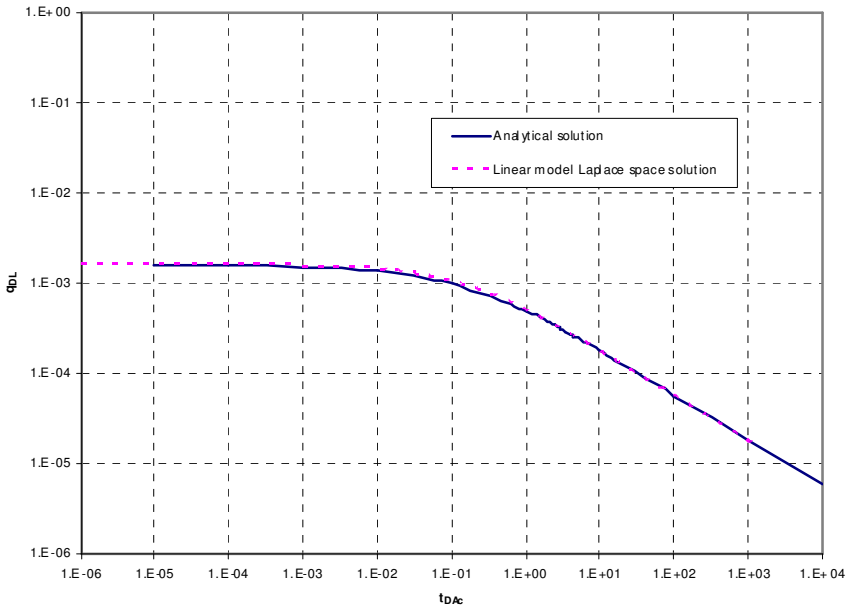

Fig. 6.13 – Validation of Analytical Solution (Linear model, slab matrix, constant p_{wf}, closed) for s_{Ac} =100 (λ_{Ac} = 3.84*10^{-4}, ω =10^{-3}, y_{De} = 0.559). The analytical solution matches more closely with the Laplace space solution compared to the s_{Ac} =10 case in Fig. 6.12.

An empirical equation analogous to that for the homogeneous case previously described in Eq. 6.16 has also been found to fit the constant p_{wf} response for the dual porosity reservoir (slab matrix) shown in Fig. 6.10.

$$\frac{1}{q_{DLm}} = 2\pi\sqrt{\pi t_{DAcm}} + \frac{2\pi s_{Acm}}{1+\frac{0.8\sqrt{t_{DAcm}}}{s_{Acm}}} \qquad \text{……..(6.20)}$$

where $\frac{1}{q_{DLm}} = \frac{k_m\sqrt{A_{cm}}\left[m(p_i)-m(p_{wf})\right]}{1422 q_g T}$; $t_{DAcm} = \frac{0.00633 k_m t}{(\phi\mu c_t)_m A_{cm}}$ and k_m is the reservoir matrix permeability.

6.4 Summary

It has been shown that the effect of skin (constant p_{wf} case) on the transient response is different for radial and linear reservoirs. The effect of skin on the linear reservoir response diminishes gradually with time as demonstrated with $s_{Ac} = 0$ and $s_{Ac} = 10$ cases in Fig. 6.5. The effect of skin for the radial reservoir is the usual constant offset between parallel lines on a semilog plot. A new equation was presented to model the effect of skin on the linear reservoir. The limiting forms of the equations for homogeneous and the dual porosity (slab matrix) are compared in Table 6.1.

Table 6.1 – Comparison of the Limiting Forms of the Transient Linear Response (Constant p_{wf}).

Period	**Homogeneous (Region 3)**	**Dual Porosity (Slab Matrix) (Region 4)**
Zero Time	$q_{DLh} = \frac{1}{2\pi s_{Ach}}$	$q_{DL} = \frac{1}{2\pi s_{Ac}}$ or $q_{DL} = \frac{1}{2\pi}\left(\frac{3}{y_{De} + 3s_{Ac}}\right)$ Or $q_{DLm} = \frac{1}{2\pi s_{Acm}}$
Late Times	$q_{DLh} = \frac{1}{2\pi\sqrt{\pi t_{DACh}}}$	$q_{DL} = \frac{1}{2\pi\sqrt{\pi t_{DAC}}}\sqrt{\frac{\lambda_{Ac}}{3}}y_{De}$ Or $q_{DLm} = \frac{1}{2\pi\sqrt{\pi t_{DACm}}}$

CHAPTER VII

APPLICATION TO SAMPLE FIELD DATA CASES

7.1 Introduction

It is necessary to predict field data with a skin effect behavior. A synthetic case is developed to represent field behavior using data given in Table 7.1. The linear model (slab matrix, constant p_{wf}, closed, linear) is used to generate the transient response in dimensionless variables, q_{DL} and t_{DAc}. The generated results are then converted to rate and time using Eq. 7.1.

$$\frac{1}{q_{DL}} = \frac{k_f \sqrt{A_{cw}}\left[m(p_i) - m(p_{wf})\right]}{1422 q_g T} \qquad t_{DAc} = \frac{0.00633 k_f t}{(\phi \mu c_t)_{f+m} A_{cw}} \qquad \text{……..……(7.1)}$$

The results are then plotted as Figs. 7.1 and 7.2 for the $s_{A\,c} = 0$ and $s_{Ac} = 10$ cases.

The dimensionless time for the end of the convergence skin period is computed as 8.06 x 10^{-4} using Eq. 7.2 (previously shown as Eq. 3.8). This is equivalent to a time of 0.74 days.

$$t_{DAc} = \frac{h}{2\pi^3 L_w} \qquad \text{……..……(7.2)}$$

The results in Figs. 7.1 and 7.2 indicate that the half-slope transient linear period (Region 4) dominates the response. Actual field data is thus expected to lie in Region 4.

Table 7.1 – Synthetic Case Dataset.	
L_w	2,000 ft
y_e	250 ft
h	100 ft
r_w	0.3 ft
$\phi_{(m+f)}$	0.08
c_{ti}	1.185×10^{-4} psi^{-1}
k_f	0.015 md
k_m	2.5×10^{-9} md
p_i	4300 psi
p_{wf}	500 psi
T	600 ^{o}R (140^{o}F)
γ_g	0.57
B_{gi}	0.6702 RB/Mscf
μ_i	0.02308 cp
Corresponding Values	
y_{De}	0.395
$m(p_i)$	1.1×10^{9} psi^2/cp
$m(p_{wf})$	1.99×10^{7} psi^2/cp
λ_{Ac} *(slab case)*	3.20×10^{-4}
ω	10^{-3}
A_{cw}	4×10^{5} ft^2

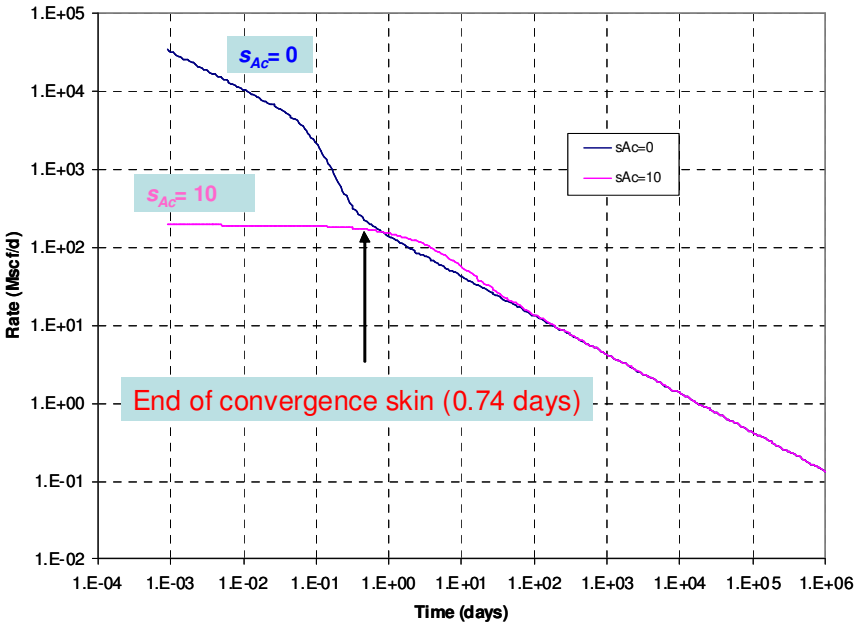

Fig. 7.1 – Log-log Plot of Rate against Time (Synthetic Case :s_{Ac} = 0 and 10). Arrow indicates that the convergence skin stabilizes after 0.74 days. Response is expected to be primarily in Region 4.

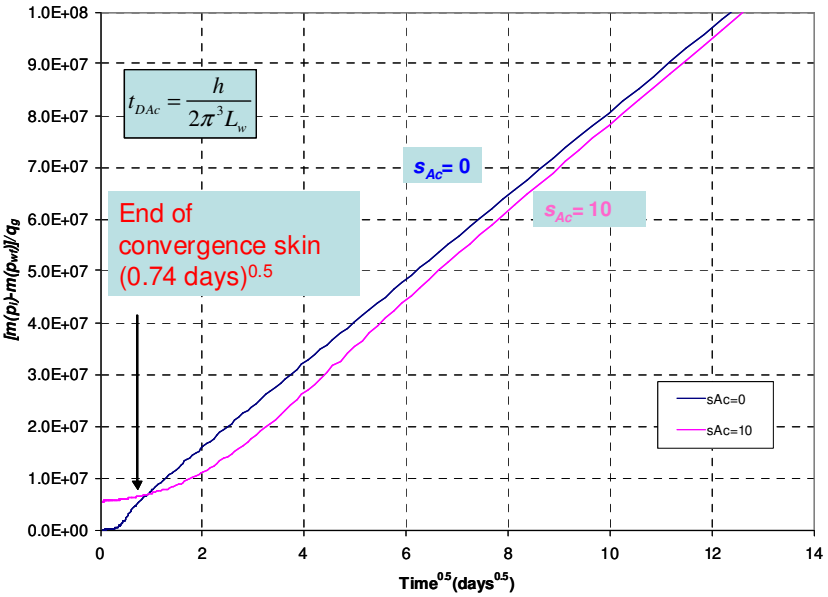

Fig. 7.2 – Specialized Plot of $[m(p_i)-m(p_{wf})]/q_g$ against $t^{0.5}$ (Synthetic Case :s_{Ac} = 0 and 10). Arrow indicates that the convergence skin stabilizes after 0.74 days. Response is expected to be primarily in Region 4.

A preliminary procedure was presented in Chapter V for data analysis. This was for the zero skin case. The only parameter that could be determined from the *[m(pi)-m(pwf)]/q_g* vs $t^{0.5}$ plot was essentially the matrix drainage area, A_{cm}. But the techniques previously presented also apply to the case where the data points are on a straight line through the origin on the *[m(pi)-m(pwf)]/q_g* vs $t^{0.5}$ plot. It is necessary to develop techniques for the case where the data points indicate an "intercept" on the *[m(pi)-m(pwf)]/q_g* vs $t^{0.5}$ plot as expected with the presence of skin (this was demonstrated on a dimensionless plot basis in Chapter VI). In this chapter, a procedure incorporating the effect of skin will be described and the procedures will be applied to two sample field cases (Wells A and B).

7.2 Effect of Skin Plots

Fig. 7.3 shows a series of curves generated from the linear dual porosity model (slab matrix ($\lambda_{Ac} = 10^{-4}$, $\omega = 10^{-3}$, $s_{Ac} = 0, 1, 10, 100$; $y_{De} = 0.5, 1$). This also shown as a square root time plot in Fig. 7.4. It can be observed from Fig. 7.3 that the curves for a particular y_{De} indicate the expected initial flat portion and converge to the transient linear regime.

The plot in Fig. 7.5 clearly indicates that the Region 3 (homogeneous) equation cannot be applied for transient linear analysis since there is no half slope evident in the presence of skin.

The initial q_{DL} value of the curves in Fig. 7.3 at time zero obeys Eq. 6.12

$$q_{DL} = \frac{1}{2\pi s_{Ac}} \qquad \text{.....(7.3)}$$

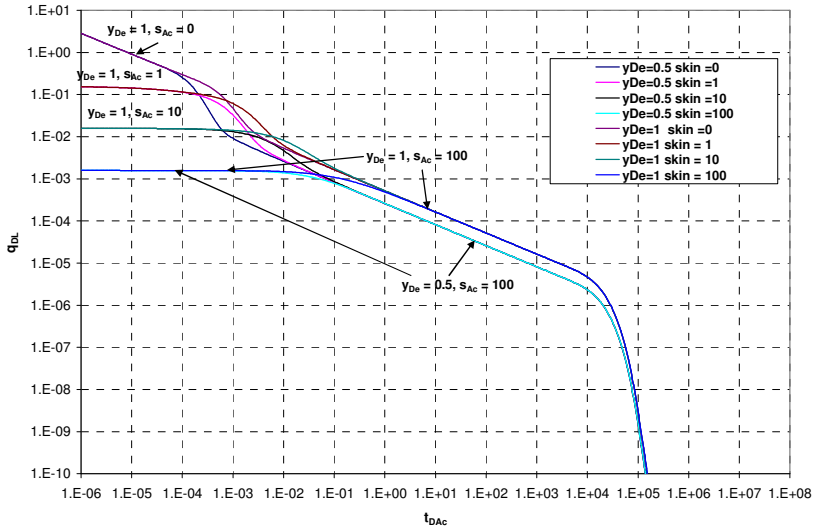

Fig. 7.3 – Log-log Plot of q_{DL} against t_{DAc} for the Linear Dual Porosity Reservoir, Slab Matrix Case ($\lambda_{Ac} = 10^{-4}$, $\omega = 10^{-3}$, s_{Ac} = 0, 1, 10, 100; y_{De} = 0.5, 1). The curves converge to the same initial point for a fixed s_{Ac}. The curves also converge to the same Region 4 half-slope line for a fixed y_{De}.

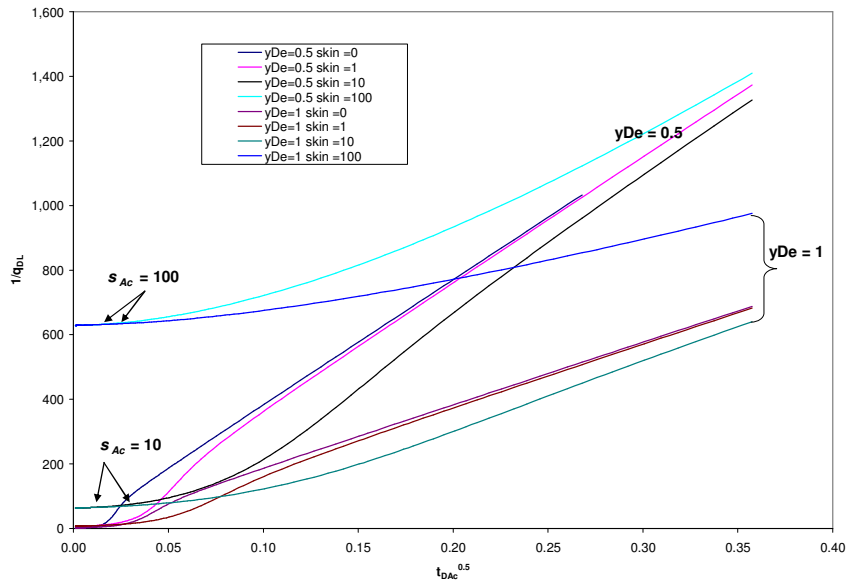

Fig. 7.4 – Specialized Plot of $1/q_{DL}$ against $t_{DAc}^{0.5}$ for the Linear Dual Porosity Reservoir, Slab Matrix Case ($\lambda_{Ac} = 10^{-4}$, $\omega = 10^{-3}$, s_{Ac} =0, 1, 10, 100; y_{De} = 0.5, 1). The curves converge to the same initial point for a fixed s_{Ac} and asymptotically approach the s_{Ac} = 0 line at late times.

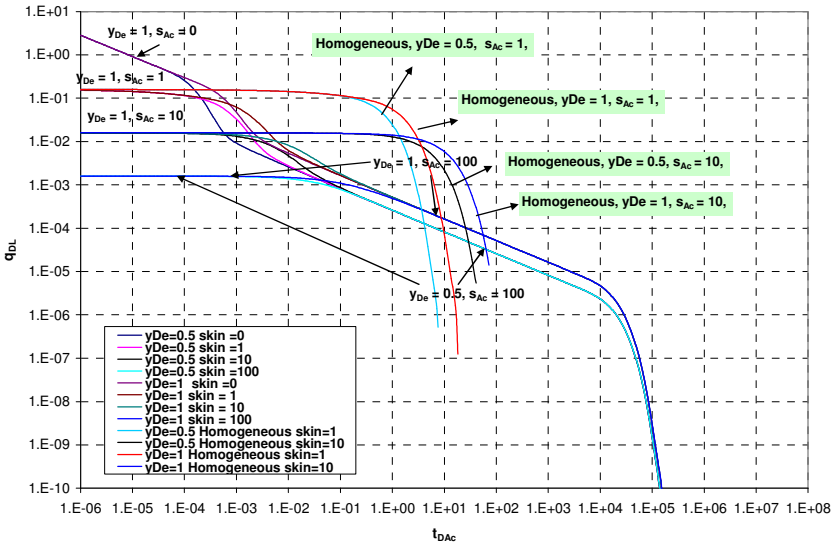

Fig. 7.5 – Log-log Plot of q_{DL} against t_{DAc} for the Linear Dual Porosity Reservoir, Slab Matrix Case (λ_{Ac} = 10^{-4}, ω=10^{-3}, s_{Ac} = 1, 10, 100; y_{De} = 0.5, 1) – Fig. 7.3 - with Homogeneous Case. This plot clearly indicates that the Region 3 (homogeneous) cannot be applied to the transient linear analysis – there is no half slope evident in the presence of skin.

The following empirical equation for the effect of skin on the dual porosity transient response (Region 4) was previously presented as Eq. 6.20

$$\frac{1}{q_{DLm}} = 2\pi\sqrt{\pi t_{DAcm}} + \frac{2\pi s_{Acm}}{1+\dfrac{0.8\sqrt{t_{DAcm}}}{s_{Acm}}} \qquad \text{.....(7.4)}$$

where $\dfrac{1}{q_{DLm}} = \dfrac{k_m\sqrt{A_{cm}}\left[m(p_i)-m(p_{wf})\right]}{1422 q_g T}$; $t_{DAcm} = \dfrac{0.00633 k_m t}{(\phi\mu c_t)_m A_{cm}}$ and k_m is the reservoir matrix permeability.

Eq. 7.4 can be expressed as

$$\frac{k_m\sqrt{A_{cm}}\left[m(p_i)-m(p_{wf})\right]}{1422q_gT}=2\pi\sqrt{\pi\frac{0.00633k_mt}{(\phi\mu c_t)_mA_{cm}}}+\frac{2\pi s_{Acm}}{1+\dfrac{0.8\sqrt{\dfrac{0.00633k_mt}{(\phi\mu c_t)_mA_{cm}}}}{s_{Acm}}} \qquad \text{.....(7.5)}$$

where $\left(\dfrac{\left[m(p_i)-m(p_{wf})\right]}{q_g}\right)_0$ is the intercept obtained from a plot of $\dfrac{m(p_i)-m(p_{wf})}{q_g}vs\sqrt{t}$

with $2\pi s_{Ac}=\dfrac{k_m\sqrt{A_{cm}}}{1422T}\left(\dfrac{\left[m(p_i)-m(p_{wf})\right]}{q_g}\right)_0$, Eq. 7.5 becomes

$$\frac{k_m\sqrt{A_{cm}}\left[m(p_i)-m(p_{wf})\right]}{1422q_gT}=2\pi\sqrt{\pi\frac{0.00633k_mt}{(\phi\mu c_t)_mA_{cm}}}+\frac{\dfrac{k_m\sqrt{A_{cm}}}{1422T}\left(\dfrac{\left[m(p_i)-m(p_{wf})\right]}{q_g}\right)_0}{1+\dfrac{0.8\sqrt{\dfrac{0.00633k_mt}{(\phi\mu c_t)_mA_{cm}}}}{\dfrac{1}{2\pi}\dfrac{k_m\sqrt{A_{cm}}}{1422T}\left(\dfrac{\left[m(p_i)-m(p_{wf})\right]}{q_g}\right)_0}} \qquad \text{.....(7.6)}$$

where $\left(\dfrac{\left[m(p_i)-m(p_{wf})\right]}{q_g}\right)_0$ is the intercept obtained from a plot of $\dfrac{m(p_i)-m(p_{wf})}{q_g}vs\sqrt{t}$

$$\frac{k_m\sqrt{A_{cm}}\left[m(p_i)-m(p_{wf})\right]}{1422q_gT}=2\pi\sqrt{\pi\frac{0.00633k_mt}{(\phi\mu c_t)_mA_{cm}}}+\frac{\dfrac{k_m\sqrt{A_{cm}}}{1422T}\left(\dfrac{\left[m(p_i)-m(p_{wf})\right]}{q_g}\right)_0}{1+\dfrac{0.8\sqrt{\dfrac{0.00633k_mt}{(\phi\mu c_t)_mA_{cm}}}}{\left(\dfrac{\left[m(p_i)-m(p_{wf})\right]}{q_g}\right)_0}\dfrac{2\pi(1422T)}{k_m\sqrt{A_{cm}}}} \qquad \text{.....(7.7)}$$

$$\frac{k_m\sqrt{A_{cm}}\left[m(p_i)-m(p_{wf})\right]}{1422q_gT}=2\pi\sqrt{\pi\frac{0.00633k_mt}{(\phi\mu c_t)_mA_{cm}}}+\frac{\dfrac{k_m\sqrt{A_{cm}}}{1422T}\left(\dfrac{\left[m(p_i)-m(p_{wf})\right]}{q_g}\right)_0}{\dfrac{\left(\dfrac{\left[m(p_i)-m(p_{wf})\right]}{q_g}\right)_0\sqrt{(\phi\mu c_t)_m}\sqrt{k_m}A_{cm}+0.8\sqrt{(0.00633)}2\pi(1422T)\sqrt{t}}{\left(\dfrac{\left[m(p_i)-m(p_{wf})\right]}{q_g}\right)_0\sqrt{(\phi\mu c_t)_m}\sqrt{k_m}A_{cm}}} \qquad \text{.....(7.8)}$$

$$\frac{k_m\sqrt{A_{cm}}\left[m(p_i)-m(p_{wf})\right]}{1422q_gT}=2\pi\sqrt{\pi\frac{0.00633k_mt}{(\phi\mu c_t)_mA_{cm}}}+\frac{\frac{k_m\sqrt{A_{cm}}}{1422T}\left(\frac{\left[m(p_i)-m(p_{wf})\right]}{q_g}\right)_0\left(\frac{\left[m(p_i)-m(p_{wf})\right]}{q_g}\right)_0\sqrt{(\phi\mu c_t)_m}\sqrt{k_m}A_{cm}}{\left(\frac{\left[m(p_i)-m(p_{wf})\right]}{q_g}\right)_0\sqrt{(\phi\mu c_t)_m}\sqrt{k_m}A_{cm}+0.8\sqrt{(0.00633)}2\pi(1422T)\sqrt{t}}$$

……..(7.9)

Multiplying Eq. 7.9 by $\frac{1422T}{k_m\sqrt{A_{cm}}}$

$$\frac{\left[m(p_i)-m(p_{wf})\right]}{q_g}=\frac{1262T\sqrt{t}}{\sqrt{k_m}A_{cm}\sqrt{(\phi\mu c_t)_m}}+\frac{\left(\frac{\left[m(p_i)-m(p_{wf})\right]}{q_g}\right)_0^2\sqrt{(\phi\mu c_t)_m}\sqrt{k_m}A_{cm}}{\left(\frac{\left[m(p_i)-m(p_{wf})\right]}{q_g}\right)_0\sqrt{(\phi\mu c_t)_m}\sqrt{k_m}A_{cm}+569T\sqrt{t}}$$

……..(7.10)

The expression given by Eq. 7.10 represents an equation that can be used to fit data on a plot of $\frac{m(p_i)-m(p_{wf})}{q_g}vs\sqrt{t}$. The term $\sqrt{k_m}A_{cm}$ can be determined from the equation previously presented for Region 4 in Chapter IV.

$$\sqrt{k_m}A_{cm}=\frac{1262T}{\sqrt{(\phi\mu c_t)_{f+m}}}\frac{1}{\tilde{m}_4}$$ ……..(7.11)

$\tilde{m}_4$ is the slope of a line drawn through the origin passing through the linear half-slope data points.

Eq. 7.10 can be reproduced on a log-log plot using Eq. 7.12.

$$q_g=\left[m(p_i)-m(p_{wf})\right]\Bigg/\left(\frac{1262T\sqrt{t}}{\sqrt{k_m}A_{cm}\sqrt{(\phi\mu c_t)_m}}+\frac{\left(\frac{\left[m(p_i)-m(p_{wf})\right]}{q_g}\right)_0^2\sqrt{(\phi\mu c_t)_m}\sqrt{k_m}A_{cm}}{\left(\frac{\left[m(p_i)-m(p_{wf})\right]}{q_g}\right)_0\sqrt{(\phi\mu c_t)_m}\sqrt{k_m}A_{cm}+569T\sqrt{t}}\right)$$

……..(7.12)

The procedure previously given in Chapter V can be summarized and modified thus:

a) Obtain field production rate data.

b) Check for half slope on log-log plot of rate against time indicating the transient linear flow regime. Also check for a straight line on a plot of $[m(p_i)-m(p_{wf})]/q_g$ against $t^{0.5}$.

c) Draw a line through the origin passing through the linear half-slope data points. Determine the slope of this line and use as $\tilde{m}_4$ in Eq. 7.11 to determine $\sqrt{k_m}A_{cm}$.

d) If matrix permeability, k_m is known then calculate matrix drainage area A_{cm} from $\sqrt{k_m}A_{cm}$

e) Use $\sqrt{k_m}A_{cm}$ and the intercept $\left(\frac{[m(p_i)-m(p_{wf})]}{q_g}\right)_0$ in Eq. 7.10 to fit the given field data

f) Reproduce the equivalent to the fit from step e) on the log-log plot using Eq. 7.12.

7.3 Application of Procedure to Field Data

In this section, the methods previously presented will be applied to actual field cases. Two examples are presented (Wells A and B). The gas rate and flowing tubing pressure data are shown for Wells A and B in Figs. 7.6 and 7.7 respectively. The reservoir and fluid properties data are shown in Table 7.2. Other computed parameters are given in Table 7.3. The length of the wells are shown in Table 7.4 A log-log plot of the rate

against time and specialized plot of $[m(p_i)-m(p_{wf})]/q_g$ against $t^{0.5}$ is shown for Well A in Figs. 7.8 and 7.9. These plots are shown for Well B in Figs. 7.10 and 7.11. These plots indicate the transient linear flow (half-slope on log-log plot). The log-log plot also indicates the constant p_{wf} effect of skin previously described. An initial curve corresponding to the convergence skin effect is noticed at early times. The transient linear is noticed at later times.

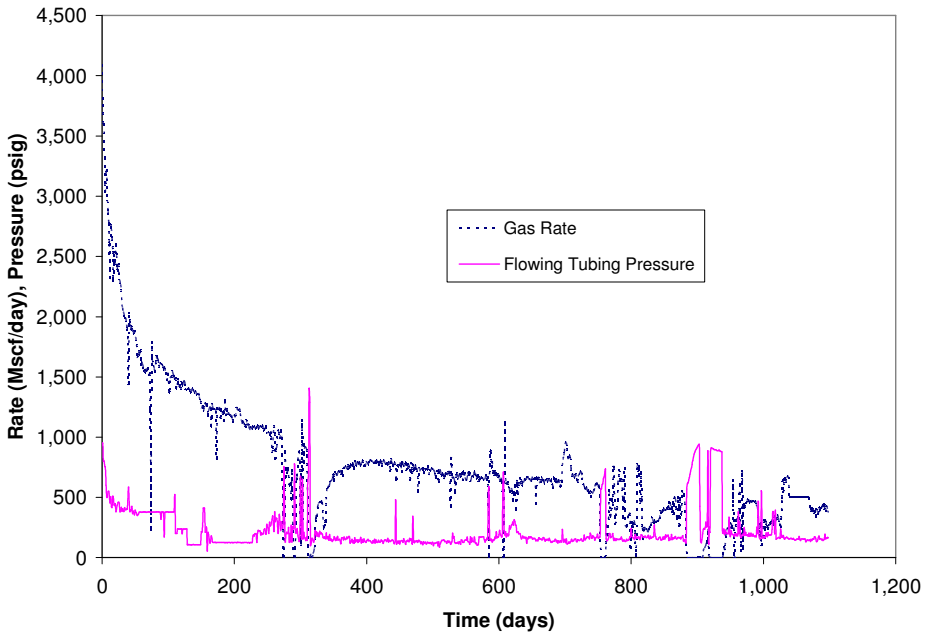

Fig. 7.6 – Field Rate and Pressure Data for Well A.

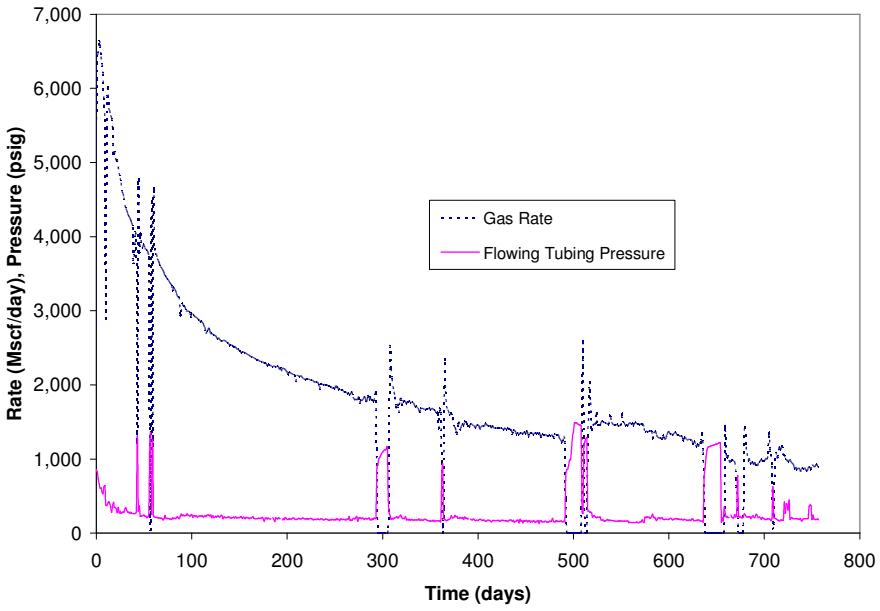

Fig. 7.7 – Field Rate and Pressure Data for Well B.

Table 7.2 - Reservoir and Fluid Properties Data for Wells A and B Analysis.	
h	140 ft
k_m	1.5×10^{-4} md
p_i	3000 psi
ϕ	0.034
T	175^{o}F (635^{o}R)
γ_g	0.65

Table 7.3 - Other Fluid Data for Wells A and B Analysis.	
$m(p_i)$	5.98×10^8 psi^2/cp
B_{gi}	0.00535 rcf/scf
c_{gi}	3.03×10^{-4} psi^{-1}
μ_i	0.0199 cp

Table 7.4 Completion Parameters of Horizontal Wells A and B.		
	x_e	$A_{cw} (=2x_eh)$
A	3417 ft	$9.57*10^5$ ft^2
B	3000 ft	$8.4*10^5$ ft^2

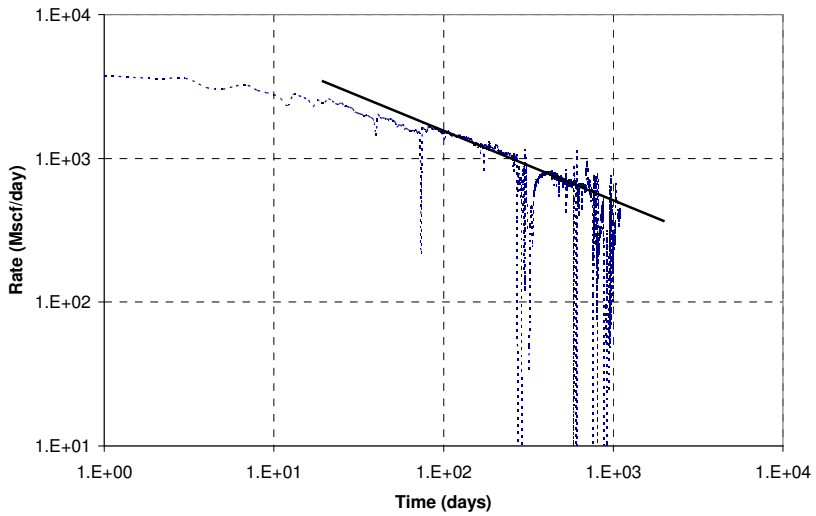

Fig. 7.8 – Log-log Plot of Rate against Time with Data Fit for Well A. Line drawn on plot indicates half slope.

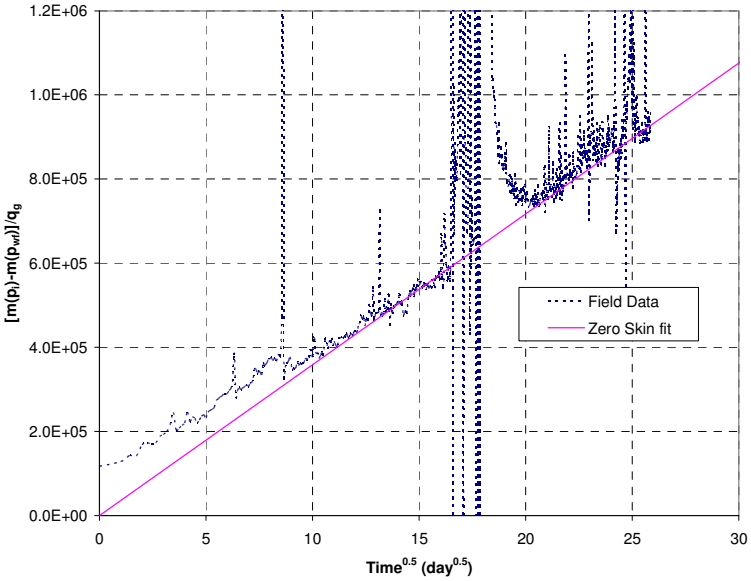

Fig. 7.9 – Specialized Plot of $[m(p_i)-m(p_{wf})]/q_g$ against $t^{0.5}$ with Zero Skin Fit for Well A. Line shown is drawn through origin and fitted to data. Data appear to indicate an initial curve corresponding to the convergence skin effect and linear transient at later times. This appears to match theory discussed in Chapter VI.

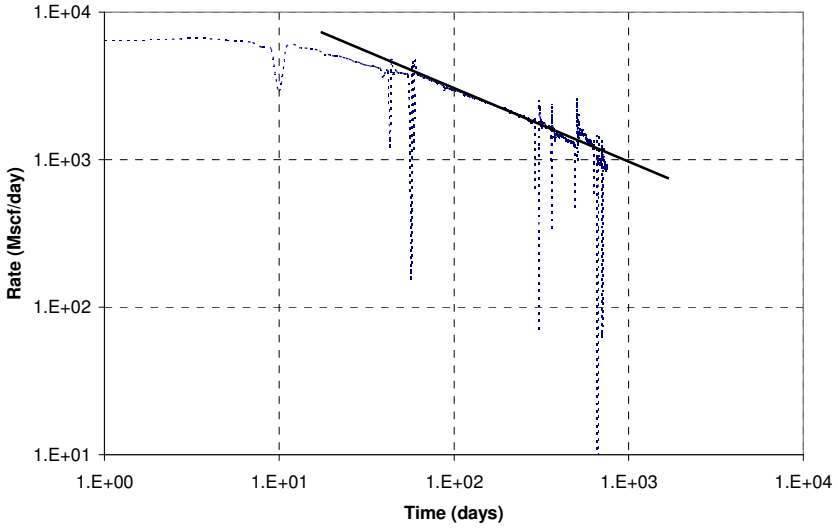

Fig. 7.10 – Log-log Plot of Rate against Time with Data Fit for Well B. Line drawn on plot indicates half slope.

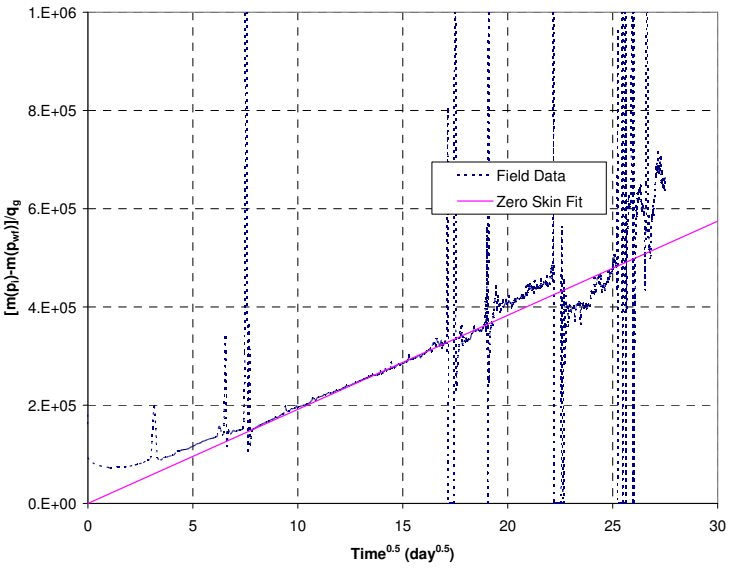

Fig. 7.11 – Specialized Plot of $[m(p_i)-m(p_{wf})]/q_g$ against $t^{0.5}$ with Zero Skin Fit for Well B Line shown is drawn through origin and fitted to data. Data appear to indicate an initial curve corresponding to the convergence skin effect and linear transient at later times. This appears to match theory discussed in Chapter VI.

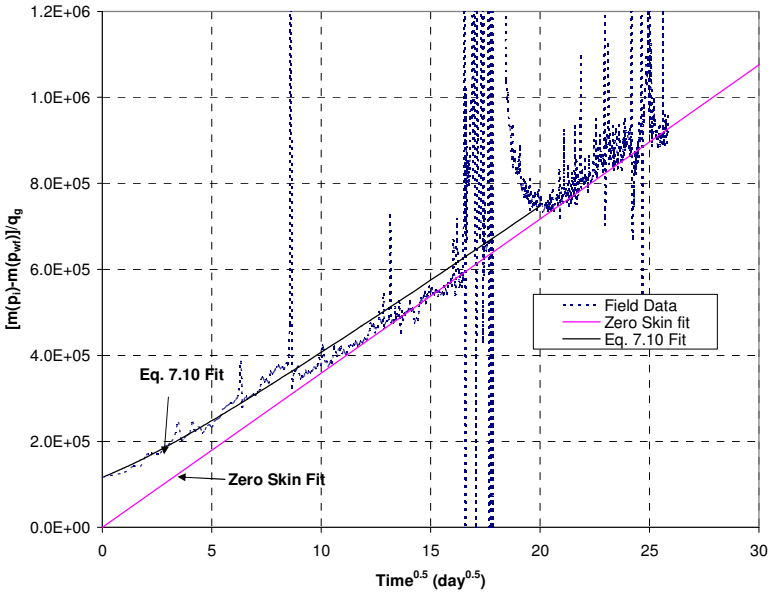

Fig. 7.12 – Specialized Plot of $[m(p_i)-m(p_{wf})]/q_g$ against $t^{0.5}$ with Eq. 7.10 Fit for Well A. Line shown is drawn through origin and fitted to data. Eq. 7.10 is also fitted to data as shown. A better fit can be obtained by choosing a lower intercept.

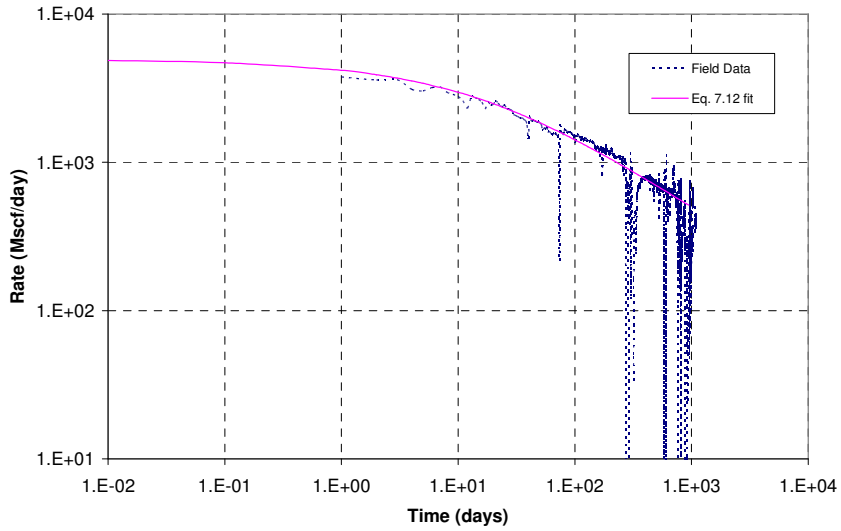

Fig. 7.13 – Log-log Plot Representation of Fig.7.12 Fit for Well A. Eq. 7.12 is also fitted to data as shown.

7.4 Discussion

A sample calculation for the matrix drainage area, A_{cm} using the techniques described in Chapter V is described for Well A. The slope is determined from Fig. 7.9 and 7.12 as 35,874 respectively. It should be noted that the slope computed is that of a line drawn through the origin as shown in Fig. 7.9 and 7.12. The intercept on the y-axis is determined approximately as 116,875.

Eq. 7.10 is fitted to that data and shown in Fig 7.12. The plot from Fig. 7.12 is reproduced on a log-log plot using Eq. 7.12 and shown in Fig. 7.13.

The parameter $\sqrt{k_m}A_{cm}$ can be calculated using Eq. 7.11.

$$\sqrt{k_m}A_{cm} = \frac{1262T}{\sqrt{(\phi\mu c_t)_{f+m}}\tilde{m}_4} = \frac{1262(635)}{\sqrt{(0.034)(0.0199)(3.03*10^{-4})}(36{,}040)} = 4.93x10^4\, md^{0.5}\, ft^2$$

And $$A_{cm} = \frac{1}{\sqrt{k_m}} = \frac{1}{\sqrt{1.5x10^{-4}}} = 4.03x10^6\, ft^2$$

A_{cm} is computed similarly for Well B as $7.54\text{x}10^6$ ft^2. Well B has a larger A_{cm} value than Well A. This indicates that Well B has a larger matrix area contacted by the frac job.

Other information is required to determine the fracture spacing from A_{cm} as demonstrated in Chapter V. Computed spacing for the slab matrix case can then be used to determine the corresponding values for other column and cube matrix geometries as described in Chapter V. The fracture spacings will be in the ratios 1:2:3 for the same matrix drainage area, A_{cm}.

In conclusion, a procedure has been presented for analyzing field data in which transient linear flow has been observed. This procedure is dependent on the linear model presented in this paper with its underlying assumptions and ability to reasonably

determine fluid and reservoir properties. The well has also been assumed to be located in the center of the reservoir.

It is concluded that field data obtain exhibit Region 4 only (drainage primarily from the matrix). The only parameter than can be determined from available data is $\sqrt{k_m} A_{cm}$.

The effects of adsorption have been neglected for reasons mentioned in Chapter I. As pressures approach 1000 psia in the Barnett shale, these effects will become more prominent.

The effect of water production has also been neglected. These are areas of further research.

CHAPTER VIII

CONCLUSIONS AND RECOMMENDATIONS

8.1 Conclusions

The major conclusions of this work can be summarized as follows:

1. A linear dual porosity model can be utilized to represent multi-fractured horizontal wells in shale gas reservoirs.
2. It has been shown extensively that matrix drainage of any geometry at constant pressure boundary conditions results in transient linear flow.
3. Five flow regions were identified using this linear model. Region 1 is the early transient linear response in the fracture system. Region 2 is the bilinear flow regime and occurs when there is a transient linear in the fracture and matrix simultaneously. Region 3 is the response for a homogeneous reservoir case. Region 4 is primarily drainage of the matrix (our regime of interest). Region 5 occurs when all the boundaries start to influence the transient response.
4. New analysis equations were presented for Regions 1 to 4.
5. The effect of skin on the response for the constant rate case is different from that for the constant p_{wf} case. The effect of skin shows up as parallel lines with a constant offset for the constant rate case while it diminishes with time for the constant p_{wf} case.

6. A new analytical equation was presented to model the constant p_{wf} effect of skin in a linear reservoir.
7. Different shape factor formulations result in similar Region 4 response when appropriate *f(s)* modifications consistent with λ_{Ac} computations are made.
8. Different matrix geometry exhibit the same Region 4 response when the area-volume ratios are made equivalent.

8.2 Recommendations for Future Work

The following recommendations are listed:

1. Investigation of the effect of water production on the results.
2. Investigation of the effects of adsorption and desorption
3. Investigation of the effects of anisotropy and varying well location.

NOMENCLATURE

A_{cm} = total matrix surface area draining into fracture system, ft^2

A_{cw} = well-face cross-sectional area to flow, ft^2

B = liquid formation volume factor, rB/STB

B_{gi} = formation volume factor at initial reservoir pressure, rcf/scf

c_t = liquid total compressibility, psi^{-1}

c_{ti} = total compressibility at initial reservoir pressure, psi^{-1}

d_z = well position in reservoir , dimensionless

D = diameter, fracture spacing, ft

$f(s)$ = relation used in Laplace space to distinguish matrix geometry types

h = reservoir thickness, ft

$I_o(x)$ = modified Bessel function of first kind, zero order

$I_1(x)$ = modified Bessel function of first kind, first order

$J_o(x)$ = Bessel function of first kind, zero order

k = homogeneous reservoir permeability, md

k_f = bulk fracture permeability of dual porosity models, md

k_m = matrix permeability, md

k_V = vertical permeability, md

k_H = horizontal permeability, md

l =half of fracture spacing, ft

ℓ^{-1} = Inverse Laplace space operator

L = general fracture spacing, ft

L_w = horizontal well length, ft

L_1 = fracture spacing (one-dimensional, slab), ft

L_2 = fracture spacing (two-dimensional, column), ft

L_3 = fracture spacing (three-dimensional, cube), ft

m_{DL} = dimensionless pressure (rectangular geometry, gas)

$\tilde{m}$ = slope of regions 1 to 5 defined in Chapter IV

$m(p)$ = pseudopressure (gas), psi^2/cp

p_i = initial reservoir pressure, psi

p_{wf} = wellbore flowing pressure, psi

p_{DL} = dimensionless pressure based on $A_{cw}^{0.5}$ and k_f (rectangular geometry, liquid, dual porosity)

p_{Drw} = dimensionless pressure based on radial definition *(*formation thickness*, h)*

p_{DH} = dimensionless pressure based on horizontal well length, L_w

p_{Dm} = dimensionless pressure in the matrix

p_{Df} = dimensionless pressure in the fracture

p_f = fracture pressure, psi

p_i = initial pressure, psi

p_{WDL} = dimensionless pressure based on $A_{cw}^{0.5}$ and k_f (rectangular geometry, liquid, dual porosity)

p_{WDLh} = dimensionless pressure based on $A_{cw}^{0.5}$ and k (rectangular geometry, liquid, homogeneous)

p_{WDLm} = dimensionless pressure based on matrix $A_{cm}^{0.5}$ and k_m (rectangular geometry,

liquid)

q_D = dimensionless rate (transient dual porosity model)

q_{DL} = dimensionless rate based on $A_{cw}^{0.5}$ and k_f (rectangular geometry, liquid, dual porosity)

q_{DLh} = dimensionless rate based on $A_{cw}^{0.5}$ and k (rectangular geometry, liquid, homogeneous)

q_{DLm} = dimensionless rate based on matrix $A_{cm}^{0.5}$ and k_m (rectangular geometry, liquid

q_g = gas rate, Mscf/day

Q = cumulative production, STB

r = radial geometry coordinate

r_{mc} = radius of cylinder matrix, ft

r_{ms} = radius of sphere matrix, ft

r_w = wellbore radius , ft

s = Laplace space variable

s_{Ac} = skin definition for linear model (dual porosity) based on k_f and $A_{cw}^{0.5}$

s_{Ach} = skin definition for linear model (homogenenous) based on k and $A_{cw}^{0.5}$

s_{Acm} = skin definition for linear model based on k_m and matrix area $A_{cm}^{0.5}$

s_c = convergence skin

s_H = skin definition based on horizontal well length

s_{rw} = skin definition based on wellbore radius

t = time, days

t_D = dimensionless time coordinate

t_{DAc} =dimensionless time based on A_{cw} and k_f (rectangular geometry, dual porosity)

t_{DAch} =dimensionless time based on A_{cw} and k (rectangular geometry, homogeneous)

t_{DAcm} =dimensionless time based on matrix A_{cm} and k_m (rectangular geometry)

t_{Drw} =dimensionless time (radial definition) based on wellbore radius

T = absolute temperature, ^{o}R

V_{bm} = total matrix bulk volume, ft^3

V_{pm} = matrix pore volume, ft^3

x_e = drainage area width (rectangular geometry), ft

y_e = drainage area half-length (rectangular geometry), ft

y_{De} = dimensionless reservoir length (rectangular geometry)

z = coordinate, z-direction (matrix)

z_D = dimensionless coordinate, z-direction

Greek symbols

α = hydraulic diffusivity term defined in Appendix A

α_n = n_{th} zero of Bessel function, J_o used in Eqs. 3.4, 3.5

γ = specific gravity

λ = dimensionless interporosity parameter

μ = viscosity, cp

ω = dimensionless storativity ratio

ϕ = porosity

σ = shape factor, ft^{-2}

Subscript

Ac = cross-sectional area to flow

i =initial

f =fracture system

g = gas

m =matrix

f+*m* =total system (fracture+matrix)

REFERENCES

1. Shanley, K.W., Robinson, J., and Cluff, R.M.: "Tight-Gas Myths have Strong Implications for Resource Estimation, Policymaking, Operating Strategies," *Oil & Gas J.* (2 August 2004) 25.
2. Ayers, W. B.: "PETE 612 – Unconventional Reservoir Class Notes," Fall 2005.
3. Cook, T.: "Chapter 23: Calculation of Estimated Ultimate Recovery (EUR) for Wells in Continuous Type Oil and Gas Accumulations," www.pubs.usgs.gov /dds/dds-069/dds-069-d/REPORTS/69_D_CH_23.pdf
4. Natural Gas Production, 1990–2020, www.eia.doe.gov/oiaf/analysispaper/ uncon_fig1.html
5. Franz, J.H., Jr. and Jochen,V.: "Shale Gas," Schlumberger White Paper, 2005.
6. Powers, B.: "The Bright Future of Shale Gas," *US Energy Investor* (January 2005) **3**, www.admiralbay.com/global/contentserver/files/1022/151596_The_ Bright_Future_of_Shale_Gas.pdf
7. Ning, X., Fan, J. and Lancaster, D.E.: "Measurement of Shale Matrix and Fracture Properties in Naturally Fractured Cores Using Pulse Testing," *Gas Shales Technology Review* (October 1993) **8**, no. 2, 31-45.
8. Frantz, Jr., J.H., Williamson, J.R., Sawyer, W.K., Johnston, D., Waters, G., Moore, L.P., Macdonald, R.J., Pearcy, M., Ganpule, S.V. and March, K.S.: "Evaluating Barnett Shale Production Performance Using An Integrated Approach," paper SPE 96917 presented at the 2005 Annual Technical Conference and Exhibition, Dallas, Texas, 9 -12 October.

9. Montgomery, S.L., Jarvie, D.M., Bowker, K.A., and Pollastro, R.M..: "Mississipian Barnett Shale, Forth Worth Basin, North-Central Texas: Gas-Shale Play with Multi-Trillion Cubic foot Potential," *AAPG Bulletin* (February 2005) **89**, no. 2, 155-175.
10. Hopkins, C.W., Frantz, Jr., J.H., Hill, D.G. and Zamora, F.: "Estimating Fracture Geometry in the Naturally Fractured Antrim Shale," paper SPE 30483 presented at the 1995 SPE Annual Technical Conference and Exhibition, Dallas, Texas, 22 – 25 October.
11. Analysis of Five Selected Tax Provisions of the Conference Energy Bill of 2003, www.eia.doe.gov/oiaf/servicerpt/ceb/fuel.html
12. Ozkan, E., Ohaeri, U. and Raghavan, R.: "Unsteady Flow to a Well Produced at a Constant Pressure in a Fractured Reservoir," *SPE Formation Evaluation* (June 1987)186-200.
13. Wattenbarger, R.A.: "Some Reservoir Performance Aspects of Unconventional Gas Production," Private Conference Presentation, 2007.
14. Mayerhofer, M.J., Lolon, E.P., Youngblood, J.E. and Heinze, J.R.: "Integration of Microseismic Fracture Mapping Results with Numerical Fracture Network Production Modeling in the Barnett Shale," paper SPE 102103 presented at the 2006 Annual Technical Conference and Exhibition, San Antonio, Texas, 24-27 September.

15. Carlson, E.S. and Mercer, J.C.: "Devonian Shale Gas Production: Mechanisms and Simple Models," paper SPE 19311 presented at the 1989 SPE Eastern Regional Meeting, Morgantown, West Virginia, 24-27 October.

16. El-Banbi, A.H.: "Analysis of Tight Gas Wells," PhD Dissertation, Texas A &M University, May 1998.

17. Barenblatt, G.I., Zheltov, I. P. and Kochina, I.N.: "Basic Concepts in the Theory of Seepage of Homogeneous Liquids in Fissured Rocks (Strata)," *PMM* (1960) **24**, No. 5, 852-864.

18. Warren, J.E. and Root, P.J.: "The Behavior of Naturally Fractured Reservoirs," paper SPE 426 presented at the 1962 Fall Meeting of the Society of Petroleum Engineers, Los Angeles, California, 7 – 10 October.

19. Kazemi, H., Seth, M.S. and Thomas, G.W.: "The Interpretation of Interference Tests in Naturally Fractured Reservoirs with Uniform Fracture Distribution," paper SPE 2156B presented at the 1968 43rd Annual Fall Meeting, Houston, Texas, 29 Sept – 2 October.

20. Odeh, A.S.: "Unsteady-State Behavior of Naturally Fractured Reservoirs," *Soc. Pet. Eng. J.*, (March 1964) 60-66.

21. Mavor, M.J. and Cinco-Ley, H.: "Transient Pressure Behavior of Naturally Fractured Reservoirs," paper SPE 7977 presented at the 1979 California Regional Meeting of the Society of Petroleum Engineers of AIME, Ventura, California, 18 – 20 April.

22. Da Prat, G., Cinco-Ley, H. and Ramey Jr., H.J.: "Decline-Curve Analysis Using Type Curves for Two-Porosity Systems," paper SPE 9292 presented at the 1981 SPE 54th Technical Conference and Exhibition, Dallas, Texas, 23-26 September.
23. Bui, T.D., Mamora, D.D. and Lee, W.J.: "Transient Pressure Analysis for Partially Penetrating Wells in Naturally Fractured Reservoirs," paper SPE 60289 2000 Annual Technical Conference and Exhibition, Denver, Colorado, 12-15 March.
24. Kazemi, H.: "Pressure Transient Analysis of Naturally Fractured Reservoirs with Uniform Fracture Distribution," paper SPE 2156A presented at the 1968 43rd Annual Fall Meeting, Houston, Texas, 29 September – 2 October.
25. De Swaan, A.: "Analytic Solutions for Determining Naturally Fractured Reservoir Properties by Well Testing," paper SPE 5346 presented at the 1975 SPE-AIME 45th Annual California Regional Meeting, Ventura, California, 2-4 April.
26. Najurieta, H.L.: "A Theory for Pressure Transient Analysis in Naturally Fractured Reservoirs," *JPT* (July 1980) 1241.
27. Serra, K., Reynolds, A.C. and Raghavan, R.: "New Pressure Transient Analysis Methods for Naturally Fractured Reservoirs," paper SPE 10780 presented at the 1982 SPE California Regional Meeting, San Francisco, California, 24-26 March.
28. Chen, C-C., Serra, K., Reynolds, A.C. and Raghavan, R.: "Pressure Transient Analysis Methods for Bounded Naturally Fractured Reservoirs," *SPEJ* (June 1985) 451-464.

29. Streltsova, T.D.: "Well Pressure Behavior of a Naturally Fractured Reservoir," paper SPE 10782 presented at the 1982 California Regional Meeting, San Francisco, California, 24-26 March.

30. Cinco-Ley, H. and Samaniego, V-F., "Pressure Transient Analysis for Naturally Fractured Reservoirs," paper SPE 11026 presented at the 57th 1982 Annual Technical Conference and Exhibition of the Society of Petroleum Engineers of AIME, New Orleans, Louisiana, 26 – 29 September.

31. Lai, C.H., Bodvarsson, G.S., Tsang, C.F. and Witherspoon, P.A.: "A New Model for Well Test Data Analysis for Naturally Fractured Reservoirs," paper SPE 11688 presented at the 1983 California Regional Meeting, Ventura, California, 23-25 March.

32. Houze, O.P., Horne, R.N. and Ramey, Jr., H.J.: "Pressure Transient Response of an Infinite Conductivity Vertical Fracture in a Reservoir with Double Porosity Behavior," *SPE Formation Evaluation* (September 1988) 510-518.

33. Stewart, G. and Ascharsobbi, F.: "Well Test Interpretation for Naturally Fractured Reservoirs," paper SPE 18173 presented at the 1988 Annual Technical Conference and Exhibition, Houston, Texas, 2-5 October.

34. Kucuk, F., and Sawyer, W.K.: "Modeling of Devonian Shale Gas Reservoir Performance," Proceedings of Third Eastern Gas Shales Symposium, Morgantown, West Virginia, (1979) 1 – 3 October.

35. Kucuk, F., and Sawyer, W.K.: "Transient Flow in Naturally Fractured Reservoirs and Its Application to Devonian Gas Shales," paper SPE 9397 presented at the

1980 Annual Fall Technical Conference and Exhibition of the Society of Petroleum Engineers of AIME, Dallas, Texas, 21-24 September.

36. Gatens III, J.M., Lee, W.J., Lane, H.S., Watson, A.T., Stanley, D.K. and Lancaster, D.E.: "Analysis of Eastern Devonian Gas Shales Production Data," paper SPE 17059 presented at the 1987 SPE Eastern Regional Meeting, Pittsburgh, Pennsylvania, 21-23 October.
37. Watson, A.T., Gatens III, J.M., Lee, W.J. and Rahim, Z.: "An Analytical Model for History Matching Naturally Fractured Reservoir Production Data," paper SPE 18856 presented at the 1989 Production Operations Symposium, Oklahoma City, Oklahoma, 13-14 March.
38. Spivey, J.P. and Semmelbeck, M.E.: "Forecasting Long-Term Gas Production of Dewatered Coal Seams and Fractured Gas Shales," paper SPE 29580 presented at the 1995 Rocky Mountain Regional/Low Permeability Reservoirs Symposium, Denver, Colorado, 20 -22 March.
39. Gringarten, A.C., Ramey Jr., H.J. and Raghavan, R.: "Unsteady-State Pressure Distributions Created by a Well with a Single Infinite Conductivity Vertical Fracture," paper SPE 4051 presented at the 1972 SPE-AIME 47th Annual Fall Meeting, San Antonio, Texas, 8 – 11 October.
40. Clonts, M.D. and Ramey Jr., H.J.: "Pressure Transient Analysis for Wells with Horizontal Drainholes," paper SPE 15116 presented at the 1986 California Regional Meeting, Oakland, California, 2-4 April.

41. Ozkan, E.: “Performance of Horizontal Wells,” PhD Dissertation, University of Tulsa, 1988.

42. Ozkan, E., Raghavan, R. and Joshi, S.D.: “Horizontal-Well Pressure Analysis,” *SPE Formation Evaluation* (December 1989) 567-575.

43. Ozkan, E. and Raghavan, R**.:** “New Solutions for Well-Test Analysis Problems: Part 1 – Analytical Considerations,” *SPE Formation Evaluation* (September 1991) 359-368.

44. Ozkan, E. and Raghavan, R**.:** “New Solutions for Well-Test Analysis Problems: Part 2 – Computational Considerations and Applications,” *SPE Formation Evaluation* (September 1991) 369-378.

45. Rosa, A.J. and de Souza Carvalho, R.: “A Mathematical Model for Pressure Evaluation in an Infinite Conductivity Horizontal Well,” *SPE Formation Evaluation* (December 1989) 559-566.

46. Ohaeri, C.U. and Vo, D.T.: “Practical Solutions for Interactive Horizontal Well Test Analysis,” paper SPE 22729 presented at the presented at the 1991 Annual Technical Conference and Exhibition, Dallas, Texas, 6-9 October.

47. Goode, P.A. and Thambynayagam, R.K.M.: “Pressure Drawdown and Buildup Analysis of Horizontal Wells in Anisotropic Media,” paper SPE 14250 presented at the 1985 Annual Technical Conference and Exhibition, Las Vegas, Nevada, 22-25 September.

48. Daviau, F., Mouronval, G., Bourdarot, G. and Curutchet, P.: “Pressure Analysis for Horizontal Wells,” *SPE Formation Evaluation* (December 1988) 716-724.

49. Kuchuk, F.J., Goode, P.A., Wilkinson, D.J. and Thambynayagam, R.K.M.: "Pressure-Transient Behavior of Horizontal Wells with and Without Gas Cap or Aquifer," *SPE Formation Evaluation* (March 1991) 86-94.

50. Kuchuk, F.J.: "Well Testing and Interpretation for Horizontal Wells," *Distinguished Author Series , JPT* (1995) 36 - 41.

51. Odeh, A.S. and Babu, D.K.: "Transient Flow Behavior of Horizontal Wells: Pressure Drawdown and Buildup Analysis," paper SPE 18802 presented at the 1989 California Regional Meeting, Bakersfield, California, 5-7 April.

52. de S. Carvalho, R. and Rosa, A.J.: "Transient Pressure Behavior for Horizontal Wells in Naturally Fractured Reservoir," paper SPE 18302 presented at the 1988 Annual Technical Conference and Exhibition, Houston, Texas, 2-5 October.

53. Aguilera, R. and Ng, M.C.: "Transient Pressure Analysis of Horizontal Wells in Anisotropic Naturally Fractured Reservoirs," paper SPE 19002 presented at the 1989 Rocky Mountain Regional/Low Permeability Reservoir Symposium and Exhibition, Denver, Colorado, 6-8 March.

54. Ng, M.C. and Aguilera, R.: "Well Test Analysis of Horizontal Wells in Bounded Naturally Fractured Reservoirs," *Journal of Canadian Petroleum Technology* (July 1999) **38**, no. 7, 20-24.

55. Thompson, L.G., Manrique, J.L. and Jelmert, T.A.: "Efficient Algorithms for Computing the Bounded Reservoir Horizontal Well Pressure Response," paper SPE 21827 presented at the 1991 Rocky Mountain Regional Meeting and Low-Permeability Reservoirs Symposium, Denver, Colorado, 15-17 April.

56. Stehfest, H.: “Algorithm 358 – Numerical Inversion of Laplace Transforms,” *Comm. ACM* (Jan 1970) 13, no. 1, 47-49.

57. Roumbostos, A. and Stewart, G.: “A Direct Deconvolution or Convolution Algorithm for Well Test Analysis,” paper SPE 18157 presented at 1988 Annual Technical Conference and Exhibition, Houston, 2-5 October.

58. Du, Kui-Fu and Stewart,G.: “Transient-Pressure Response of Horizontal Wells in Layered and Naturally Fractured Reservoirs with Dual-Porosity Reservoirs,” paper SPE 24682 presented at the 1992 Annual Technical Conference and Exhibition, Washington, DC, 4-7 October.

59. Van Everdingen and Hurst,W.: “The Application of Laplace Transformation to Flow Problems in Reservoirs,” *Petroleum Transactions, AIME* (December 1949) 305-324.

60. Lichtenberger, G.J.: “Data Acquisition and Interpretation of Horizontal Well Pressure-Transient Tests,” paper SPE 25922 presented at the 1993 Rocky Mountain Regional/Low Permeability Reservoirs Symposium, Denver, Colorado, 12 -14 April.

61. Kazemi, H., Merrill, L.S., Porterfield, K.L. and Zeman, P.R.: “Numerical Simulation of Water-Oil Flow in Naturally Fractured Reservoirs,” paper SPE 5719 presented at the 1976 SPE-AIME Fourth Symposium on Numerical Simulation of Reservoir Performance, Los Angeles, California,19 -20 February.

62. Coats, K.H.: "Implicit Compositional Simulation of Single-Porosity and Dual-Porosity Reservoirs," paper SPE 18427 presented at the 1989 Symposium on Reservoir Simulation, Houston, Texas, 6-8 February.

63. Ueda, Y., Murata, S., Watanabe, Y. and Funatsu, K.: "Investigation of the Shape Factor used in the Dual-Porosity Reservoir Simulator," paper SPE 19469 presented at the 1989 Asia-Pacific Conference, Sydney, Australia, 13-15 September.

64. Zimmerman, R.W., Chen, G., Hadgu, T. and Bodvarsson,G.S.: "A Numerical Dual-Porosity Model with Semianalytical Treatment of Fracture/Matrix Flow," *Water Resources Research* (July 1993) **29**, no. 7, 2121-2137.

65. Chang, M.: "Deriving the Shape Factor of a Fractured Rock Matrix," Topical Report, US Department of Energy, DE-FC22-83FE60149, September 1993.

66. Lim, K.T. and Aziz, K.: "Matrix-Fracture Transfer Shape Factors for Dual-Porosity Simulators," *Journal of Petroleum Science and Engineering* (1995) **13**, 169-178.

67. Sarda, S., Jeannin, L., Basquet, R. and Bourbiaux, B.: "Hydraulic Characterization of Fractured Reservoirs: Simulation on Discrete Fracture Models," paper SPE 77300 presented at the 2001 Reservoir Simulation Symposium, Houston, Texas, 11-14 February.

68. Hassanzadeh, H. and Pooladi-Darvish, M.: "Effects of Fracture Boundary Conditions on Matrix-Fracture Transfer Shape Factor," *Transport in Porous Media* (2006) 64, .51-71.

69. Mora, C.A. and Wattenbarger, R.A.: "Analyst and Verification of Dual Porosity and CBM Shape Factors," paper CIPC 2006-139 presented at the 7th International Petroleum Engineering Conference, Calgary, Alberta, 13-15 June.

70. Bello, R.O. and Wattenbarger, R.A.: "Rate Transient Analysis in Naturally Fractured Shale Gas Reservoirs," paper SPE 114591 presented at the 2008 CIPC/SPE Gas Technology Symposium Joint Conference, Calgary, Alberta, 16-19 June.

71. Earlougher, R.C.: *Advances in Well Test Analysis,* Society of Petroleum Engineers of AIME, New York (1977).

72. Carslaw, H.S. and Jaeger, J.C.: *Conduction of Heat in Solids*, 2nd ed., Oxford, Clarendon Press (1959).

APPENDIX A

SINGLE MATRIX BLOCK DRAINAGE

AT CONSTANT PRESSURE

A-1 Overview

As previously described, the dual porosity model of a naturally fractured reservoir is composed of matrix blocks draining into surrounding fractures at constant pressure (the most widely used boundary condition in the literature). It was mentioned in Chapter I that the drainage of these matrix blocks is the cause of the transient linear regime observed in the shale gas wells. In this section, drainage of single matrix blocks will be investigated. Three methods will be used to illustrate and compare constant pressure drainage of matrix blocks of different geometries – slab, cylinder and sphere. The cylinder and sphere geometries have been used in the literature as approximations to the ideal two-dimensional (column) and three-dimensional (cube) geometries. This will be demonstrated for the slightly compressible fluid case. The results are expected to be applicable to the compressible gas case. These methods are numerical simulation, analytical solution and Laplace space solutions. The development of the equations for the analytical and Laplace space solutions are shown only for the slab case in Section A-2. Data common to three matrix geometries is shown in Table A-1

A-10 SLAB MATRIX

Data specific to the slab case is shown in Table A-2. A schematic of the slab matrix is shown in Fig. A-1. The three methods will subsequently be presented.

A-10.1 Numerical Simulation

The simulation was conducted using two numerical simulators – *GASSIM* and *ECLIPSE* version 2007.1 (Schlumberger). A 101 x 1 x 1 grid system was utilized in both simulators with Δx = 0.5 ft, Δy = 1000 ft and Δz = 10 ft. The 101st grid contains the well (constant bottomhole pressure of 100 psi) and was assigned a small porosity of 10^{-8} and high permeability of 10^{11} md to model the constant pressure condition at the boundary of the slab. It was found by comparing with the analytical solution that maximum timestep sizes of 0.05 (*GASSIM*) and 0.001(*ECLIPSE*) were required to give accurate results.

Table A-1 – Data for the Slab, Cylinder and Sphere Matrix.	
k_m	0.1 md
ϕ	0.065
μ	1 cp
c_t	15 x 10^{-6} psi^{-1}
B	1 RB/STB

Table A-2 – Data for the Slab Matrix Case.	
l (half of fracture spacing)	50 ft
p_f	100 psi
p_i	1000 psi
V_p	32,500 ft^3
a (one dimension on fracture face)	1000 ft
b (other dimension on fracture face)	10 ft
A_{cm} *(= a x b)*	10,000 ft^2

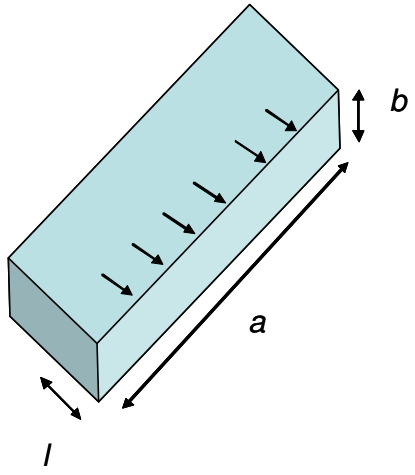

Fig. A-1 – Schematic of Slab Matrix.

A-10.2 Analytical Solution

The development of the equations for the slab matrix case is illustrated in Appendix A-2. The two equations used are :

$$q = \frac{V_{bm}\phi c_t}{B}\frac{2\alpha}{l^2}\left(p_i - p_f\right)\sum_{n=0}^{\infty} e^{-\left(\frac{\alpha(2n+1)^2\pi^2 t}{4l^2}\right)} \qquad \text{(Method I)} \quad \text{.....(A-1)}$$

$$q = -0.00633\frac{k_m A_{cm}}{\mu}\frac{2}{l}\left(p_f - p_i\right)\sum_{n=0}^{\infty}(-1)^n e^{-\left(\frac{\alpha(2n+1)^2\pi^2 t}{4l^2}\right)} \sin\left[(2n+1)\frac{\pi}{2}\right]$$

(Method II) ....(A-2)

Where α is the hydraulic diffusivity defined in Appendix A as

$$\alpha = \frac{0.00633k_m}{\phi\mu c_t}$$

A-10.3 Laplace Space Solution

The development of the equation for the slab matrix case is illustrated in Appendix A-2. The equation is given by

$$q = -0.00633\frac{k_m A_{cm}}{\mu}\ell^{-1}\left[\frac{d\overline{p_m}}{dz}\right]_{z=L/2} \qquad \text{.....(A-3)}$$

where $\left.\frac{d\overline{p_m}}{dz}\right|_{z=L/2} = \frac{2}{L}\sqrt{s}\left(\frac{p_f - p_i}{s}\right)\tanh\sqrt{s}$ and is inverted numerically using a Laplace space inversion algorithm and substituted into Eq. A.3.

The results from all the tests are shown in Fig. A-2. It can be observed from Fig. A-2 that the results from all the methods are similar and exhibit an initial transient linear

response (one-half slope on a log-log plot) and a boundary-dominated response at later times.

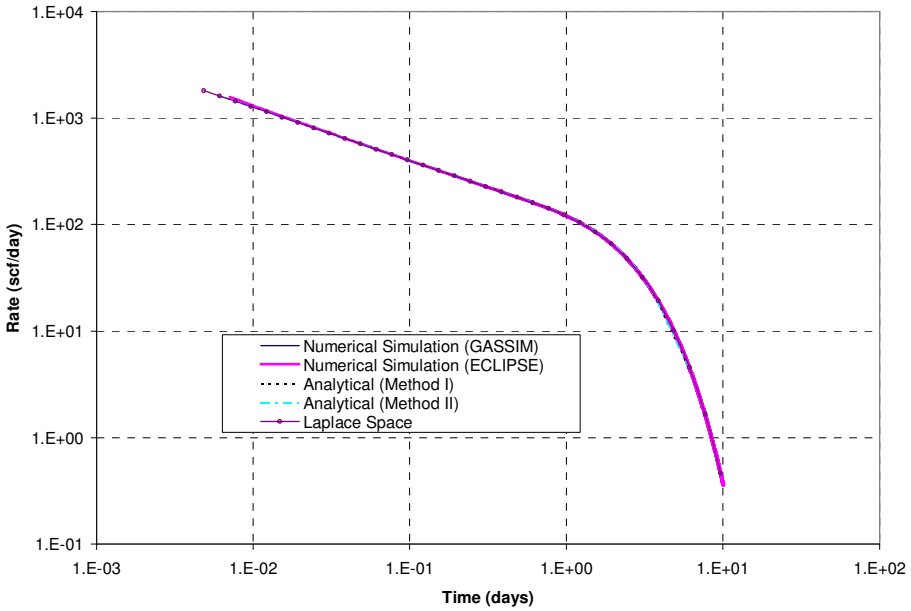

Fig. A-2 – Comparison of Slab Matrix Drainage Results. All methods exhibit similar initial transient linear response and later boundary dominated response.

A-11 CYLINDER MATRIX

Data specific to the cylinder case is shown in Table A-3. The three methods will subsequently be presented.

A-11.1 Numerical Simulation

The simulation was conducted using two numerical simulators – *GASSIM* and *ECLIPSE* version 2007.1 (Schlumberger). A 101 x 1 radial grid system (Δr = 1 ft, Δz = 1 ft) was utilized in *GASSIM* while a 201 x 1 radial grid (Δr =0.5 ft, Δz = 1 ft was utilized in

ECLIPSE. The 101st and 201st grid in *GASSIM* and *ECLIPSE* respectively contain the well (constant bottomhole pressure of 100 psi) and was assigned a small porosity of 10^{-4} and high permeability of 10^6 md to model the constant pressure condition at the boundary of the slab. It was found by comparing with the analytical solution that maximum timestep sizes of 0.05 (*GASSIM*) and 0.01(*ECLIPSE*) were required to give accurate results.

Table A-3 – Data for the Cylinder Matrix Case.	
r_{mc}	100 ft
p_f	100 psi
p_i	1000 psi
V_{pm}	2,042 ft^3
h	1 ft
A_{cm}	628 ft^2

A-11.2 Analytical Solution

The two equations developed using methods similar to the slab matrix case are:

$$q = \frac{V_{bm}\phi c_t}{B}\left[\alpha\left(p_i - p_f\right)\frac{4}{r_{mc}^2}\sum_{n=1}^{\infty} e^{-\alpha\alpha_n^2 t}\right] \qquad \text{(Method I)} \quad \text{.....(A-4)}$$

$$q = -0.00633\frac{k_m A_{cm}}{\mu}\left(p_f - p_i\right)\frac{2}{r_{mc}}\sum_{n=1}^{\infty} e^{-\alpha\alpha_n^2 t} \qquad \text{(Method II)} \quad \text{.....(A-5)}$$

Where α is the hydraulic diffusivity defined in Appendix A as

$$\alpha = \frac{0.00633 k_m}{\phi \mu c_t}$$

and α_n is the n_{th} zero of the Bessel function J_o

A-11.3 Laplace Space Solution

The equation developed using methods similar to the slab matrix case is given by

$$q = -0.00633 \frac{k_m A_{cm}}{\mu} \ell^{-1} \left[\frac{d\overline{p_m}}{dr} \right]_{r=r_{mc}} \qquad \text{.....(A-6)}$$

where $\left| \frac{d\overline{p_m}}{dr} \right|_{r=r_{mc}} = \frac{\sqrt{s}}{r_{mc}} \left(\frac{p_f - p_i}{s} \right) \frac{I_1 \sqrt{s}}{I_o \sqrt{s}}$ and is inverted numerically using a Laplace space inversion algorithm and substituted into Eq. A-6.

I_o, I_1 are modified Bessel functions.

The results from all the tests are shown in Fig. A-3. It can be observed from Fig. A-3 that the results from all the methods are similar and exhibit an initial transient linear response (one-half slope on a log-log plot) and a boundary-dominated response at later times.

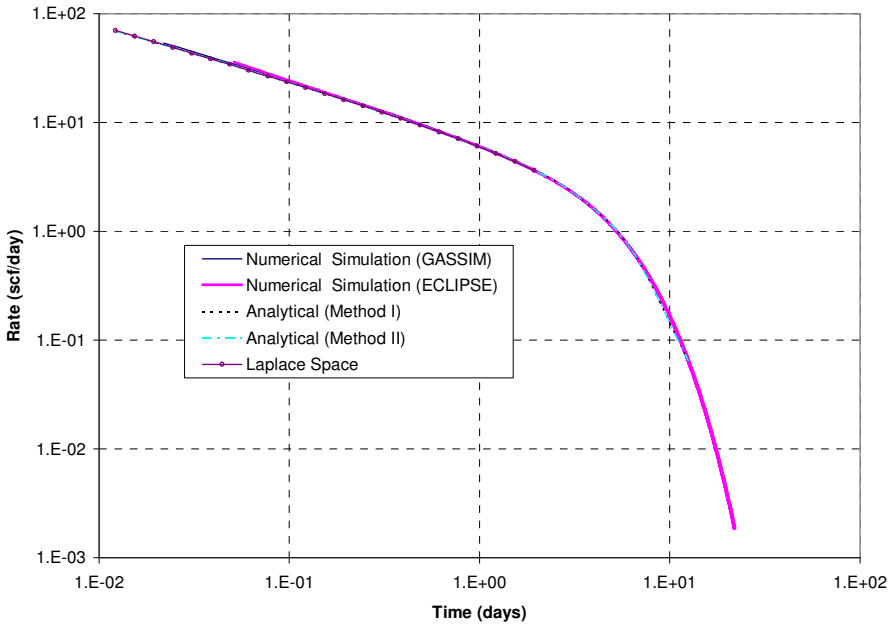

Fig. A-3 – Comparison of Cylinder Matrix Drainage Results. All methods exhibit similar initial transient linear response and later boundary dominated response

A-12 SPHERE MATRIX

Data specific to the sphere case is shown in Table A-4. The three methods will subsequently be presented.

A-12.1 Numerical Simulation

There is no available simulator for the sphere case. An attempt will be made to simulate the sphere matrix case using the numerical simulator *GASSIM*. The cylinder case will be adapted to simulate the sphere case by using fictitious transmissibilities and porosity.

Our equation for the required pore volume (grid) of a sphere is given by

$$V_{pm} = \frac{4}{3}\pi\left(r_2^3 - r_1^3\right)h\phi \qquad \text{.....(A-7)}$$

Where $\phi = 0.065$ as given in Table A-1

r_1 and r_2 are inner and outer radial grid dimensions

The equation for the pore volume (grid) of a cylinder is thus given by

$$V_{pm} = \pi\left(r_2^2 - r_1^2\right)h\phi_s \qquad \text{.....(A-8)}$$

ϕ_s is a fictitious porosity that will be input into the simulator (cylinder case) to yield the required sphere pore volume.

The transmissibility of the sphere (grid) is given by

$$T_1 = 0.00633\frac{r_1 r_2 4\pi k}{r_2 - r_1} \qquad \text{.....(A-9)}$$

The transmissibility of the cylinder (grid) is thus given by

$$T_2 = (0.00633)(2\pi)\frac{hk_s}{\ln\left(r_2/r_1\right)} \qquad \text{.....(A-10)}$$

k_s is a fictitious permeability that will be input into the simulator (cylinder case) to behave like the sphere.

A 101 x 1 radial grid system (Δr = 1 ft, Δz = 10 ft) was utilized.

Table A-4 – Data for the Sphere Matrix Case.	
r_{ms}	100 ft
p_f	100 psi
p_i	1000 psi
V_{pm}	272,271 ft^3
A_{cm}	125,664 ft^2

A-12.2 Analytical Solution

The two equations developed using methods similar to the slab matrix case are

$$q = \frac{V_{bm}\phi c_t}{B}\frac{\alpha n^2\pi^2}{r_{ms}^2}\left[\left(p_i - p_f\right)\frac{6}{\pi^2}\sum_{n=1}^{\infty}\frac{1}{n^2}e^{-\alpha n^2\pi^2 t/r_m^2}\right] \qquad \text{(Method I)} \qquad \text{.....(A-11)}$$

$$q = -0.00633\frac{k_m A_{cm}}{\mu}\left(p_f - p_i\right)\sum_{n=1}^{\infty}\frac{2n}{r_{ms}}\frac{(-1)^n}{n}(\cos n\pi)e^{-\alpha^2 n^2\pi^2 t/r_{ms}^2} \quad \text{(Method II)} \quad \text{.....(A-12)}$$

A-12.3 Laplace Space Solution

The equation developed using methods similar to the slab matrix case are

$$q = -0.00633\frac{k_m A_{cm}}{\mu}\ell^{-1}\left[\frac{d\overline{p_m}}{dz}\right]_{r=r_{ms}} \qquad \text{.....(A-13)}$$

where $\left|\frac{d\overline{p_m}}{dr}\right|_{r=r_{ms}} = \frac{1}{r_{ms}}\left(\frac{p_f - p_i}{s}\right)\left[\sqrt{s}Coth\left(\sqrt{s}\right) - 1\right]$ and is inverted numerically using a Laplace space inversion algorithm and substituted into Eq. A-13.

The results from all the tests are shown in Fig. A-4. It can be observed from Fig. A-4 that the results from Analytical methods and Laplace exhibit similar initial transient linear response. Numerical simulation is not similar to the other methods. It is possible that a match with the other methods might be obtained with a smaller maximum timestep (0.05 days was used in this work) and smaller grids.

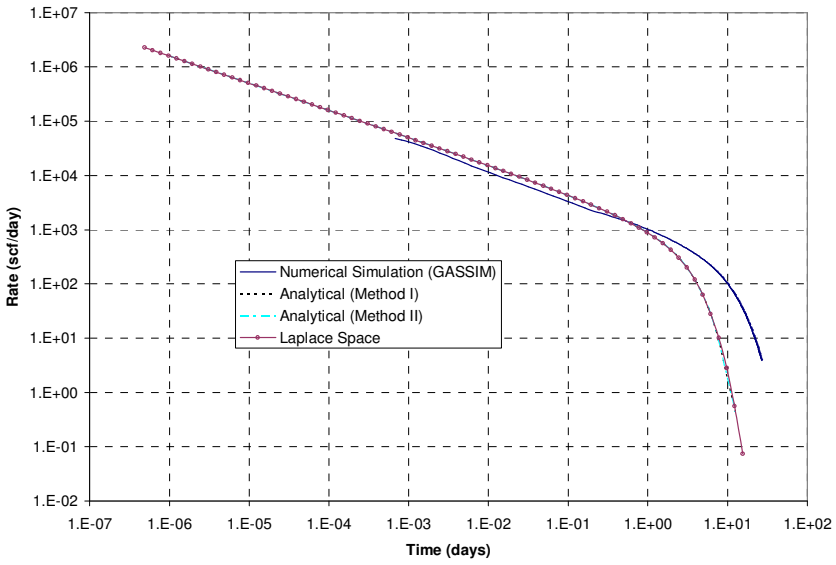

Fig. A-4 – Comparison of Sphere Matrix Drainage Results. Analytical and Laplace space solutions exhibit similar response. Numerical simulation is different probably due to approximations.

Summary

Matrix drainage at constant pressure was investigated using different methods. It can be concluded from Figs. A-2 to A-4 that drainage of matrix blocks of any geometry at constant pressure boundary condition results in transient linear flow (one-half slope on a log-log plot). This is one of the possible causes of the observed transient linear flow regime in the shale gas wells as discussed in Chapter I.

A-2 Derivation of Equations for Slab Matrix Case

In this section, the development of an equation for one –dimensional slab geometry matrix drainage at constant pressure is shown using analogy with heat flow principles from Carslaw and Jaeger[72]

The underlying assumptions are stated thus:

- Incompressible fluid
- Constant fluid properties
- The slab is initially at the same initial pressure
- One boundary is at constant pressure

A-20 Analytical solution (Method I)

Half of the slab is modeled. The length of which is given by

$$l = \frac{L}{2}$$

The following expression can be written for the pressure distribution

$$\frac{\bar{p} - p_i}{p_f - p_i} = \frac{8}{\pi^2} \sum_{n=0}^{\infty} \frac{1}{(2n+1)^2} e^{-\frac{\alpha(2n+1)^2 \pi^2 t}{4l^2}} \qquad \text{.....(A-14)}$$

where p_f is the constant pressure boundary condition, $\bar{p}$ is the average pressure and p_i is the initial pressure

and $\alpha = \dfrac{0.00633k_m}{\phi\mu c_t}$

From Eq. A-14,

$$\bar{p} = p_i + (p_f - p_i)\frac{8}{\pi^2}\sum_{n=0}^{\infty}\frac{1}{(2n+1)^2}e^{-\frac{\alpha(2n+1)^2\pi^2 t}{4l^2}} \qquad \text{.....(A-15)}$$

The fluid content at any time is given by

$$Q = \frac{V_{bm}\phi c_t \bar{p}}{B} \qquad \text{.....(A-16)}$$

differentiating Eq. A-16

$$\frac{dQ}{dt} = \frac{V_{bm}\phi c_t}{B}\frac{d\bar{p}}{dt} \qquad \text{.....(A-17)}$$

Differentiating Eq. A-15

$$\frac{d\bar{p}}{dt} = \frac{-\alpha(2n+1)^2\pi^2}{4l^2}\left[(p_f - p_i)\frac{8}{\pi^2}\sum_{n=0}^{\infty}\frac{1}{(2n+1)^2}e^{-\frac{\alpha(2n+1)^2\pi^2 t}{4l^2}}\right]$$

$$\frac{d\bar{p}}{dt} = -\frac{2\alpha}{l^2}(p_f - p_i)\sum_{n=0}^{\infty}e^{-\frac{\alpha(2n+1)^2\pi^2 t}{4l^2}} \qquad \text{.....(A-18)}$$

Substituting Eq. A-18 in Eq. A-17

$$\frac{dQ}{dt} = \frac{V_{bm}\phi c_t}{B}\frac{2\alpha}{l^2}(p_i - p_f)\sum_{n=0}^{\infty}e^{-\frac{\alpha(2n+1)^2\pi^2 t}{4l^2}} \qquad \text{.....(A-19)}$$

And thus rate (scf/day) is given by

$$q = \frac{dQ}{dt}$$

$$q = \frac{V_{bm}\phi c_t}{B}\frac{2\alpha}{l^2}(p_i - p_f)\sum_{n=0}^{\infty}e^{-\frac{\alpha(2n+1)^2\pi^2 t}{4l^2}} \qquad \text{.....(A-20)}$$

A-21 Analytical solution (Method II)

The following expression can also be written for the pressure distribution

$$\frac{p - p_i}{p_f - p_i} = 1 - \frac{4}{\pi}\sum_{n=0}^{\infty}\left(\frac{(-1)^n}{2n+1}\right)e^{\frac{-\alpha(2n+1)^2\pi^2 t}{4l^2}}\cos\left[\frac{(2n+1)}{2l}\pi x\right] \qquad \text{.....(A-21)}$$

$$p=\left(p_f-p_i\right)-\left(p_f-p_i\right)\frac{4}{\pi}\sum_{n=0}^{\infty}\left(\frac{(-1)^n}{2n+1}\right)e^{\frac{-\alpha(2n+1)^2\pi^2 t}{4l^2}}\cos\left[\frac{(2n+1)}{2l}\pi x\right]+p_i$$

……(A-22)

Differentiating Eq. A-22

$$\frac{\partial p}{\partial x}=\frac{(2n+1)\pi}{2l}\left(p_f-p_i\right)\frac{4}{\pi}\sum_{n=0}^{\infty}\left(\frac{(-1)^n}{2n+1}\right)e^{\frac{-\alpha(2n+1)^2\pi^2 t}{4l^2}}\sin\left[\frac{(2n+1)}{2l}\pi x\right]$$

……(A-23)

$$\left.\frac{\partial p}{\partial x}\right|_{x=l}=\frac{(2n+1)\pi}{2l}\left(p_f-p_i\right)\frac{4}{\pi}\sum_{n=0}^{\infty}\left(\frac{(-1)^n}{2n+1}\right)e^{\frac{-\alpha(2n+1)^2\pi^2 t}{4l^2}}\sin\left[\frac{(2n+1)}{2l}\pi l\right]$$

……(A-24)

$$\left.\frac{\partial p}{\partial x}\right|_{x=l}=\frac{2}{l}\left(p_f-p_i\right)\sum_{n=0}^{\infty}(-1)^n e^{\frac{-\alpha(2n+1)^2\pi^2 t}{4l^2}}\sin\left[(2n+1)\frac{\pi}{2}\right]$$ ……(A-25)

$$\frac{q}{A_{cm}}=-0.00633\frac{k_m}{\mu}\left[\frac{\partial p}{\partial x}\right]_{x=l}$$ ……(A-26)

Thus rate is given by

$$q=-0.00633\frac{k_m A_{cm}}{\mu}\frac{2}{l}\left(p_f-p_i\right)\sum_{n=0}^{\infty}(-1)^n e^{\frac{-\alpha(2n+1)^2\pi^2 t}{4l^2}}\sin\left[(2n+1)\frac{\pi}{2}\right]$$

……(A-27)

A-22 Laplace Space Solution

This method utilizes a form of the matrix-fracture source term normally utilized in the dual porosity equations.

The following dimensionless variable definitions are used.

$$p_D=\frac{kh\left(p_i-p\right)}{141.2qB\mu}\qquad t_{DL}=0.00633\frac{k_m t}{\phi\mu c_t\left(L/2\right)^2}\qquad z_D=\frac{z}{L/2}$$ ……(A-28)

The diffusivity equations for the matrix and fracture and the boundary conditions are stated below:

Matrix

$$\frac{\partial^2 p_m}{\partial z^2} = \left(\frac{\phi\mu c_t}{k}\right)_m \frac{\partial p_m}{\partial t} \qquad \text{……(A-29)}$$

Initial condition: $p_m(z,0) = p_i$

Inner boundary: at $z = 0, \frac{\partial p_m}{\partial z} = 0$ (line of symmetry)

Outer boundary: at $z = \frac{L}{2}, p_m = p_f$

Converting Eq. A-29 to dimensionless variables

$$\frac{\partial^2 p_{Dm}}{\partial z_D^2} = \frac{\partial p_{Dm}}{\partial t_D}$$

The Initial condition in Eq. A-29 becomes in dimensionless variables

$$p_{Dm}(z_D,0) = 0 \qquad \text{……(A-30)}$$

The Inner boundary condition in Eq. A-29 becomes in dimensionless variables

$$\left|\frac{\partial p_{Dm}}{\partial z_D}\right|_{z_D=0} = 0 \qquad \text{……(A-31)}$$

The outer boundary condition in Eq. A-29 becomes in dimensionless variables

$$\left|p_{Dm}\right|_{z_D=1} = p_{Df} \qquad \text{……(A-32)}$$

Transforming Eqs. A-29, A-30, A-31 and A-32 into Laplace space

$$\frac{d^2\overline{p_{Dm}}}{dz_D^2} = \left[s\,\overline{p_{Dm}} - \overline{p_{Dm}}(z_D,0)\right] \qquad \text{……(A-33)}$$

initial condition: $\overline{p_{Dm}}(z_D,0) = 0$

inner boundary: $\left|\frac{d\overline{p_{Dm}}}{dz_D}\right|_{z_D=0} = 0$

outer boundary: $\left|\overline{p_{Dm}}\right|_{z_D=1} = \overline{p_{Df}}$

The general solution is given by

$$\overline{p_{Dm}} = A\cosh\sqrt{s}z_D + B\sinh\sqrt{s}z_D \qquad \text{……(A-34)}$$

and A and B are determined as

$$A = \frac{\overline{p_{Df}}}{\cosh\sqrt{s}}$$

$B = 0$

and Eq. A-34 becomes $\overline{p_{Dm}} = \overline{p_{Df}} \dfrac{\cosh \sqrt{s} z_D}{\cosh \sqrt{s}}$ ……(A-35)

Transforming Eq. A-35;

$$\overline{p_m} = \frac{p_i}{s} + \left(\frac{p_f - p_i}{s} \right) \left(\frac{\cosh \sqrt{s} \dfrac{z}{L/2}}{\cosh \sqrt{s}} \right) \quad \text{……(A-36)}$$

$$\frac{d\overline{p_m}}{dz} = \frac{2}{L} \sqrt{s} \left(\frac{p_f - p_i}{s} \right) \frac{\sinh \sqrt{s} \dfrac{z}{L/2}}{\cosh \sqrt{s}} \quad \text{……(A-37)}$$

$$\left. \frac{d\overline{p_m}}{dz} \right|_{z=L/2} = \frac{2}{L} \sqrt{s} \left(\frac{p_f - p_i}{s} \right) \tanh \sqrt{s} \quad \text{……(A-38)}$$

Eq. A-38 is inverted using the Stehfest algorithm. It should be noted that the inverse of the Laplace variable, s is the dimensionless variable t_{DL}. This is then converted to time, t using the dimensionless variable definitions in Eq. A-28.

$$q = -0.00633 \frac{k_m A_{cm}}{\mu} \left[\frac{\partial p_m}{\partial z} \right]_{z=L/2} \quad \text{……(A-39)}$$

APPENDIX B

LINEAR DUAL POROSITY MODEL

Derivations for the linear dual porosity model (slab matrix, constant rate, bounded rectangular reservoir) are shown in this section. The assumptions relevant to the model are stated:

Naturally fractured reservoir is made up of matrix and fractures (dual-porosity)

Both porous media are homogeneous and isotropic

Matrix acts as a uniformly distributed source for the fractures

Fluid flows through the fractures to the wellbore

Flow of a slightly compressible fluid of constant viscosity

Reservoir is a bounded rectangular reservoir with a well at the centre producing at constant rate

The following dimensionless variables are defined

Dimensionless time: $$t_{DAc} = \frac{0.00633 k_f t}{\left[\left[\phi c_t\right]_m + \left[\phi c_t\right]_f\right] \mu A_{cw}}$$

Dimensionless pressure: $$p_{DL} = \frac{k_f \sqrt{A_{cw}} (p_i - p)}{141.2 qB\mu}$$

Storativity: $$\omega = \frac{\left[\phi c_t\right]_f}{\left[\phi c_t\right]_m + \left[\phi c_t\right]_f}$$

Interporosity flow parameter: $$\lambda_{Ac} = \alpha \frac{k_m}{k_f} A_{cw}$$

Dimensionless length coordinate: $$z_D = \frac{z}{L/2} \qquad \text{……(B-1)}$$

The diffusivity equations for the matrix and fracture along with the boundary conditions are stated below:

Matrix

$$\frac{\partial^2 p_m}{\partial z^2} = \left(\frac{\phi\mu c_t}{k}\right)_m \frac{\partial p_m}{\partial t} \qquad \text{.....(B-2)}$$

Initial condition: $p_m(z,0) = p_i$

Inner boundary: At $z = 0, \frac{\partial p_m}{\partial z} = 0$ (line of symmetry)

Outer boundary: At $z = \frac{L}{2}, p_m = p_f$

Fractures

$$\frac{\partial^2 p_f}{\partial y^2} = (\frac{\phi\mu c_t}{k})_f \frac{\partial p_f}{\partial t} - \frac{k_m}{k_f \frac{L}{2}} \left|\frac{\partial p_m}{\partial z}\right|_{z=\frac{L}{2}} \qquad \text{.....(B-3)}$$

The additional term on the right-hand side is the source term from the matrix.

Initial condition: $p_f(y,0) = p_i$

Inner boundary: $q = -\frac{k_f A_{cw}}{\mu}\left(\frac{\partial p_f}{\partial y}\right)_{y=0}$ (constant rate)

Outer boundary: At y = $\frac{y_e}{\sqrt{A_{cw}}}$, $\frac{\partial p_f}{\partial y} = 0$ (no-flow boundary)

Converting Eq. B-2 to dimensionless variables with definitions in Eq. B-1

$$\frac{\partial^2 p_{DLm}}{\partial z_D^2} = (1-\omega)\frac{L^2}{4}\frac{k_f}{k_m}\frac{1}{A_{cw}}\frac{\partial p_{DLm}}{\partial t_{DAc}}$$

and

$$\frac{\partial^2 p_{DLm}}{\partial z_D^2} = \frac{3}{\lambda_{Ac}}(1-\omega)\frac{\partial p_{Dm}}{\partial t_{DAc}} \qquad \text{.....(B-4)}$$

where $\lambda_{Ac} = \frac{12}{L^2}\frac{k_m}{k_f}A_{cw}$ is the Warren and Root interporosity flow parameter

The Initial condition in Eq. B-2 becomes in dimensionless variables

$$p_{DLm}(z_D,0)=0 \qquad \text{.....(B-5)}$$

The Inner boundary condition in Eq. B-2 becomes in dimensionless variables

$$\left|\frac{\partial p_{DLm}}{\partial z_D}\right|_{z_D=0}=0 \qquad \text{.....(B-6)}$$

The outer boundary condition in Eqn. B-2 becomes in dimensionless variables

$$\left|p_{DLm}\right|_{z_D=1}=p_{DLf} \qquad \text{.....(B-7)}$$

Transforming Eqs. B-4, B-5, B-6 and B-7 into Laplace space

$$\frac{d^2\overline{p_{DLm}}}{dz_D^2}=\frac{3(1-\omega)}{\lambda_{Ac}}\left[s\,\overline{p_{DLm}}-\overline{p_{DLm}}(z_D,0)\right] \qquad \text{.....(B-8)}$$

initial condition: $\overline{p_{DLm}}(z_D,0)=0$

inner boundary: $\left|\frac{d\,\overline{p_{DLm}}}{dz_D}\right|_{z_D=0}=0$

outer boundary: $\left|\overline{p_{DLm}}\right|_{z_D=1}=\overline{p_{DLf}}$

Applying the initial condition to Eq. B-8 yields

$$\frac{d^2\overline{p_{DLm}}}{dz_D^2}-\frac{3(1-\omega)}{\lambda_{Ac}}s\,\overline{p_{DLm}}=0 \qquad \text{.....(B-9)}$$

the general solution is given by

$$\overline{p_{DLm}}=A\cosh\sqrt{\frac{3(1-\omega)s}{\lambda_{Ac}}}z_D+B\sinh\sqrt{\frac{3(1-\omega)s}{\lambda_{Ac}}}z_D \qquad \text{.....(B-10)}$$

A and B are determined as

$$B=0$$

$$A=\frac{\overline{p_{DLf}}}{\cosh\sqrt{\frac{3(1-\omega)s}{\lambda_{Ac}}}}$$

and Eq. B-10 becomes

$$\overline{p_{DLm}}=\overline{p_{DLf}}\,\frac{\cosh\sqrt{\frac{3(1-\omega)s}{\lambda_{Ac}}}z_D}{\cosh\sqrt{\frac{3(1-\omega)s}{\lambda_{Ac}}}} \qquad \text{.....(B-11)}$$

Converting the equation for the fractures in Eqn. B-3 into dimensionless variables

$$\frac{\partial^2 p_{DLf}}{\partial y_D^2} = \omega \frac{\partial p_{DLf}}{\partial t_{DAc}} - \frac{\lambda_{Ac}}{3} \left| \frac{\partial p_{DLm}}{\partial z_D} \right|_{z_D=1} \qquad \text{.....(B-12)}$$

Initial condition: $p_{DLf}(y_D,0) = 0$

Inner boundary: $\left| \frac{\partial p_{DLf}}{\partial y_D} \right|_{y_D=0} = -2\pi$

Outer boundary: $\frac{\partial p_{DLf}}{\partial y_D}\left({y_e}/{\sqrt{A_c}}, t_{DAc} \right) = 0$

Transforming Eqn. B-12 into Laplace space

$$\frac{d^2 \overline{p_{DLf}}}{dy_D^2} = \omega \left[s\,\overline{p_{DLf}} - \overline{p_{DLf}}(y_D,0) \right] - \frac{\lambda_{Ac}}{3} \left| \frac{d\,\overline{p_{DLm}}}{dz_D} \right|_{z_D=1} \qquad \text{.....(B-13)}$$

Differentiating and substituting Eqn. B-11 into B-13

$$\frac{d^2 \overline{p_{DLf}}}{dy_D^2} = \omega \left[s\,\overline{p_{DLf}} \right] - \frac{\lambda_{Ac}}{3} \left[\overline{p_{DLf}} \sqrt{\frac{3(1-\omega)s}{\lambda_{Ac}}} \tanh \sqrt{\frac{3(1-\omega)s}{\lambda_{Ac}}} \right]$$

$$\frac{d^2 \overline{p_{DLf}}}{dy_D^2} - \overline{p_{DLf}}\, s \left\{ \omega + \overline{p_{DLf}} \sqrt{\frac{\lambda_{Ac}}{3s}(1-\omega)} \tanh \sqrt{\frac{3(1-\omega)s}{\lambda_{Ac}}} \right\} = 0$$

Which can be represented as

$$\frac{d^2 \overline{p_{DLf}}}{dy_D^2} - \overline{p_{DLf}}\, s f(s) = 0 \qquad \text{.....(B-14)}$$

where $f(s) = \omega + \sqrt{\frac{\lambda_{Ac}}{3s}(1-\omega)} \tanh \sqrt{\frac{3(1-\omega)s}{\lambda_{Ac}}}$

Eq. B-12 thus becomes in Laplace space

$$\frac{d^2 \overline{p_{DLf}}}{dy_D^2} - s f(s) \overline{p_{DLf}} = 0 \qquad \text{.....(B-15)}$$

Initial condition: $\overline{p_{DLf}}(y_D,0) = 0$

Inner boundary: $\left| \frac{d\,\overline{p_{DLf}}}{dy_D} \right|_{y_D=0} = -\frac{2\pi}{s}$

Outer boundary: $\frac{d\overline{p_{DLf}}}{dy_D}\left(\frac{y_e}{\sqrt{A_c}}, s\right) = 0$

Thus, the general solution to Eq. B-15 is

$$\overline{p_{DLf}} = A\cosh\left(\sqrt{sf(s)}\,y_D\right) + B\sinh\left(\sqrt{sf(s)}\,y_D\right) \qquad \text{.....(B-16)}$$

A and B are determined as

$$B = \frac{-2\pi}{s\sqrt{sf(s)}} \qquad \text{.....(B-17)}$$

$$A = \frac{2\pi}{s\sqrt{sf(s)}} \frac{\cosh\left(\sqrt{sf(s)}\,y_e \big/ \sqrt{A_c}\right)}{\sinh\left(\sqrt{sf(s)}\,y_e \big/ \sqrt{A_c}\right)}$$

Substituting into Eqn. B-16 yields

$$\overline{p_{DLf}} = \frac{2\pi}{s\sqrt{sf(s)}} \frac{\cosh\left(\sqrt{sf(s)}\,y_e \big/ \sqrt{A_c}\right)}{\sinh\left(\sqrt{sf(s)}\,y_e \big/ \sqrt{A_c}\right)} \cosh\left(\sqrt{sf(s)}\,y_D\right) - \frac{2\pi}{s\sqrt{sf(s)}} \sinh\left(\sqrt{sf(s)}\,y_D\right) \qquad \text{.....(B-18)}$$

Substituting $y_D = 0$ (at the well) into Eq B-18 yields

$$\overline{p_{wDL}} = \frac{2\pi}{s\sqrt{sf(s)}} \frac{\cosh\left(\sqrt{sf(s)}\,y_e \big/ \sqrt{A_c}\right)}{\sinh\left(\sqrt{sf(s)}\,y_e \big/ \sqrt{A_c}\right)} \qquad \text{.....(B-19)}$$

and $$\overline{p_{wDL}} = \frac{2\pi}{s\sqrt{sf(s)}} \frac{e^{\left(\sqrt{sf(s)}\,y_e \big/ \sqrt{A_c}\right)} + e^{\left(-\sqrt{sf(s)}\,y_e \big/ \sqrt{A_c}\right)}}{e^{\left(\sqrt{sf(s)}\,y_e \big/ \sqrt{A_c}\right)} - e^{\left(-\sqrt{sf(s)}\,y_e \big/ \sqrt{A_c}\right)}} \qquad \text{.....(B-20)}$$

$$\overline{p_{wDL}} = \frac{2\pi}{s\sqrt{sf(s)}} \left[\frac{e^{\sqrt{sf(s)}\,y_{De}} + e^{-\sqrt{sf(s)}\,y_{De}}}{e^{\sqrt{sf(s)}\,y_{De}} - e^{-\sqrt{sf(s)}\,y_{De}}}\right] \qquad \text{.....(B-21)}$$

Where $y_{De} = \frac{y_e}{\sqrt{A_{cw}}}$

$$\overline{p_{wDL}} = \frac{2\pi}{s\sqrt{sf(s)}} \left[\frac{e^{\sqrt{sf(s)}\,y_{De}} + \frac{1}{e^{\sqrt{sf(s)}\,y_{De}}}}{e^{\sqrt{sf(s)}\,y_{De}} - \frac{1}{e^{\sqrt{sf(s)}\,y_{De}}}}\right]$$

$$\overline{p_{wDL}} = \frac{2\pi}{s\sqrt{sf(s)}}\left[\frac{e^{2\sqrt{sf(s)}y_{De}}+1}{e^{2\sqrt{sf(s)}y_{De}}-1}\right] \qquad \text{……(B-22)}$$

dividing by $e^{2\sqrt{sf(s)}y_{De}}$

$$\overline{p_{wDL}} = \frac{2\pi}{s\sqrt{sf(s)}}\left[\frac{1+e^{-2\sqrt{sf(s)}y_{De}}}{1-e^{-2\sqrt{sf(s)}y_{De}}}\right] \qquad \text{……(B-23)}$$

In Laplace space, the constant pressure case at the wellbore can be found from the solution for the constant rate case given by Eq. B-23 using Eq. B-24.

$$\overline{q_{DL}} = \frac{1}{s^2\overline{p_{wDL}}} \qquad \text{……(B-24)}$$

Eq. B-23 thus becomes for the constant pressure case

$$\frac{1}{\overline{q_{DL}}} = \frac{2\pi s}{\sqrt{sf(s)}}\left[\frac{1+e^{-2\sqrt{sf(s)}y_{De}}}{1-e^{-2\sqrt{sf(s)}y_{De}}}\right] \qquad \text{……(B-25)}$$

Eq. B-25 can then be inverted to obtain the solutions as a function of time using suitable Laplace numerical inversion algorithms such as Stehfest's inversion algorithm.

APPENDIX C

DEVELOPMENT OF ANALYSIS EQUATIONS

In this section, the analysis equations for the linear model are derived.

C-1 Region 1

This region represents early linear flow in the fracture system only. The Laplace space solution for the constant pressure inner boundary, closed outer boundary reservoir (slab matrix) is given from Eq. B-25 by

$$\frac{1}{\overline{q_{DL}}} = \frac{2\pi s}{\sqrt{sf(s)}}\left[\frac{1+e^{-2\sqrt{sf(s)}y_{De}}}{1-e^{-2\sqrt{sf(s)}y_{De}}}\right] \quad \text{where} \quad y_{De} = y_e \Big/ \sqrt{A_{cw}}$$

This can be shown to be the same as

$$\frac{1}{\overline{q_{DL}}} = \frac{2\pi s}{\sqrt{sf(s)}} Coth\left(\sqrt{sf(s)}\,y_{De}\right) \qquad \text{.....(C-1)}$$

$$\text{using} \quad Coth(x) = \frac{e^{2x}+1}{e^{2x}-1} \qquad \text{.....(C-2)}$$

Approximately for x >3, $Coth(x) \approx 1$

Therefore $Coth\left(\sqrt{sf(s)}y_{De}\right) \approx 1$ when $\sqrt{sf(s)}y_{De} > 3$ .....(C-3)

Eq. C-1 becomes

$$\frac{1}{\overline{q_{DL}}} = \frac{2\pi s}{\sqrt{sf(s)}} \qquad \text{.....(C-4)}$$

For slab matrix, $f(s) = \omega + \sqrt{\frac{\lambda_{Ac}}{3s}(1-\omega)}\tanh\left(\sqrt{\frac{3(1-\omega)s}{\lambda_{Ac}}}\right)$ .....(C-5)

Assume $\omega >>>>> \sqrt{\frac{\lambda_{Ac}}{3s}(1-\omega)}\tanh\left(\sqrt{\frac{3(1-\omega)s}{\lambda_{Ac}}}\right)$ .....(C-6)

Therefore $f(s) = \omega$ .....(C-7)

Eq. C-4 becomes

$$\frac{1}{\overline{q_{DL}}} = \frac{2\pi s}{\sqrt{s}} \frac{1}{\sqrt{\omega}} \qquad \text{……(C-8)}$$

or $$\overline{q_{DL}} = \frac{1}{2\pi\sqrt{s}} \sqrt{\omega} \qquad \text{……(C-9)}$$

Inverting from Laplace space

$$q_{DL} = \frac{1}{2\pi\sqrt{\pi t_{DAc}}} \sqrt{\omega} \qquad \text{……(C-10)}$$

$$q_{DL} = \frac{1}{2\pi\sqrt{\pi t_{DAc}/\omega}} \qquad \text{……(C-11)}$$

From the assumptions in Eqs. C-3 and C-6 we can derive approximate equations for the approximate range where Eq. C-11 is valid

From Eq. C-3, $\sqrt{sf(s)}y_{De} > 3$

Applying Eq. C-7

Thus $\sqrt{s\omega}y_{De} > 3$ ……(C-12)

And $s > \frac{9}{y_{De}^2 \omega}$

Multiplying by $\frac{1}{s^2}$

$$\frac{1}{s} > \frac{1}{s^2} \frac{9}{y_{De}^2 \omega} \qquad \text{……(C-13)}$$

Inverting from Laplace space

$$1 > t_{DAc} \frac{9}{y_{De}^2 \omega} \qquad \text{……(C-14)}$$

And $t_{DAc} < \frac{y_{De}^2 \omega}{9}$ ……(C-15)

From Eq. C-6, $\omega >>>>> \sqrt{\frac{\lambda_{Ac}}{3s}(1-\omega)} \tanh\left(\sqrt{\frac{3(1-\omega)s}{\lambda_{Ac}}}\right)$ implies that

$$\sqrt{\frac{\lambda_{Ac}}{3s}(1-\omega)} \tanh\left(\sqrt{\frac{3(1-\omega)s}{\lambda_{Ac}}}\right) \approx 0 \quad \text{……(C-16)}$$

This implies that s is large (very small times, t_{DAc})

We can thus give an approximate range for Region 1 as

$$0 < t_{DAc} < \frac{y_{De}^2 \omega}{9} \quad \text{……(C-17)}$$

C-2 Region 2

This represents bilinear flow caused by simultaneous depletion in the fracture system and matrix. The Laplace space solution for the constant pressure inner boundary, closed outer boundary reservoir (slab matrix) is given from Eq. B-25 by

$$\frac{1}{\overline{q}_{DL}} = \frac{2\pi s}{\sqrt{sf(s)}}\left[\frac{1+e^{-2\sqrt{sf(s)}y_{De}}}{1-e^{-2\sqrt{sf(s)}y_{De}}}\right] \quad \text{where} \quad y_{De} = y_e \Big/ \sqrt{A_{cw}}$$

From Eq. C-1,

$$\frac{1}{\overline{q}_{DL}} = \frac{2\pi s}{\sqrt{sf(s)}} Coth\left(\sqrt{sf(s)}\, y_{De}\right) \quad \text{……(C-18)}$$

For slab matrix,

$$f(s) = \omega + \sqrt{\frac{\lambda_{Ac}}{3s}(1-\omega)} \tanh\left(\sqrt{\frac{3(1-\omega)s}{\lambda_{Ac}}}\right) \quad \text{……(C-19)}$$

Assume $\omega <<<< \sqrt{\frac{\lambda_{Ac}}{3s}(1-\omega)} \tanh\left(\sqrt{\frac{3(1-\omega)s}{\lambda_{Ac}}}\right)$ ……(C-20)

and $1-\omega \approx 1$

Approximately for For x >3, $Tanh(x) \approx 1$

Assume $\tanh\left(\sqrt{\frac{3(1-\omega)s}{\lambda}}\right) \approx 1$ ……(C-21)

Thus $\sqrt{\frac{3s}{\lambda_{Ac}}} > 3$ ……(C-22)

Therefore Eq. C-19 becomes

$f(s) = \sqrt{\frac{\lambda_{Ac}}{3s}}$ ……(C-23)

Approximately For x>3 $Coth(x) \approx 1$

Therefore In Eq. C-18

$Coth\left(\sqrt{sf(s)}y_{De}\right) \approx 1$ when $\sqrt{sf(s)}y_{De} > 3$ ……(C-24)

And Eq. C-18 becomes

$$\frac{1}{\overline{q_{DL}}} = \frac{2\pi s}{\sqrt{sf(s)}} \quad \text{……(C-25)}$$

Substituting Eq. C-23 in C-25

$$\frac{1}{\overline{q_{DL}}} = 2\pi s\left(\frac{3^{0.25}}{s^{0.25}\lambda_{Ac}^{0.25}}\right) = \frac{(2\pi)\left(3^{0.25}\right)}{\lambda_{Ac}^{0.25}} s^{0.75}$$

and $$\overline{q_{DL}} = \frac{\lambda_{Ac}^{0.25}}{(2\pi)\left(3^{0.25}\right)} \frac{1}{s^{0.75}} \quad \text{……(C-26)}$$

Inverting from Laplace space

$q_{DL} = \frac{\lambda_{Ac}^{0.25}}{(2\pi)\left(3^{0.25}\right)} \frac{t_{DAc}^{-0.25}}{\Gamma(0.75)}$ where Γ( ) is the gamma function.

$$q_{DL} = \frac{\lambda_{Ac}^{0.25}}{(2\pi)\left(3^{0.25}\right)} \frac{t_{DAc}^{-0.25}}{1.22542}$$

$$q_{DL} = \frac{\lambda_{Ac}^{0.25}}{10.13317\ t_{DAc}^{0.25}} \qquad \text{……(C-27)}$$

From the assumptions in Eqs. C-22 and C-24 we can derive approximate equations for the approximate range where Eq. C-26 is valid

From Eq. C-22, $\sqrt{\frac{3s}{\lambda_{Ac}}} > 3$

And $\frac{3s}{\lambda_{Ac}} > 9$ ……(C-28)

Multiplying by $\frac{1}{s^2}$

$$\frac{1}{s}\frac{3}{\lambda_{Ac}} > \frac{1}{s^2}9 \qquad \text{……(C-29)}$$

Inverting from Laplace space

$$\frac{3}{\lambda_{Ac}} > t_{DAc}9 \qquad \text{…….(C-30)}$$

And $t_{DAc} < \frac{1}{3\lambda_{Ac}}$ …….(C-31)

From Eq. C-24, $\sqrt{sf(s)}y_{De} > 3$ …….(C-32)

Applying Eq. C-23 to Eq. C-32

$$\frac{s^{0.25}\lambda_{Ac}^{0.25}}{3^{0.25}} y_{De} > 3 \qquad \text{…….(C-33)}$$

And $s > \left(\frac{3}{y_{De}}\right)^4 \frac{3}{\lambda_{Ac}}$ …….(C-34)

Multiplying by $\frac{1}{s^2}$

$$\frac{1}{s} > \frac{1}{s^2}\left(\frac{3}{y_{De}}\right)^4 \frac{3}{\lambda_{Ac}} \qquad \text{.....(C-35)}$$

Inverting from Laplace space

$$1 > t_{DAc}\left(\frac{3}{y_{De}}\right)^4 \frac{3}{\lambda_{Ac}} \qquad \text{.....(C-36)}$$

And $t_{DAc} < \left(\frac{y_{De}}{3}\right)^4 \frac{\lambda_{Ac}}{3}$

It thus appears that an approximate criteria for Region 2 is

$$t_{DAc} < \frac{1}{3\lambda_{Ac}}$$

and $t_{DAc} < \left(\frac{y_{De}}{3}\right)^4 \frac{\lambda_{Ac}}{3}$ .....(C-37)

C-3 Region 3

This region represents the homogeneous reservoir case. The Laplace space solution for the constant pressure inner boundary, closed outer boundary reservoir (slab matrix) is given from Eq. B-25 by

$$\frac{1}{\overline{q_{DL}}} = \frac{2\pi s}{\sqrt{sf(s)}}\left[\frac{1+e^{-2\sqrt{sf(s)}y_{De}}}{1-e^{-2\sqrt{sf(s)}y_{De}}}\right] \text{ where } y_{De} = y_e \Big/ \sqrt{A_{cw}}$$

From Eq. C-1,

$$\frac{1}{\overline{q_{DL}}} = \frac{2\pi s}{\sqrt{sf(s)}} Coth\left(\sqrt{sf(s)}\, y_{De}\right) \qquad \text{.....(C-38)}$$

Approximately for x >3, $Coth(x) \approx 1$

Therefore $Coth\left(\sqrt{sf(s)}y_{De}\right) \approx 1$ when $\sqrt{sf(s)}y_{De} > 3$ .....(C-39)

Eq. (C-38) becomes

$$\overline{\overline{\frac{1}{q_{DL}}}} = \frac{2\pi s}{\sqrt{sf(s)}} \qquad \text{.....(C-40)}$$

For the homogeneous case , $f(s) = 1$ .....(C-41)

and

$$\overline{\overline{\frac{1}{q_{DLh}}}} = \frac{2\pi s}{\sqrt{sf(s)}}$$

Eq. C-40 becomes

$$\overline{\overline{\frac{1}{q_{DLh}}}} = \frac{2\pi s}{\sqrt{s}} \qquad \text{.....(C-42)}$$

or $$\overline{q_{DLh}} = \frac{1}{2\pi\sqrt{s}} \qquad \text{.....(C-43)}$$

Inverting from Laplace space

$$q_{DLh} = \frac{1}{2\pi\sqrt{\pi t_{DAch}}} \qquad \text{.....(C-44)}$$

Where $\frac{1}{q_{DLh}} = \frac{k\sqrt{A_{cw}}\left[m(p_i) - m(p_{wf})\right]}{1422 q_g T}$; $t_{DAch} = \frac{0.00633kt}{(\phi\mu c_t)A_{cw}}$ and k is the homogeneous reservoir permeability.

From the assumptions in Eqs. C-39 and C-41 we can derive approximate equations for the approximate range where Eq. C-44 is valid

From Eq. C-39, $\sqrt{sf(s)}\,y_{De} > 3$

Applying Eq. C-41

Thus $\sqrt{s}\,y_{De} > 3$ .....(C-45)

And $s > \frac{9}{y_{De}^2}$ .....(C-46)

Multiplying by $\frac{1}{s^2}$

$$\frac{1}{s} > \frac{1}{s^2}\frac{9}{y_{De}^2} \qquad \text{.....(C-47)}$$

Inverting from Laplace space

$$1 > t_{DAc}\frac{9}{y_{De}^2} \qquad \text{.....(C-48)}$$

And $t_{DAc} < \frac{y_{De}^2}{9}$ .....(C-49)

We can thus give an approximate criteria for Region 3 as

$$t_{DAc} < \frac{y_{De}^2}{9} \qquad \text{.....(C-50)}$$

C-4 Region 4

This represents the transient linear case when the transient response is primarily from drainage of the matrix. The Laplace space solution for the constant pressure inner boundary, closed outer boundary reservoir (slab matrix) is given from Eq. B-25 by

$$\frac{1}{\overline{q_{DL}}} = \frac{2\pi s}{\sqrt{sf(s)}}\left[\frac{1+e^{-2\sqrt{sf(s)}y_{De}}}{1-e^{-2\sqrt{sf(s)}y_{De}}}\right] \text{ where } y_{De} = y_e \Big/ \sqrt{A_{cw}}$$

From Eq. C-1,

$$\frac{1}{\overline{q_{DL}}} = \frac{2\pi s}{\sqrt{sf(s)}}Coth\left(\sqrt{sf(s)}\,y_{De}\right) \qquad \text{.....(C-51)}$$

For slab matrix,

$$f(s) = \omega + \sqrt{\frac{\lambda_{Ac}}{3s}(1-\omega)}\tanh\left(\sqrt{\frac{3(1-\omega)s}{\lambda_{Ac}}}\right) \qquad \text{.....(C-52)}$$

Assume $\omega <<<< \sqrt{\frac{\lambda_{Ac}}{3s}(1-\omega)}\tanh\left(\sqrt{\frac{3(1-\omega)s}{\lambda_{Ac}}}\right)$ .....(C-53)

and $1-\omega \approx 1$

Approximately for For x >3, $Tanh(x) \approx 1$

Assume $\tanh\left(\sqrt{\frac{3(1-\omega)s}{\lambda_{Ac}}}\right) \approx 1$ …….(C-54)

Thus $\sqrt{\frac{3s}{\lambda_{Ac}}} > 3$ …….(C-55)

Therefore Eq. C-52 becomes

$f(s) = \sqrt{\frac{\lambda_{Ac}}{3s}}$ …….(C-56)

Taylor's series expansion of

$Coth(x) = \frac{1}{x} + \frac{x}{3} - \frac{x^3}{45} + \frac{2x^5}{945} + ...$ …….(C-57)

Taking first term of series $Coth(x) \approx \frac{1}{x}$ ……..……(C-58)

Thus, In Eq. C-51,

assuming $Coth\left(\sqrt{sf(s)}y_{De}\right) \approx \frac{1}{\sqrt{sf(s)}y_{De}}$ ……..……(C-59)

Eq. C-51 becomes $\frac{1}{\overline{\overline{q_{DL}}}} = \frac{2\pi s}{\sqrt{sf(s)}} \frac{1}{\sqrt{sf(s)}y_{De}}$

and $\frac{1}{\overline{\overline{q_{DL}}}} = \frac{2\pi}{f(s)} \frac{1}{y_{De}}$ ……..……(C-60)

Substituting Eq. C-56 in C-60

$\frac{1}{\overline{\overline{q_{DL}}}} = 2\pi\sqrt{\frac{3s}{\lambda_{Ac}}} \frac{1}{y_{De}} = 2\pi\sqrt{s}\sqrt{\frac{3}{\lambda_{Ac}}} \frac{1}{y_{De}}$

and $\overline{q_{DL}} = \frac{1}{2\pi\sqrt{s}} \sqrt{\frac{\lambda_{Ac}}{3}} y_{De}$

Inverting from Laplace space

$$q_{DL} = \frac{1}{2\pi\sqrt{\pi t_{DAc}}}\sqrt{\frac{\lambda_{Ac}}{3}}y_{De} \qquad \text{……..……(C-61)}$$

From the assumptions in Eqs. C-55 and C-59 we can derive approximate equations for the approximate range where Eq. C-61 is valid

From Eq. C-55, $\sqrt{\frac{3s}{\lambda_{Ac}}} > 3$

And $\frac{3s}{\lambda_{Ac}} > 9$ ……..……(C-62)

Multiplying by $\frac{1}{s^2}$

$\frac{1}{s}\frac{3}{\lambda_{Ac}} > \frac{1}{s^2}9$ ……..……(C-63)

Inverting from Laplace space

$\frac{3}{\lambda_{Ac}} > t_{DAc}9$ ……..……(C-64)

And $t_{DAc} < \frac{1}{3\lambda_{Ac}}$ ……..……(C-65)

From Eq. C-59, $Coth\left(\sqrt{sf(s)}y_{De}\right) \approx \frac{1}{\sqrt{sf(s)}y_{De}}$

Since $Coth(x) \approx \frac{1}{x}$ when approximately x <0.5 ……..……(C-66)

This implies that $\sqrt{sf(s)}y_{De} < 0.5$ ……..……(C-67)

Applying Eq. C-56

$\left(\frac{\lambda_{Ac}s}{3}\right)^{0.25} y_{De} < 0.5$ ……..……(C-68)

And

$s < \frac{3}{\lambda_{Ac}}\left(\frac{0.5}{y_{De}}\right)^4$ ……..……(C-69)

Multiplying by $\frac{1}{s^2}$

$$\frac{1}{s} < \frac{1}{s^2}\frac{3}{\lambda_{Ac}}\left(\frac{0.5}{y_{De}}\right)^4 \qquad \text{……..……(C-70)}$$

Inverting from Laplace space

$$1 < t_{DAc}\frac{3}{\lambda_{Ac}}\left(\frac{0.5}{y_{De}}\right)^4 \qquad \text{……..……(C-71)}$$

$$t_{DAc} > \frac{\lambda_{Ac}}{3}\left(\frac{y_{De}}{0.5}\right)^4 \qquad \text{……..……(C-72)}$$

We can thus give an approximate range from Eq. C-65 and C-72 for Region 4 as

$$\frac{\lambda_{Ac}}{3}\left(\frac{y_{De}}{0.5}\right)^4 < t_{DAc} < \frac{1}{3\lambda_{Ac}} \qquad \text{……..……(C-73)}$$

APPENDIX D

HOMOGENEOUS LINEAR RESERVOIR RESPONSE

In this section, the derivations of the equations for the homogeneous, constant pressure inner boundary, bounded rectangular reservoir are shown. This equation is derived beginning with Eq. B-25 for the linear model.

$$\frac{1}{\overline{q_{DL}}} = \frac{2\pi s}{\sqrt{sf(s)}}\left[\frac{1+e^{-2\sqrt{sf(s)}y_{De}}}{1-e^{-2\sqrt{sf(s)}y_{De}}}\right]$$

As shown in Appendix C, this is the same as

$$\frac{1}{\overline{q_{DL}}} = \frac{2\pi s}{\sqrt{sf(s)}} Coth\left(\sqrt{sf(s)}\,y_{De}\right)$$

For the homogeneous case, *f(s) = 1,* and

$$\frac{1}{\overline{q_{DLh}}} = \frac{2\pi s}{\sqrt{sf(s)}} Coth\left(\sqrt{sf(s)}\,y_{De}\right)$$

thus

$$\frac{1}{\overline{q_{DLh}}} = \frac{2\pi s}{\sqrt{s}} Coth\left(\sqrt{s}\,y_{De}\right) \qquad \text{……..……(D-1)}$$

Or

$$\overline{q_{DLh}} = \frac{\sqrt{s}}{2\pi s} Tanh\left(\sqrt{s}\,y_{De}\right) \qquad \text{……..……(D-2)}$$

$$Tanh(x) = 1 + 2\sum_{n=1}^{\infty}(-1)^n e^{-2nx} \qquad \text{……..……(D-3)}$$

Applying Eq. D-3 to D-2

$$\overline{q_{DLh}} = \frac{\sqrt{s}}{2\pi s}\left[1 - 2e^{-2\sqrt{s}y_{De}} + 2e^{-4\sqrt{s}y_{De}} - 2e^{-6\sqrt{s}y_{De}} + ...\right] \qquad \text{...……..……(D-4)}$$

$$\overline{q_{DLh}} = \frac{1}{2\pi\sqrt{s}}\left[1 - 2e^{-2\sqrt{s}y_{De}} + 2e^{-4\sqrt{s}y_{De}} - 2e^{-6\sqrt{s}y_{De}} + ...\right] \qquad \text{……..……(D-5)}$$

Inverting from Laplace space

$$q_{DLh} = \frac{1}{2\pi\sqrt{\pi t_{DAch}}}\left[1 - 2e^{-\left(y_{De}^2/t_{DAch}\right)} + 2e^{-\left(4y_{De}^2/t_{DAch}\right)} - 2e^{-\left(6y_{De}^2/t_{DAch}\right)} + ...\right] \qquad \text{……...……(D-6)}$$

$$q_{DLh} = \frac{1}{2\pi\sqrt{\pi t_{DAch}}}\left[1 + 2\sum_{n=1}^{\infty}(-1)^n e^{-\left(n^2 y_{De}^2/t_{DAch}\right)}\right] \qquad \text{……..……(D-7)}$$

Eq. D-7 is the exact analytical solution for Eq. B-25 for the homogeneous case.

APPENDIX E

EFFECT OF SKIN

Skin is normally defined as a dimensionless pressure for the slightly compressible fluid case given by[71]

$$s_{rw} = \frac{kh\Delta p_s}{141.2qB\mu} \qquad \text{……..(E-1)}$$

Where the skin is an additional dimensionless pressure

$$p_{wD} = p_D + s_{rw} \qquad \text{……..(E-2)}$$

There have been different definitions for the dimensionless pressure used in pressure transient horizontal wells. One set of investigators[42,48,54,55] define

$$p_{Drw} = \frac{kh\Delta p}{141.2qB\mu} \qquad \text{……..(E-3)}$$

While Kuchuk[50] and Lichtenberger[60] define

$$p_{DH} = \frac{kL_w\Delta p}{141.2qB\mu} \quad \text{and thus} \quad s_H = \frac{kL_w\Delta p_s}{141.2qB\mu} \qquad \text{……..(E-4)}$$

For the linear model we will define

$2\pi s_{Ac} = \dfrac{k\sqrt{A_{cw}}\Delta p_s}{141.2qB\mu}$ which represents the skin defined in El-Banbi[16].

In this section, an investigation will be conducted using different software to determine how their skin is defined or represented. The test model is the constant rate, horizontal well, homogeneous rectangular bounded reservoir case. The software to be

used in this exercise are *Kappa Ecrin v4.02.02 (Saphir module), Fekete (WellTest32 Module version 7.0.0.2)* and the numerical simulator *ECLIPSE version 2007.1*. The results will be compared with our linear model given in Appendix B (homogeneous case, $f(s) = 1$). The dataset is given in Table E-1. Two cases will be presented. Case 1 is one in which skin = zero and Case 2 is one in which skin =10. Skin = 0 and Skin = 10 means that 0 and 10 will be input into each software for the required case.

Table E-1 – Dataset for Effect of Skin Runs.	
r_w	0.25 ft
h	30 ft
ϕ	0.1
k	1 md
p_i	5,000 psi
L_w (x_e)	2,000 ft
y_e	500 ft
q	100 stb/d
B	1 rb/stb
μ	1 cp
c_t	3×10^{-6} psi^{-1}

The results from Case 1 are shown in Figs. E-1 and E-2. Fig. E-1 shows the results plotted in terms of normal variables, log-log plot of $[p_i - p_{wf}]/q$ against time. It can

be observed from Fig. E-1 that the results from the three software show similar results except for Saphir which deviates at later times. Our linear model differs as expected from the three software by the convergence skin expected with an actual horizontal well.

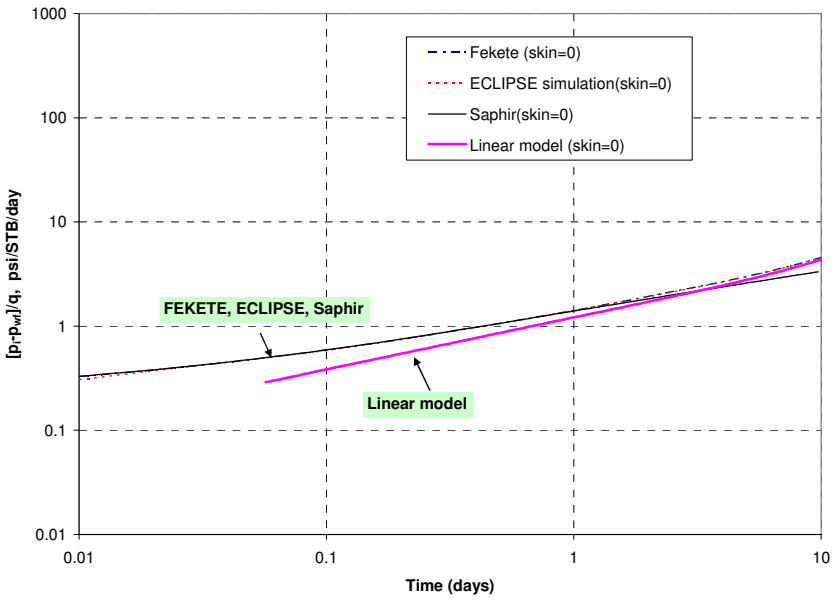

Fig. E-1 – Case 1 (skin = 0) - Comparison of Results. The three software show similar results except for Saphir which deviates at later times. Our linear model differs as expected from the three software by the convergence skin expected with an actual horizontal well.

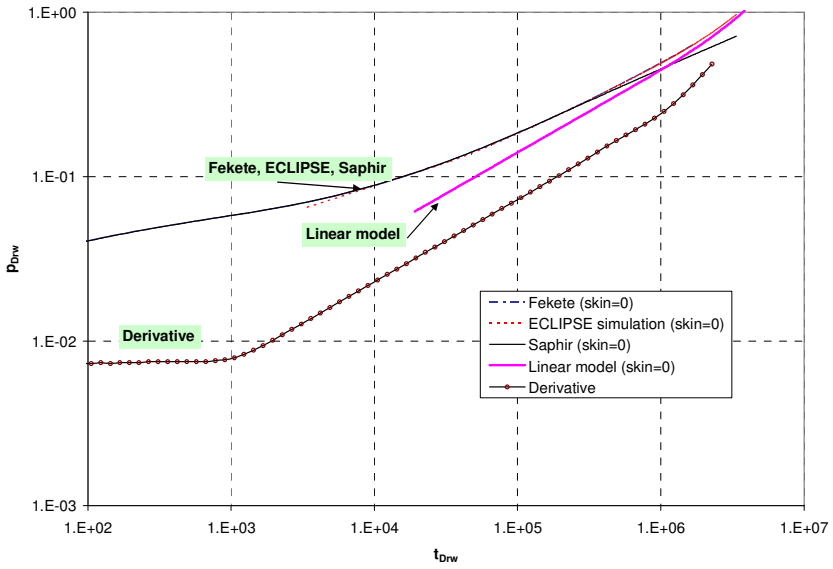

Fig. E-2 – Case 1 (skin = 0) - Comparison of Results (Dimensionless Pressure against Dimensionless Time). The three software show similar results except for Saphir which deviates at later times. Our linear model differs as expected from the three software by the convergence skin expected with an actual horizontal well.

The generated pressure and time results for *Fekete*, *ECLIPSE* from Fig. E-1 are converted to p_{Drw} using Eq. E-3 and t_{Drw} using Eq. E-5 and are plotted in Fig. E-2. Fig. E-2 shows the results plotted as a dimensionless plot of pressure, p_{Drw} against dimensionless time, t_{Drw}. The derivative is also added to the plot.

$$t_{Drw} = \frac{0.00633kt}{\phi\mu c_t r_w^2} \qquad \text{.....(E-5)}$$

The results from the linear model are converted to the above variables p_{Drw} and t_{Drw} using the relations

$$p_{Drw} = p_{DL}\left(\frac{h}{\sqrt{A_{cw}}}\right) \quad \text{and} \quad t_{Drw} = t_{DAc}\left(\frac{r_w^2}{A_{cw}}\right) \qquad \text{.....(E-6)}$$

Fig. E-2 shows the same results as Fig. E-1. The three software show similar results except for Saphir which deviates at later times (Saphir's horizontal well model

might be different from the others). Our linear model as expected indicates linear flow (half-slope on derivative). Our linear model also differs as expected from the three software by the convergence skin expected with an actual horizontal well. The effect of convergence skin has been discussed in Chapter III.

The results from Case 2 (skin = 10) are shown in Figs. E-3 and E-4. Fig. E-3 shows the results plotted in terms of normal variables as a log-log plot of $[p_i-p_{wf}]/q$ against time. It can be observed from Fig. E-3 that the results from *ECLIPSE* and *Fekete* are similar. The results from Saphir differ from the others indicating that the skin definition is different. The linear model obviously also differs from the other results due to its different skin definition. Fig. E-4 shows the corresponding dimensionless pressure and time plot similar to Fig. E-3 except that the skin=10 runs are also added to the plot. The results are summarized in Table E-2.

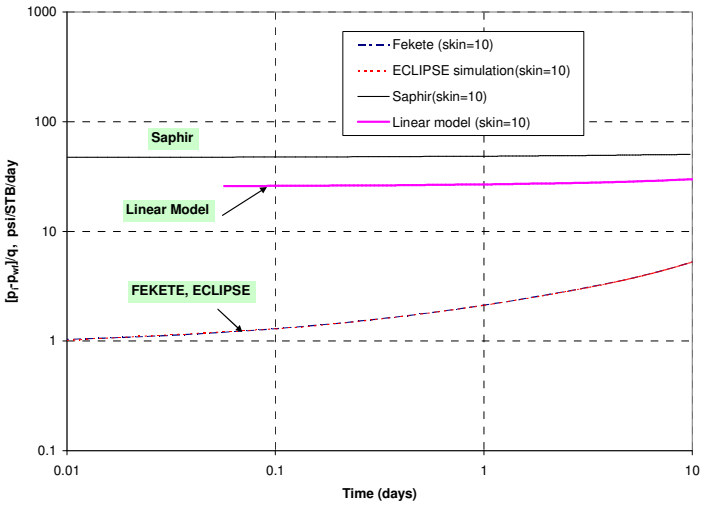

Fig. E-3 – Case 2 (skin = 10) - Comparison of Results. ECLIPSE and Fekete are similar while Saphir and the Linear model are different because of the different skin definitions.

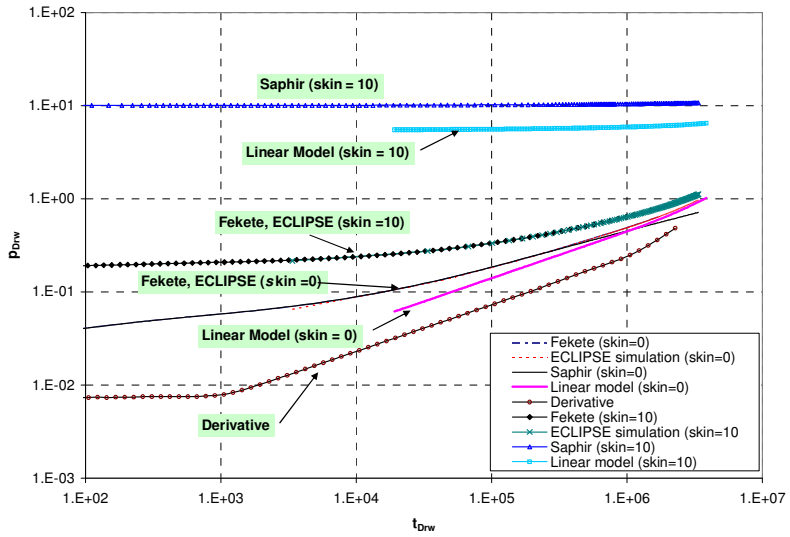

Fig. E-4 – Comparison of Results (skin = 0 and skin =10) Dimensionless Pressure against Dimensionless Time. Fekete and ECLIPSE have similar definitions of skin different from the other software

Table E-2 – Summary of Results from Fig. E-4.	
Software	**Skin *:* $p_{Drw(skin=10)} - p_{Drw(skin=0)}$**
Fekete	0.15
ECLIPSE simulator	0.15
Saphir	10
Linear model	5.44

It can be observed from Table E-2 that the Fekete definition is based on L_w as shown in Eq. E-4. The conversion to conventional definitions results in

$$s_H = 10\frac{h}{L_w} = 10\frac{30}{2{,}000} = 0.15$$

The Saphir definition is obviously based on h. The linear model definition as was previously shown is based on $\sqrt{A_{cw}}$.

$$2\pi s_{Ac} = (2\pi)(10)\frac{h}{\sqrt{A_{cw}}} = (2\pi)(10)\frac{30}{\sqrt{120{,}000}} = 5.44$$

When utilizing the different software these different skin definitions should be noted so as to ensure that accurate interpretation and calculations.

The results from Fekete are plotted on a $[m(p_i)-m(p_{wf})]/q$ against $t^{0.5}$ plot in Fig. E-5. It can be observed from Fig E-5 that there are two parallel lines representing the response in the transient linear region for the skin = 0 and skin = 10 cases. It can thus be concluded that the effect of skin is a constant offset on this plot.

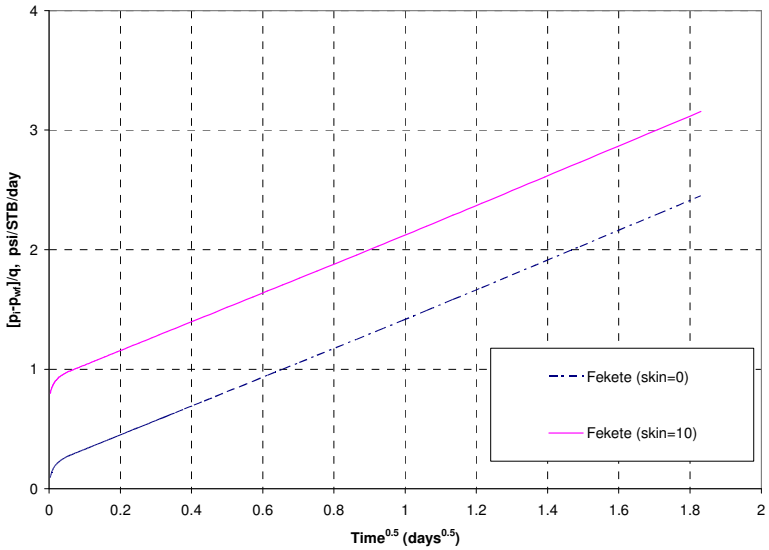

Fig. E-5 – Comparison of Results (skin=0 and skin=10) - Specialized Plot of $[m(p_i)-m(p_{wf})]/q$ against $t^{0.5}$. The two plots are parallel with a constant offset showing the effect of skin. The initial curve is due to the horizontal well radial flow present in the Fekete model.

An equation[60] for computing the convergence skin in the linear flow period which account for additional pressure drop caused by linear flow streamlines converging to an actual horizontal well is given by

$$s_c = \ln\left[\frac{\pi r_w}{h}\left(1+\sqrt{\frac{k_V}{k_H}}\right)\sin\left(\frac{\pi d_z}{h}\right)\right] \qquad \text{.....(E-7)}$$

This equation should be added to the response from our linear model to obtain similar results as in Fekete and ECLIPSE as demonstrated in Chapter III.

E.1 Constant p_{wf} Case

In this section, an investigation will be conducted using the constant p_{wf}, horizontal well, homogeneous rectangular bounded reservoir case. Only *ECLIPSE* and the linear model will be used for this test. The data set is the same as given in Table E-1 except that a well flowing pressure of 250 psi is used. The results for ECLIPSE are shown in Figs. E-6 and E-7. The results for the linear model is shown in Fig. E-8 and E-9. It can be observed from Figs. E-6 and E-8 that the effect of the skin is to lower the rates in the transient linear region. This is contrary to observations with the constant rate case. It can be observed from Figs. E-7 and E-9 that the effect of the skin decreases with increasing time. This is contrary to the parallel lines observed in Fig. E-5 for the constant rate case.

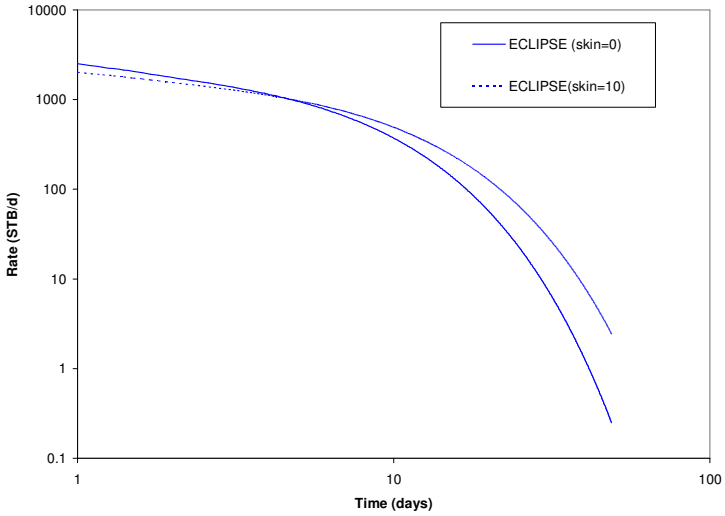

Fig. E-6 – Comparison of Results for ECLIPSE (skin =0 and 10, Constant Pressure case) – Log-log Plot of Rate against Time. The skin = 10 case shows lower rates.

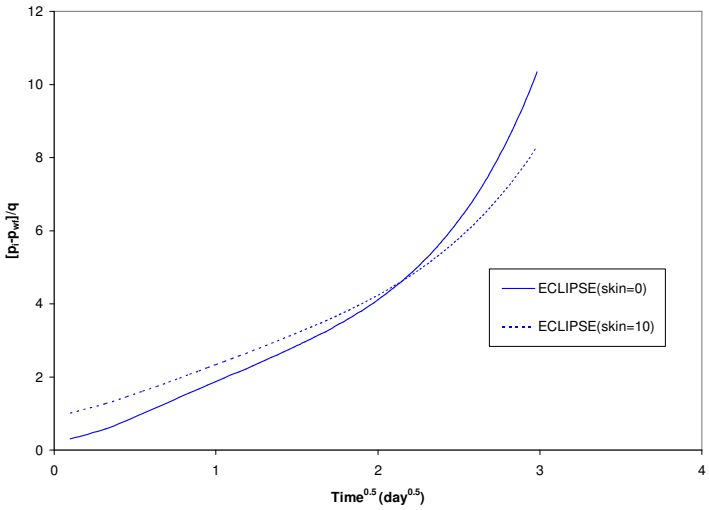

Fig. E-7 – Comparison of Results for ECLIPSE (skin =0 and 10, Constant Pressure case) – Specialized Plot of $[p_i-p_{wf}]/q_g$ against $t^{0.5}$. There is a diminishing effect of skin with time.

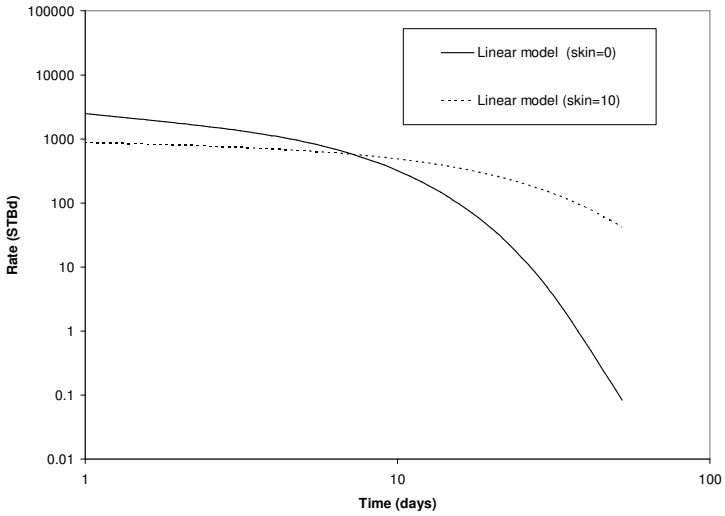

Fig. E-8 – Comparison of Results for the Linear Model (skin =0 and 10, Constant p_{wf} case) – Log-log Plot of Rate against Time. The skin = 10 case shows lower rates.

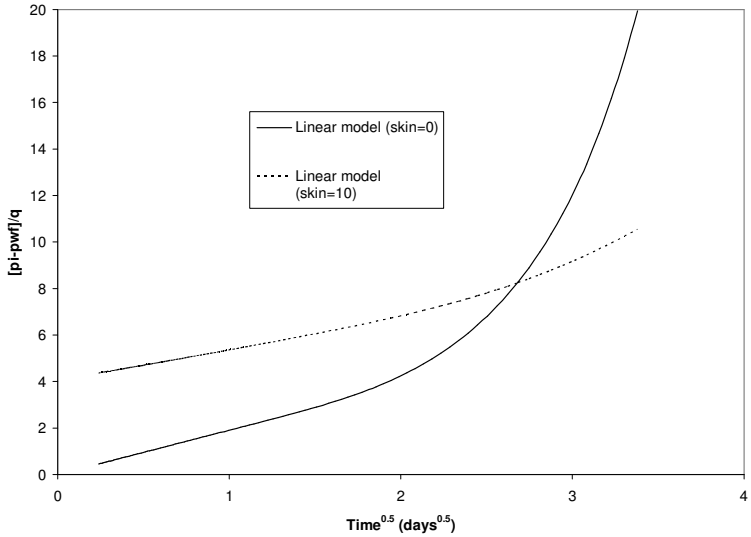

Fig. E-9 – Comparison of Results for the Linear Model (skin =0 and 10, Constant p_{wf} case) – Specialized Plot of $[p_i-p_{wf}]/q_g$ against $t^{0.5}$. There is a diminishing effect of skin with time.

APPENDIX F

DERIVATION OF THE EQUATION FOR THE CONSTANT BOTTOMHOLE PRESSURE EFFECT OF SKIN (HOMOGENEOUS, LINEAR RESERVOIR)

In this section, the constant pressure effect of skin shown previously in Appendix D will be derived for the infinite, homogeneous linear reservoir case.

The equation[16] for the linear model (infinite reservoir case) is given by

$$\frac{1}{\overline{q_{DL}}} = \frac{2\pi s}{\sqrt{sf(s)}}\left[1 + s_{Ac}\sqrt{sf(s)}\right] \qquad \text{……..(F-1)}$$

For the homogeneous reservoir case, $f(s)=1$

Thus

$$\frac{1}{\overline{q_{DLh}}} = \frac{2\pi s}{\sqrt{s}}\left[1 + s_{Ach}\sqrt{s}\right] \qquad \text{……..(F-2)}$$

$$\overline{q_{DLh}} = \frac{1}{2\pi\sqrt{s}\left[1 + s_{Ach}\sqrt{s}\right]} \qquad \text{……..(F-3)}$$

and solving by partial fractions

$$\frac{1}{2\pi\sqrt{s}\left[1 + s_{Ach}\sqrt{s}\right]} = \frac{A}{2\pi\sqrt{s}} + \frac{B}{1 + s_{Ach}\sqrt{s}} \qquad \text{……..(F-4)}$$

$$1 = A\left(1 + s_{Ach}\sqrt{s}\right) + B2\pi\sqrt{s} \qquad \text{……..(F-5)}$$

put $\sqrt{s} = 0$ into Eq. F-4 and thus *A=1*

put $\sqrt{s} = \frac{-1}{s_{Ach}}$ into Eq. F-4 and thus B = $\frac{-s_{Ach}}{2\pi}$

and thus Eq. F-3 can be expressed as

$$\overline{q_{DLh}} = \frac{1}{2\pi\sqrt{s}} + \frac{-s_{Ach}/2\pi}{1+s_{Ac}\sqrt{s}} \qquad \text{.....(F-6)}$$

$$q_{DLh} = \ell^{-1}\left[\frac{1}{2\pi\sqrt{s}}\right] + \ell^{-1}\left[\frac{-s_{Ach}/2\pi}{1+s_{Ac}\sqrt{s}}\right] \qquad \text{.....(F-7)}$$

$$q_{DLh} = \ell^{-1}\left[\frac{1}{2\pi\sqrt{s}}\right] + \frac{-1}{2\pi}\ell^{-1}\left[\frac{1}{1/s_{Ach}+\sqrt{s}}\right] \qquad \text{.....(F-8)}$$

$$q_{DLh} = \frac{1}{2\pi\sqrt{\pi t_{DACh}}} - \frac{1}{2\pi}\left[\frac{1}{\sqrt{\pi t_{DACh}}} - \frac{1}{s_{Ach}} e^{\left(1/s_{Ach}^2\, t_{DAch}\right)} erfc\left(\frac{1}{s_{Ach}}\sqrt{t_{DAch}}\right)\right] \qquad \text{.....(F-9)}$$

$$q_{DLh} = \frac{1}{2\pi s_{Ach}} e^{\left(1/s_{Ach}^2\, t_{DAch}\right)} erfc\left(\frac{1}{s_{Ach}}\sqrt{t_{DAch}}\right) \qquad \text{.....(F-10)}$$

Eq. F-10 gives the transient response for an infinite homogeneous, constant pressure inner boundary reservoir with a skin effect, s_{Ach} present.

It can be observed from Eq. F-10 that at small times, $t_{DAc} \approx 0$

$$q_{DLh} = \frac{1}{2\pi s_{Ach}} \qquad \text{.....(F-11)}$$

And at large times $t_{DAc} \approx \infty$

Using first term of asymptotic expansion for erfc(x) for large x

$$Erfc(x) = \frac{e^{-x^2}}{x\sqrt{\pi}}$$

Eq. F-10 becomes

$$q_{DLh} = \frac{1}{2\pi s_{Ach}} e^{\left(1/s_{Ach}^2 \; t_{DAch}\right)} \frac{e^{-\left(1/s_{Ach}^2 \; t_{DAch}\right)}}{1/s_{Ach} \sqrt{t_{DAch}} \sqrt{\pi}} \qquad \text{……..(F-12)}$$

$$q_{DLh} = \frac{1}{2\pi \sqrt{\pi t_{DACh}}} \qquad \text{……..(F-13)}$$

APPENDIX G

DERIVATION OF THE EQUATION FOR THE SQUARE ROOT OF TIME LINEAR DERIVATIVE (HOMOGENEOUS, LINEAR RESERVOIR, CONSTANT BOTTOMHOLE PRESSURE)

In this section, the analytical equation for linear derivative for the linear homogeneous reservoir (constant pressure inner boundary, infinite) with a skin effect will be derived.

From Eq. F-10,

$$q_{DLh} = \frac{1}{2\pi s_{Ach}} e^{\left(1/s_{Ach}^2\, t_{DAch}\right)} erfc\left(\frac{1}{s_{Ach}}\sqrt{t_{DAch}}\right) \qquad \text{……..(G-1)}$$

We know that

$$\frac{d\left(1/q_{DLh}\right)}{dt_{DAch}} = -\frac{1}{q_{DLh}^2}\frac{dq_{DLh}}{dt_{DAch}}$$

and

$$\frac{d\left(1/q_{DLh}\right)}{d\sqrt{t_{DAch}}} = 2\sqrt{t_{DAch}}\left(-\frac{1}{q_{DLh}^2}\right)\left(\frac{dq_{DLh}}{dt_{DAch}}\right) \qquad \text{……..(G-2)}$$

Let $u = \frac{1}{s_{Ach}}\sqrt{t_{DAch}}$ and thus $u^2 = \frac{1}{s_{Ach}^2} t_{DAch}$

Thus Eq. G-1 becomes

$$q_{DLh} = \frac{1}{2\pi s_{Ach}} e^{u^2} erfc(u) \qquad \text{……..(G-3)}$$

Differentiating

$$\frac{dq_{DLh}}{dt_{DAch}} = \frac{1}{2\pi s_{Ach}} e^{u^2} \frac{d}{dt_{DAch}}[erfc(u)] + erfc(u) \frac{d}{dt_{DAch}}\left[\frac{1}{2\pi s_{Ach}} e^{u^2}\right] \quad \text{……..(G-4)}$$

We know that $\frac{d}{dx} erfc(x) = -\frac{2}{\sqrt{\pi}} e^{-x^2}$

Thus $\frac{d}{du} erfc(u) = -\frac{2}{\sqrt{\pi}} e^{-u^2}$

And $\frac{d}{dt_{DAch}} = \frac{d}{du}\frac{du}{dt_{DAch}}$

Thus $\frac{d}{dt_{DAch}}[erfc(u)] = \frac{d}{du}\frac{du}{dt_{DAch}}[erfc(u)] = -\frac{2e^{-u^2}}{\sqrt{\pi}} \frac{1}{s_{Ach}} \frac{1}{2\sqrt{t_{DAch}}}$

Eq. G-4 becomes

$$\frac{dq_{DLh}}{dt_{DAch}} = \frac{1}{2\pi s_{Ach}} e^{u^2}\left(-\frac{2e^{-u^2}}{\sqrt{\pi}} \frac{1}{s_{Ach}} \frac{1}{2\sqrt{t_{DAch}}}\right) + erfc(u)\left(\frac{1}{2\pi s_{Ach}^3} e^{u^2}\right)$$

……..(G-5)

Applying Eq. G-2 to obtain the square root of time derivative

$$\frac{d\left(1/q_{DLh}\right)}{d\sqrt{t_{DAch}}} = 2\sqrt{t_{DAch}}\left(-\frac{1}{q_{DLh}^2}\right)\left[\frac{1}{2\pi s_{Ach}} e^{u^2}\left(-\frac{2e^{-u^2}}{\sqrt{\pi}} \frac{1}{s_{Ach}} \frac{1}{2\sqrt{t_{DAch}}}\right) + erfc(u)\left(\frac{1}{2\pi s_{Ach}^3} e^{u^2}\right)\right]$$

……..(G-6)

$$\frac{d\left(1/q_{DLh}\right)}{d\sqrt{t_{DAch}}} = \frac{1}{q_{DLh}^2 s_{Ach}^2 \pi^{1.5}} - \sqrt{t_{DAch}} \frac{1}{q_{DLh}^2 \pi s_{Ach}^3} e^{\left(1/s_{Ach}^2 t_{DAch}\right)} erfc\left(\frac{1}{s_{Ach}}\sqrt{t_{DAch}}\right)$$

……..(G-7)

At zero time Eq. G-7 becomes

$$\frac{d\left(1/q_{DLh}\right)}{d\sqrt{t_{DAch}}} = \frac{1}{q_{DLh}^2 s_{Ach}^2 \pi^{1.5}} \qquad \text{……..(G-8)}$$

from Eq. F-10 that at small times, $t_{DAc} \approx 0$

$$q_{DLh} = \frac{1}{2\pi s_{Ach}} \qquad \text{……..(G-9)}$$

The ratio of the slopes at zero time and late time is given by

$$\frac{1/\left(q_{DLh}^2 s_{Ach}^2 \pi^{1.5}\right)}{2\pi\sqrt{\pi}} \qquad \text{……..(G-10)}$$

Substituting Eq. G-9 in Eq. G-10

$$\frac{1/\left[\left(1/2\pi s_{Ach}\right)^2 s_{Ach}^2 \pi^{1.5}\right]}{2\pi\sqrt{\pi}}$$

Which yields

$$\frac{4\pi^2}{\pi^{1.5} 2\pi\sqrt{\pi}} = \frac{2}{\pi} \qquad \text{……..(G-11)}$$

The ratio of the slopes at zero time and late time is given by $\frac{2}{\pi}$

APPENDIX H

DERIVATION OF THE EQUATION FOR THE CONSTANT BOTTOMHOLE PRESSURE EFFECT OF SKIN (SLAB MATRIX, LINEAR RESERVOIR)

In this section, the equation for the linear dual porosity reservoir (slab matrix, constant pressure inner boundary, closed) with a skin effect will be derived.

The constant rate solution (zero skin) is given by Eq. B-23 in Appendix B as

$$\overline{p_{wDL}} = \frac{2\pi}{s\sqrt{sf(s)}}\left[\frac{1+e^{-2\sqrt{sf(s)}y_{De}}}{1-e^{-2\sqrt{sf(s)}y_{De}}}\right] \qquad \text{.....(H-1)}$$

This was shown in Appendix B to be the same as

$$\overline{p_{wDL}} = \frac{2\pi}{s\sqrt{sf(s)}}Coth\left(\sqrt{sf(s)}\,y_{De}\right) \qquad \text{.....(H-2)}$$

using $Coth(x) = \dfrac{e^{2x}+1}{e^{2x}-1}$

the addition of skin to Eq. H-2 in Laplace space is given by

$$\overline{p_{wDL}} = \frac{2\pi}{s\sqrt{sf(s)}}Coth\left(\sqrt{sf(s)}\,y_{De}\right) + \frac{2\pi s_{Ac}}{s} \qquad \text{.....(H-3)}$$

$$\overline{p_{wDL}} = \frac{2\pi Coth\left(\sqrt{sf(s)}\,y_{De}\right) + 2\pi s_{Ac}\sqrt{sf(s)}}{s\sqrt{sf(s)}} \qquad \text{.....(H-4)}$$

The solution for the constant pressure is obtained by applying the Van Everdingen and Hurst relation[59] given by Eq. H-5 to Eq. H-4.

$$\overline{q_{DL}} = \frac{1}{s^2\overline{p_{wDL}}} \qquad \text{.....(H-5)}$$

This results in

$$\frac{1}{\overline{\overline{q_{DL}}}} = \frac{2\pi s Coth\left(\sqrt{sf(s)}\, y_{De}\right) + 2\pi s s_{Ac}\sqrt{sf(s)}}{\sqrt{sf(s)}} \qquad \text{……(H-6)}$$

Taylor's series expansion of

$$Coth(x) = \frac{1}{x} + \frac{x}{3} - \frac{x^3}{45} + \frac{2x^5}{945} + ... \qquad \text{…….(H-7)}$$

Taking first two terms of the series

$$Coth(x) \approx \frac{1}{x} + \frac{x}{3} \qquad \text{……..……(H-8)}$$

Thus, In Eq. H-6,

$$Coth\left(\sqrt{sf(s)}\, y_{De}\right) \approx \frac{1}{\sqrt{sf(s)}\, y_{De}} + \frac{\sqrt{sf(s)}\, y_{De}}{3} \qquad \text{……..……(H-9)}$$

Eq. H-6 becomes

$$\frac{1}{\overline{\overline{q_{DL}}}} = \frac{2\pi s\left[\frac{1}{\sqrt{sf(s)}\, y_{De}} + \frac{\sqrt{sf(s)}\, y_{De}}{3}\right] + 2\pi s s_{Ac}\sqrt{sf(s)}}{\sqrt{sf(s)}} \qquad \text{……..……(H-10)}$$

This yields

$$\frac{1}{\overline{\overline{q_{DL}}}} = \frac{2\pi s(3) + 2\pi s\left(sf(s) y_{De}^2\right) + 2\pi s\left(s_{Ac} sf(s) 3 y_{De}\right)}{3sf(s) y_{De}} \qquad \text{……..……(H-11)}$$

And thus

$$\overline{q_{DL}} = \frac{3sf(s) y_{De}}{2\pi s(3) + 2\pi s\left(sf(s) y_{De}^2\right) + 2\pi s\left(s_{Ac} sf(s) 3 y_{De}\right)} \qquad \text{……..……(H-12)}$$

For slab matrix,

$$f(s) = \omega + \sqrt{\frac{\lambda_{Ac}}{3s}(1-\omega)}\tanh\left(\sqrt{\frac{3(1-\omega)s}{\lambda_{Ac}}}\right) \qquad \text{……..……(H-13)}$$

Assume $\omega <<<< \sqrt{\frac{\lambda_{Ac}}{3s}(1-\omega)}\tanh\left(\sqrt{\frac{3(1-\omega)s}{\lambda_{Ac}}}\right)$ ……..……(H-14)

and $1-\omega \approx 1$

Approximately for For x >3, $Tanh(x) \approx 1$

Assume $\tanh\left(\sqrt{\frac{3(1-\omega)s}{\lambda}}\right) \approx 1$ ……(H-15)

Therefore Eq. H-13 becomes

$f(s) = \sqrt{\frac{\lambda_{Ac}}{3s}}$ ……..……(H-16)

Substituting Eq. H-16 in G-12

$$\overline{q_{DL}} = \frac{3\sqrt{\frac{\lambda_{Ac}s}{3}}y_{De}}{2\pi s(3) + 2\pi s\left(\sqrt{\frac{\lambda_{Ac}s}{3}}y_{De}^2\right) + 2\pi s\left(s_{Ac}\sqrt{\frac{\lambda_{Ac}s}{3}}3y_{De}\right)}$$ ……..……(H-17)

$$\overline{q_{DL}} = 3y_{De}\sqrt{\frac{\lambda_{Ac}}{3}}\frac{\sqrt{s}}{2\pi s\left[3+\sqrt{\frac{\lambda_{Ac}s}{3}}y_{De}^2 + s_{Ac}\sqrt{\frac{\lambda_{Ac}s}{3}}3y_{De}\right]}$$ ……..……(H-18)

$$\overline{q_{DL}} = 3y_{De}\sqrt{\frac{\lambda_{Ac}}{3}}\frac{1}{2\pi\sqrt{s}\left[3+\sqrt{\frac{\lambda_{Ac}s}{3}}y_{De}^2 + s_{Ac}\sqrt{\frac{\lambda_{Ac}s}{3}}3y_{De}\right]}$$ ……..……(H-19)

$$\overline{q_{DL}} = 3y_{De}\sqrt{\frac{\lambda_{Ac}}{3}}\frac{1}{2\pi\sqrt{s}\left[3+\sqrt{s}\left(\sqrt{\frac{\lambda_{Ac}}{3}}y_{De}^2 + s_{Ac}\sqrt{\frac{\lambda_{Ac}}{3}}3y_{De}\right)\right]}$$ ……..……(H-20)

or

$$\overline{q_{DL}} = 3y_{De}\sqrt{\frac{\lambda_{Ac}}{3}}\frac{1}{2\pi\sqrt{s}A\left[\frac{3}{A}+\sqrt{s}\right]} \qquad \text{……..……(H-21)}$$

Where $A = \sqrt{\frac{\lambda_{Ac}}{3}}y_{De}^2 + s_{Ac}\sqrt{\frac{\lambda_{Ac}}{3}}3y_{De}$

Inverting Eq. H-21 from Laplace space

$$q_{DL} = \frac{1}{2\pi}y_{De}\sqrt{\frac{\lambda_{Ac}}{3}}\frac{3}{A}\left[e^{\left(3/A\right)^2 t_{DAc}}erfc\left(\frac{3}{A}\sqrt{t_{DAc}}\right)\right] \qquad \text{……..……(H-22)}$$

It can also be shown as in Appendix F that at small times, $t_{DAc} \approx 0$ Eq. H-22 becomes

$$q_{DL} = \frac{1}{2\pi}\left(\frac{3}{y_{De}+3s_{Ac}}\right) \qquad \text{……..……(H-23)}$$

Which yields similar results as Eq. F-11 as described in Chapter VII.

And at large times, $t_{DAc} \approx \infty$

Using first term of asymptotic expansion for erfc(x) for large x

$$Erfc(x) = \frac{e^{-x^2}}{x\sqrt{\pi}}$$

Eq. H-22 becomes

$$q_{DL} = \frac{1}{2\pi}y_{De}\sqrt{\frac{\lambda_{Ac}}{3}}\frac{3}{A}e^{\left(\left(\frac{3}{A}\right)^2 t_{DAc}\right)}\frac{e^{-\left(\left(\frac{3}{A}\right)^2 t_{DAc}\right)}}{3/A\sqrt{t_{DAc}}\sqrt{\pi}} \qquad \text{……..(H-24)}$$

$$q_{DL} = \frac{1}{2\pi\sqrt{\pi t_{DAC}}}\sqrt{\frac{\lambda_{Ac}}{3}}y_{De} \qquad \text{……..(H-25)}$$

Which is the expected equation for Region 4 previously given in Eq. C-65.

APPENDIX I

DERIVATION OF EQUATIONS FOR THE BEGINNING OF CONVERGENCE SKIN STABILIZATION IN LINEAR FLOW

As previously discussed, convergence skin accounts for distortion of the linear flow in the rectangular reservoir to radial flow around the wellbore. The convergence skin develops during radial flow and stabilizes throughout linear flow. In this section equations will be derived for the beginning of this stabilization for both constant rate and constant p_{wf} cases.

I-1 Constant Rate

The equation for the radial flow in a horizontal well is given by

$$p_{DH} = \frac{1}{2}\ln t_{Drw} + 0.4045 \qquad \text{.....(I-1)}$$

Eq. I-1 can also be expressed as

$$\frac{kL_w\Delta p}{141.2qB\mu} = \frac{1}{2}\ln\left(\frac{0.00633kt}{\phi\mu c_t r_w^2}\right) + 0.4045 \qquad \text{.....(I-2)}$$

The equation for linear flow is given by

$$p_{DL} = 4\sqrt{\pi t_{DAc}} + s_c \qquad \text{.....(I-3)}$$

where s_c is the convergence skin

Eq. I-3 can also be expressed as

$$\frac{k\sqrt{A_{cw}}\Delta p}{141.2qB\mu} = 4\sqrt{\pi\left(\frac{0.00633kt}{\phi\mu c_t A_{cw}}\right)} + s_c \qquad \text{……..(I-4)}$$

From Eq. I-2,

$$\frac{k\Delta p}{141.2qB\mu} = \frac{1}{L_w}\left\{\frac{1}{2}\ln\left(\frac{0.00633kt}{\phi\mu c_t r_w^2}\right) + 0.4045\right\} \qquad \text{……..(I-5)}$$

Differentiating Eq. I-5

$$\frac{d\left(\frac{k\Delta p}{141.2qB\mu}\right)}{dt} = \frac{1}{L_w}\left(\frac{1}{2t}\right) \qquad \text{……..(I-6)}$$

From Eq. I-4,

$$\frac{k\Delta p}{141.2qB\mu} = \frac{1}{\sqrt{A_{cw}}}\left\{4\sqrt{\pi\left(\frac{0.00633kt}{\phi\mu c_t A_{cw}}\right)} + s_c\right\} \qquad \text{……..(I-7)}$$

Differentiating Eq. I-7

$$\frac{d\left(\frac{k\Delta p}{141.2qB\mu}\right)}{dt} = \frac{1}{\sqrt{A_{cw}}}4\sqrt{\pi\left(\frac{0.00633k}{\phi\mu c_t A_{cw}}\right)}\frac{1}{2\sqrt{t}} \qquad \text{……..(I-8)}$$

Equate Eqs. I-6 and I-8

$$\frac{1}{2tL_w} = \frac{4}{A_{cw}}\sqrt{\pi\left(\frac{0.00633k}{\phi\mu c_t}\right)}\frac{1}{2\sqrt{t}} \qquad \text{……..(I-9)}$$

$$\frac{1}{\sqrt{t}} = \frac{L_w}{A_{cw}}4\sqrt{\pi\left(\frac{0.00633k}{\phi\mu c_t}\right)} \qquad \text{……..(I-10)}$$

Squaring both sides

$$\left(\frac{1}{\sqrt{t}}\right)^2 = \left[\frac{L_w}{A_{cw}} 4\sqrt{\pi\left(\frac{0.00633k}{\phi\mu c_t}\right)}\right]^2 \qquad \text{……..(I-11)}$$

$$1 = \frac{L_w^2 16\pi}{A_{cw}}\left(\frac{0.00633kt}{\phi\mu c_t A_{cw}}\right) \qquad \text{……..(I-12)}$$

$$1 = \frac{L_w^2 16\pi}{A_{cw}} t_{DAc} \qquad \text{……..(I-13)}$$

Since $A_{cw} = 2L_w h$

Then $1 = \frac{L_w^2 16\pi}{2L_w h} t_{DAc}$ ……..(I-14)

and $t_{DAc} = \frac{h}{8\pi L_w}$ ……..(I-15)

I-2 Constant p_{wf}

The equation for the radial flow in a horizontal well is given by

$$\frac{1}{q_{DH}} = \frac{1}{2}\ln t_{Drw} + 0.4045 \qquad \text{……..(I-16)}$$

Eq. I-16 can also be expressed as

$$\frac{kL_w\Delta p}{141.2qB\mu} = \frac{1}{2}\ln\left(\frac{0.00633kt}{\phi\mu c_t r_w^2}\right) + 0.4045 \qquad \text{……..(I-17)}$$

The equation for linear flow is given by

$$\frac{1}{q_{DL}} = 2\pi\sqrt{\pi t_{DAc}} + s_c \qquad \text{……..(I-18)}$$

Eq. I-18 can also be expressed as

$$\frac{k\sqrt{A_{cw}}\Delta p}{141.2qB\mu} = 2\pi\sqrt{\pi\left(\frac{0.00633kt}{\phi\mu c_t A_{cw}}\right)} + s_c \qquad \text{……..(I-19)}$$

Solving Eqs. I-16 to I-19 similarly to the constant rate case given previously yields

$$t_{DAc} = \frac{h}{2\pi^3 L_w} \qquad \text{……..(I-20)}$$

for the constant p_{wf} case

VITA

Name: Rasheed Olusehun Bello

Permanent Address: Harold Vance Dept. of Petroleum Engineering
TAMU, College Station TX 77843-3116.

Email Address: raolbel@yahoo.com

Education: Ph.D., Petroleum Engineering
Texas A&M University
College Station, TX, 2009.

M.Sc., Chemical Engineering
University of Saskatchewan
Saskatchewan, Canada, 2004.

B.Sc., Chemical Engineering
University of Lagos
Lagos, Nigeria, 1999.